PERFORMANCE OF REINFORCED CONCRETE COLUMN LAP SPLICES

A Thesis

by

RYAN ALBERSON

Submitted to the Office of Graduate Studies of
Texas A&M University
in partial fulfillment of the requirements for the degree of

MASTER OF SCIENCE

August 2009

Major Subject: Civil Engineering

PERFORMANCE OF REINFORCED CONCRETE COLUMN LAP SPLICES

A Thesis

by

RYAN ALBERSON

Submitted to the Office of Graduate Studies of
Texas A&M University
in partial fulfillment of the requirements for the degree of

MASTER OF SCIENCE

Approved by:

Committee Co-Chairs,	Joseph Bracci
	David Trejo
Committee Member	Mohammed Haque
Head of Department,	David Rosowsky

August 2009

Major Subject: Civil Engineering

ABSTRACT

Performance of Reinforce Concrete Column Lap Splices. (August 2009)

Ryan Alberson, B.S., Texas A&M University

Co-Chairs of Advisory Committee: Dr. Joseph M. Bracci
Dr. David Trejo

Cantilevered reinforced concrete columns with a lap splice of the longitudinal reinforcement near the base can induce high moment demands on the splice region when lateral loads are present on the structure. Code design specifications typically require a conservative splice length to account for these high moment demands and their consequences of bond failure. The required splice length is calculated as a function of required development length, which is a function of the bond between the reinforcement and the surrounding concrete, and a factor depending on the section detailing. However, the effects of concrete deterioration due to alkali silica reaction (ASR) and/or delayed ettringite formation (DEF) may weaken the bond of the splice region enough to overcome the conservative splice length, potentially resulting in brittle failure of the column during lateral loading.

This thesis presents the following results obtained from an experimental and analytical program.

- Fabrication of large-scale specimens of typical column splice regions with concrete that is susceptible to ASR/DEF deterioration
- Measurement of the large-scale specimen deterioration due to ASR/DEF accelerated deterioration

- Analytical model of the column splice region based on flexure theory as a function of the development length of the reinforcement and a factor to account for deterioration of the bond due to ASR/DEF
- Experimental behavior of two large-scale specimens that are not influenced by premature concrete deterioration due to ASR/DEF (control specimens). This experimental data is also used to calibrate the analytical model.

The conclusions of the research are that the analytical model correlates well with the experimental behavior of the large-scale control specimens not influenced by ASR/DEF. The lap splice region behaved as expected and an over-strength in the splice region is evident. To account for ASR/DEF damage, the analytical model proposes a reduction factor to decrease the bond strength of the splice region to predict ultimate performance of the region with different levels of premature concrete deterioration.

ACKNOWLEDGEMENTS

I would like to thank my committee co-chairs, Dr. Trejo and Dr. Bracci, and my committee member, Dr. Haque, for their guidance and support throughout the course of this research.

Thanks also go to my friends and colleagues and the department faculty and staff for making my time at Texas A&M University a great experience. I also want to acknowledge the engineers in the Texas Transportation Institute. They challenged me every step of the way. I also want to extend my gratitude to Matt Potter, Tim Stocks, Harding Clout, Aaron Whitsit, and Marcus Schniers for helping with the fabrication and testing of the specimens in the Structural and Materials Testing Laboratory.

Finally, thanks to my mother and father for their encouragement and to my wife for her support, patience, and love.

TABLE OF CONTENTS

Page

ABSTRACT iii

ACKNOWLEDGEMENTS v

TABLE OF CONTENTS vi

LIST OF FIGURES ix

LIST OF TABLES xv

1. INTRODUCTION 1

    1.1. Problem Statement 1
    1.2. Bond, Development Length, and Lap Splice Length 4
    1.3. Premature Concrete Deterioration Mechanisms 9
        1.3.1. Alkali-Silica Reactions (ASR) 9
        1.3.2. Delayed Ettringite Formation (DEF) 10
        1.3.3. Effects of Internal Expansion 11
    1.4. Research Objectives 14
    1.5. Research Methodology 15
    1.6. Scope of Thesis 16

2. SPECIMEN DESIGN AND CONSTRUCTION 17

    2.1. Design of Large-Scale Specimens 17
        2.1.1. Simulated Axial Load 23
    2.2. Instrumentation 25
        2.2.1. DEMEC Strain Measurements 25
        2.2.2. Electronic Strain Gages 28
    2.3. Materials of Construction 34
        2.3.1. Coarse and Fine Aggregates 35
        2.3.2. Cement 37
        2.3.3. Water 38
        2.3.4. Sodium Hydroxide 38
        2.3.5. Mix Quantities 39
        2.3.6. Reinforcement Steel 40
    2.4. Fabrication Procedure 40
        2.4.1. Reinforcement Cage Assembly 41

Page

2.4.2. Strain Gage Application 43
2.4.3. Post Tension Strand Installation 44
2.4.4. Electrical Resistive Wiring Installation 44
2.4.5. Batching and Mixing Concrete 46
2.4.6. Casting Specimens 49
2.4.7. Early Age Specimen Conditioning 51
2.5. Summary 52

3. DETERIORATION OF LARGE-SCALE SPECIMENS 53

3.1. Introduction 53
3.2. Specimen Exposure Conditions 53
3.3. Specimen Behavior during Deterioration Phase 55
3.3.1. Strains between DEMEC Points 55
3.3.2. Embedded Full-bridge Concrete Gage Measurements 61
3.3.3. Strain Gage Measurements 65
3.3.4. Crack Width Measurements 67
3.3.5. Comparison of Measurements 69
3.4. Summary 71

4. ANALYSIS OF COLUMN SPLICE REGION 72

4.1. Introduction 72
4.2. Analytical Program - Capacity Analysis Using Flexure Theory 72
4.2.1. Objectives 72
4.2.2. Modeling Assumptions 73
4.2.3. Splice Capacity Model 73
4.2.4. Iterative Analytical Model for Flexural Capacity 80
4.2.5. Strain Gage Predictions in Longitudinal Steel 89
4.3. Analytical Predictions of Undamaged Control Specimens 92
4.3.1. Four-point Test Predictions 93
4.3.2. Three-point Test Predictions 99
4.3.3. Bond Slip Predictions 105
4.4. Summary 105

5. EXPERIMENTAL TESTING AND RESULTS – LSC CONTROL SPECIMENS 107

5.1. Introduction 107
5.2. Four-point Flexural Load Tests 107
5.2.1. Experimental Design and Specimen Layout 108
5.2.2. Instrumentation 110
5.2.3. Test Procedures 117
5.3. Three-point Load Tests 117

Page

5.3.1. Experimental Design and Specimen Layout 118
5.3.2. Instrumentation 118
5.3.3. Test Procedures 121
5.4. Experimental Response 121
5.4.2. Four-point Flexural Test Results 125
5.4.3. Three-point Flexural/Shear Test Results 137
5.5. Summary 152

6. SUMMARY AND FUTURE TESTING 153

6.1. Summary 153
6.2. Future Work 155

REFERENCES 156

VITA 161

LIST OF FIGURES

Page

Figure 1-1 Example of Premature Concrete Deterioration in the Field (Photo Courtesy of D. Trejo) 3

Figure 1-2 Bond Stresses between the Reinforcing Steel and Concrete (taken from ACI 408, 2005) 4

Figure 1-3 Research Methodology by Program Benchmarks 15

Figure 2-1 Sample TxDOT Column Reinforcement Detail 18

Figure 2-2 Section B-B of the Sample Column 19

Figure 2-3 Reinforcement Layout 19

Figure 2-4 End View of the Reinforcement Layout 20

Figure 2-5 Four-point Load Test 22

Figure 2-6 Three-point Load Test 23

Figure 2-7 Strand Layout (End View) 24

Figure 2-8 Strand End Termination 24

Figure 2-9 Brass Insert with Tip Installed in the Surface of the LSC 26

Figure 2-10 DEMEC Layout in the Splice Region 26

Figure 2-11 DEMEC Installation on the Long Side 27

Figure 2-12 Internal Strain Gage Locations 29

Figure 2-13 Critical Section Instrumentation (KM Gages Were Placed in Between Column Hoops (6 in (152 mm) from Instrumented Hoop) 30

Figure 2-14 Thermocouple Locations 31

Figure 2-15 Typical Temperature History at Mid-span Section 32

Figure 2-16 Typical Temperature History at Quarter-span Section 33

Page

Figure 2-17 Typical Temperature History at End-span Section 34

Figure 2-18 Gradation of the Coarse Aggregates 36

Figure 2-19 Gradation of the Fine Aggregates 36

Figure 2-20 Voids in the First Trials 40

Figure 2-21 Rebar Types, Quantities, and Dimensions 42

Figure 2-22 ERW Layouts 45

Figure 2-23 Batching Operations 47

Figure 2-24 Dumping Cement into the Mixer 48

Figure 2-25 Slump Versus Time 49

Figure 2-26 Pouring Concrete in the Form 50

Figure 2-27 Insulated Form with ERW Power Supplies on Top 51

Figure 3-1 Specimens Exposed to Atmospheric Conditions at Riverside Campus 54

Figure 3-2 Sprinkler System between Two Specimens 54

Figure 3-3 Transverse Surface Strains on the Short Side of the LSC 57

Figure 3-4 Transverse Surface Strains on the Long Side of the LSC 57

Figure 3-5 Direct Sunlight Exposure of Columns at Riverside 58

Figure 3-6 Individual Transverse Strain Measurements on the Top Half of the Long Side of the LSC Specimens 59

Figure 3-7 Individual Transverse Strain Measurements on the Bottom Half of the Long Side of the LSC Specimens 60

Figure 3-8 KM Gage Transverse Expansion on the Short Side of the LSC Specimens 62

Figure 3-9 KM Gage Transverse Expansion on the Long Side of the LSC Specimens 63

Page

Figure 3-10 Location of the KM Gages Relative to the Hoops 64

Figure 3-11 Strains in the Hoop on the Short Side of the LSC Specimens (SG11) 66

Figure 3-12 Strains in the Hoop on the Long Side of the LSC Specimens (SG12) 66

Figure 3-13 Longitudinal Crack from ASR/DEF Expansion 67

Figure 3-14 Transverse Strains on the Short Side by Summing Crack Widths..... 68

Figure 3-15 Strain Distribution from Surface..... 69

Figure 3-16 Comparison of Transverse Strain Measurements 70

Figure 4-1 Structural Flexural Limit States 75

Figure 4-2 Linear Addition of Undeveloped Steel 76

Figure 4-3 Area of Tension Steel in the LSC Specimens Based on Reinforcement Layout 76

Figure 4-4 Linear Addition of Undeveloped Steel When $l_{d,eff}$ Equals the Splice Length 80

Figure 4-5 SG Locations on Center Bar 89

Figure 4-6 Analytical Moment Capacity and Strains of an SG Instrumented Bar 92

Figure 4-7 Moment-curvature of Splice and SG Locations..... 93

Figure 4-8 Four-point Load Test 94

Figure 4-9 Four-point Load Test at Yield Capacity versus Demand..... 95

Figure 4-10 SG Measurement Predictions for the Four-point Test Setup 96

Figure 4-11 Actuator Load versus Splice End Deflection for the Four-point Actuator Load 99

Figure 4-12 Three-point Load Test..... 100

Figure 4-13 Three-point Load Test at Yield Capacity versus Demand..... 101

Figure 4-14 Three-point Load Test Shear Demand and Capacity..... 102

Page

Figure 4-15 Capacity at the SG Sections for the Three-point Test Setup 103

Figure 4-16 Three-point Load Test Deflection at the Load Point 104

Figure 5-1 "Pinned" Support Setup 108

Figure 5-2 "Fixed" Support Setup 109

Figure 5-3 Specimen in the Four-point Test Setup 110

Figure 5-4 LVDT Installation Prior to Testing 111

Figure 5-5 KM Gage Installation Prior to Testing 111

Figure 5-6 STR Locations for the Four-point Test 112

Figure 5-7 External Sensor Layout for the Four-point Test of LSC16 113

Figure 5-8 KM Gage Detail 115

Figure 5-9 External Sensor Layout for the Four-point Test on LSC15 116

Figure 5-10 External Sensor Layout for the Three-point Tests on LSC16 and LSC15 120

Figure 5-11 Stress-strain Plots from Cylinder Compression Tests 124

Figure 5-12 Load-deflection Curve for the Four-point Test at the Actuator Load Point (Splice End) 126

Figure 5-13 Load Versus Measured Strain in the Internal Strain Gages (SG1 through SG4) and the Analytical Predictions for Each Gage 128

Figure 5-14 Load Versus Measured Strain in the Internal Strain Gages (SG5 through SG8) and the Analytical Predictions for Each Gage 129

Figure 5-15 Load Versus Measured Strain of the Internal Strain Gages in the Compression Region (SG9 and SG10) and the Analytical Predictions 131

Figure 5-16 Load Versus Measured Strain of the External Strain Gages across the Depth of the Critical Section and the Analytical Prediction 132

Page

Figure 5-17 Load Versus Measured Strain in the LVDTs across the Splice Length in the Tension Region of LSC15 133

Figure 5-18 Load Versus Measured Strain in the KM Gages along the Splice Length in the Compression Region of LSC15 134

Figure 5-19 Load Versus Measured Strain in the KM Gages at the Splice End in the Compression Region of LSC15 135

Figure 5-20 Load Versus Measured Strain in the LVDTs at the Splice End in the Tension Region on LSC15 136

Figure 5-21 Tensile Crack at the Splice End on the Bottom 136

Figure 5-22 End View of the Deflection during the Three-point Test 137

Figure 5-23 Load-Deflection Curve for the Three-point Test at the Actuator Load Point 138

Figure 5-24 Load Versus Measured Strain in the Internal Strain Gages (SG1 through SG4) and the Analytical Predictions for Each Gage 140

Figure 5-25 Load Versus Measured Strain in the Internal Strain Gages (SG5 through SG8) and the Analytical Predictions for Each Gage 141

Figure 5-26 Load Versus Measured Strain in the Internal Strain Gages (SG9 and SG10) and the Analytical Predictions for Each Gage 142

Figure 5-27 Shear and Tensile Cracks on the LSC Specimens in the Three-point Test 143

Figure 5-28 Load Versus Measured Strain in the Internal Strain Gages, SG11 and SG12 (Transverse Gages) 144

Figure 5-29 LVDTs Along the Splice Length in the Tension Region during the Three-point Test 145

Figure 5-30 Load versus Measured Strain in the LVDTs across the Splice Length in the Tension Region 146

Figure 5-31 Crushing of the Concrete in the Three-point Test 147

Figure 5-32 Load Versus Measured Strain of the External Strain Gages across the Depth of the Critical Section and the Analytical Prediction 148

Page

Figure 5-33 Load Versus Measured Strain in the LVDTs at the Splice End in the Compression Region 149

Figure 5-34 Tensile Cracks around LVDT9 and LVDT10 150

Figure 5-35 Load Versus Measured Strain in the LVDTs at the Splice End in the Tension Region 151

LIST OF TABLES

Page

Table 1-1 Reported Influence of Internal Expansive Forces on Material Properties (from Trejo et al. 2006) 12

Table 1-2 Reported Influence of Internal Expansive Forces on Structural Performance (from Trejo et al. 2006) 12

Table 2-1 Measured Aggregate Properties 37

Table 2-2 Lehigh Cement Analysis 38

Table 2-3 Mixture Characteristics 39

Table 2-4 Mixture Proportions 39

Table 2-5 Fabrication Procedure in the Structures and Materials Laboratory 49

Table 4-1 Geometric Boundaries of Tensile Reinforcement 74

Table 4-2 Sample Values from Iterative Calculations Based on Equilibrium at Cracking 84

Table 5-1 Average 28-Day Compression and Flexural Strength Results 122

1. INTRODUCTION

1.1. Problem Statement

Over the past 25 years or so, the Texas Department of Transportation (TxDOT) has had an aggressive construction program in place, especially in major metropolitan areas. To keep up with the large population growth in the state, contractors have taken aggressive construction approaches, including the proportioning of concrete mixtures to achieve high early strengths such that forms can be removed early. Although advantageous in minimizing construction costs and the speed of construction, it is believed that this practice may have led to early cracking (termed premature concrete deterioration) of many reinforced concrete (RC) bridge structures.

In addition, the chemical constituents in the cement and aggregates play a key role in the durability of the concrete structure. It has been well documented by Folliard et al. (2006) that high alkali contents in cement when used with reactive siliceous aggregates (which are very prominent in Texas) in concrete in the presence of moisture can result in alkali silica reactions (ASR). ASR can lead to the formation of expansive products, which in turn can lead to cracking of the concrete. Folliard et al. (2006) also found that concrete cracking from ASR can lead to other deterioration processes, such as delayed ettringite formation (DEF) and corrosion, which can further reduce the capacity of the structure.

In addition to high alkali contents, high cement contents and larger structural member volumes can lead to high heat generation during the early ages of the concrete (i.e., during hydration), which can also lead to cracking (both from thermal in the short term or later-age cracking).

This thesis follows the style of *The Journal of Engineering Mechanics.*

Research, such as Petrov et al. (2006) and Folliard et al. (2006), has found that reformation of ettringite results in expansion and cracking and this mechanism is associated with concrete exceeding higher temperatures (values have been reported to be from 148 ^{o}F to 160 ^{o}F [64.4 ^{o}C to 71.1 ^{o}C]) during its early age. TxDOT developed and implemented guidelines for placing concrete (Standard Specifications for Construction and Maintenance of Highways, Streets, and Bridges [2004]) such that temperatures above 160 ^{o}F (71.1 ^{o}C) are not allowed. It is believed that these guidelines have reduced the likelihood of DEF damage, but structures constructed prior to these new guidelines may be susceptible to DEF and cracking. Although DEF does not seem to be as prevalent as ASR (at least during the early phases of concrete deterioration), there has been a structure in Texas identified as exhibiting DEF only damage in San Antonio. However, in general, it is thought that structures first exhibit cracking due to ASR and then possibly exhibit DEF (Thomas 1998). ASR and DEF are different mechanisms of deterioration, but in general, both can lead to cracking of the concrete. It is this cracking that has the potential to reduce the structural capacity of the RC elements. In particular, this research is interested in the bond behavior of the reinforcing steel and the surrounding concrete.

Although significant research has been performed to assess the mechanisms of ASR and DEF deterioration, identifying the critical variables that lead to ASR and DEF, and mitigating the damage caused by ASR and DEF is critical. Several issues on the structural capacity of RC elements exhibiting ASR and/or DEF have not been thoroughly investigated. One such issue is the bond between the concrete and the reinforcing steel of critical sections in structures exhibiting ASR and/or DEF damage. Figure 1-1 shows an example of an RC column affected by premature concrete deterioration where the column has developed cracks parallel to the column height, which corresponds to the direction of tensile stresses due to gravity loading and Poisson's effect. Because a significant number of structures in Texas are exhibiting cracking caused by ASR and/or DEF (see Figure 1-1) and limited information is

available on how this cracking influences the bond, research is needed to determine the bond capacity (including development and lap lengths) in critical splice sections of the columns.

(a) Column with ASR Cracking

(b) Close-up of Crack

Figure 1-1 Example of Premature Concrete Deterioration in the Field (Photo Courtesy of D. Trejo)

1.2. Bond, Development Length, and Lap Splice Length

The objective of this section is to provide a brief overview of bond and development length of reinforcing steel and to provide an introduction on how structural codes that have been developed and been modified over the past 50 years. Figure 1-2 shows a representation of how bond develops between a deformed reinforcement and surrounding concrete. This bond is based on three mechanisms: chemical adhesion between the bar and surrounding concrete, friction force between the reinforcement and concrete due to slippage of reinforcement, and the bearing of the ribs against the concrete surface (mechanical anchorage) (MacGregor 1997). Movement of the reinforcement from applied loads causes the chemical adhesion to be lost and friction forces on the ribs and barrel of the reinforcement to develop. As slip increases, the compressive bearing forces on the ribs become the primary force transfer mechanism. If the concrete cover or the spacing between the reinforcement is sufficiently small, these stresses can cause transverse cracks that can lead to splitting cracks along the reinforcement and to the loss of bond. If the concrete cover and spacing of the longitudinal reinforcement are large or if there is sufficient transverse reinforcement to prevent splitting cracks, the structural member will fail by shearing along a surface around the bar (assuming sufficient stress is provided). The loss of bond through this type of failure is called a "pullout" failure.

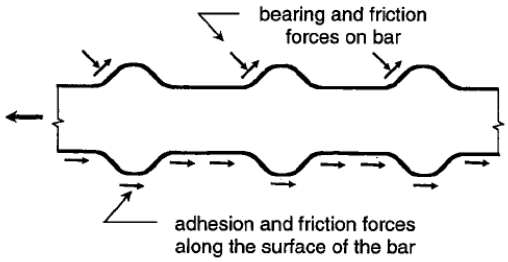

Figure 1-2 Bond Stresses between the Reinforcing Steel and Concrete (taken from ACI 408, 2005)

Section 5 of the AASHTO LRFD Bridge Design Specifications (2004) contains the provisions for the design of bridge and retaining wall components. Subsection 5.11 defines the requirements for the development length and splices of reinforcement based on work reported in ACI 318-89 (1989) (as stated in the commentary of AASHTO LRFD (2004).

The 1963 ACI 318 code (ACI 318-63 1963) defined requirements for two different terms called flexural bond and anchorage bond. Flexural bond stress was defined as a function of the rate of change of the moment along the span of the member, i.e. shear. Flexural bond provisions required comparing the peak bond stresses calculated at critical points to a limit stress. However, the complex distribution of bond stresses, especially the existence of extreme variations of bond stresses near flexural cracks, made the flexural bond calculations unrealistic. Anchorage bond stress was defined as the average bond stress between a peak stress point of the reinforcement and the end of the reinforcement where the stress is zero. Considering that all bond tests calculate an average bond resistance over a length of embedment, the ACI 318-71 (1971) code dropped the flexural bond concept and defined a development length formula based on the cross sectional area of the reinforcing bars, yield strength of reinforcing bars, and the square root of design compressive strength of the concrete. Subsequent codes had similar provisions until a new design approach was adopted in ACI 318-95 (1995) that matched observed behavior from many studies more closely.

There are five different major sets of descriptive equations for determining development length based on test results of numerous samples and statistical methods. The first set was established by Orangun et al. (1975 and 1977) for the development length of reinforcement with and without transverse reinforcement. Darwin et al. (1992) reevaluated the same data used by Orangun et al. and established an equation for the development length of reinforced samples without transverse reinforcement. Using a larger database, Darwin et al. (1996) established development length equations based on

$f_c'^{1/4}$ for reinforcement with and without transverse reinforcement (this was different than the established equations that were based on $\sqrt{f_c'}$). Later Zuo and Darwin (1998 and 2000) further developed the work performed by Darwin et al. (1996) by adding high strength concrete samples into their database. In their equations, Zuo and Darwin (1998) also used $f_c'^{1/4}$ for the effect of compressive strength for reinforcement without transverse reinforcement, however they found that a power term of ¾ to 1 was better for characterizing the effect of compressive strength on the development length of reinforcement with transverse reinforcement. Lastly, ACI committee 408 (2001) formulated the development length equations by applying minor changes to the equations developed by Zuo and Darwin (1998 and 2000).

Currently, the design provisions in ACI 318-08 (2008) for the development length of straight reinforcement in tension are based on the equations developed by Orangun et al. (1975 and 1977) as follows:

$$l_d = \left(\frac{3}{40} \frac{f_y}{\sqrt{f_c'} \left(\frac{c_b + K_{tr}}{d_b} \right)} \right) d_b \tag{1.1}$$

or:

$$l_d = \xi \left(\frac{f_y \psi_t \psi_e}{\lambda \sqrt{f'_c}} \right) d_b \tag{1.2}$$

where ψ_t is a reinforcement location factor, ψ_e is a coating factor, λ is a factor for the weight of concrete, l_d is required development length, d_b is reinforcement diameter, f_y is yield strength of reinforcement being spliced, ξ is a factor dependent on the size of

reinforcement and the spacing (see ACI 318-08), c_b is spacing or cover dimension, and K_{tr} is the transverse reinforcement index as follows:

$$K_{tr} = \frac{A_{tr} f_{yt}}{1500sn} \tag{1.3}$$

where A_{tr} is the area of the stirrup or tie legs crossing the potential plane of splitting adjacent to the reinforcement being developed, spliced, or anchored, f_{yt} is the yield strength of transverse reinforcement, s is the spacing of transverse reinforcement, and n is the number of bars being developed or spliced. To limit the probability of a pullout failure, ACI 318-08 (2008) also requires:

$$\frac{c + K_{tr}}{d_b} \leq 2.5 \tag{1.4}$$

ACI 318-08 (2008) also limits the $\sqrt{f_c'}$ to a maximum value of 100 psi (689.5 kPa). Eq. (1.1) results in a lower calculated development length for this research and is discussed further in Section 2.1.

ACI 318-08 (2008) defines two types of lap splices, Class A and Class B. Class A splices can be used when the ratio of provided steel area to required steel area equals to two or more, and 50 percent or less of the steel is spliced within the lap. All other splices are defined as Class B. The lap splice length for Class A splices is equal to the development length, where the splice length of Class B splices is 1.3 times the development length. Because the AASHTO LRFD (2004) bridge design is based on the 1989 version of the ACI 318-89 (1989) code, it also includes a Class C splice classification that is no longer used in the new version of the ACI 318-08 (2008) code (removed to encourage splicing bars at points of minimum stress and to stagger the

splices). According to AASHTO LRFD (2004), Class C splices are 1.7 times the development length.

In addition to the ACI 318-08 (2008), there are three additional design provisions that can be followed to calculate development lengths. The first, published by the ACI 408 committee, was adopted as ACI 408.3 (2001) and provides provisions for the development length and splices of deformed reinforcement with high relative rib area. The second is the ACI committee 408 provisions based on the work of Zuo and Darwin (1998 and 2000). The last is the CEB-FIP Model code (1990). A structural reliability analysis performed by the ACI 408 committee compared the available design provisions using their database and found that the CEB-FIP code (1990) had more scatter and greater coefficient of variation compared to the other design provisions.

Because AASHTO is widely used to design bridge columns, the AASHTO definition for development length was used in this thesis. The AASHTO LRFD Bridge Design Specification (2004) for l_d is as follows:

$$l_d = \frac{1.25 A_b f_y}{\sqrt{f'_c}} \tag{1.5}$$

where A_b is the area of the reinforcement being spliced (in^2), f_y is the yield strength of the spliced reinforcement in ksi and f'_c is the compressive strength of the concrete in ksi. Like ACI 318-08, the AASHTO specifications have different classes of lap splices that are based on the development length. However, using the ASSHTO specifications (2004), the splice used in this research is classified as a class C splice and is required to provide $1.7 l_d$ and is further discussed in Section 2.1.

1.3. Premature Concrete Deterioration Mechanisms

This section provides an overview of the mechanisms of premature concrete deterioration believed to cause cracking in various bridge columns across Texas, mainly due to ASR and/or DEF. Prior research has not identified the contribution of either mechanism on the magnitude of deterioration, but the literature has defined certain criteria for the mechanism to be present (Folliard 2006). The section below provides a brief review of ASR and DEF mechanisms followed by how ASR and DEF influence, or damage, concrete structures.

1.3.1. Alkali-Silica Reactions (ASR)

ASR is the chemical reaction between the alkalis in concrete (generally from the cement) and reactive silica found in naturally occurring concrete aggregates. Conditions required for ASR include reactive silica phases in the aggregate, availability of alkali hydroxides in the pore solution ($[Na^+]$, $[K^+]$, $[OH^-]$), and sufficient moisture (Folliard et al. 2006). The reaction between the reactive silica in the aggregate and the alkalis in the pore solution produce a by-product, commonly referred to as ASR gel, that expands with time, causing cracking. However, the alkalis and reactive silica are consumed with time and are eventually depleted. As these constituents are consumed, the ASR process will stop unless these constituents are provided from an external source (Folliard et al. 2006).

As the ASR gel forms, Folliard et al. (2006) found that tensile stresses develop internally in the concrete. In general, the hydrated cement paste (HCP) is weaker than the aggregate and cracking initially occurs in the HCP or along the interface of the aggregate and HCP (Poole 1992, Swamy 1992). Jensen (2003) found that ASR damaged concrete exhibited both cracking in the HCP and aggregate and even quantified the amount of cracking in the aggregate. Bazant et al. (2000) modeled the fracture mechanics of ASR using radial cracks propagating from flaws at the aggregate-HCP interface into the HCP

using the theories of Poole (1992) and Swamy (1992). The literature indicates that although cracking due to ASR initiates in the HCP, eventual expansion can result in cracking of the aggregates. Aggregate cracking can influence the shear capacity (aggregate interlock) and may be one factor influencing the bond strength of splice reinforcement.

1.3.2. Delayed Ettringite Formation (DEF)

Many researchers have developed different hypotheses on how DEF occurs in hardened concrete. In general, ettringite forms at early ages in fresh concrete. As the sulfate (typically from the gypsum in the cement) reacts with the calcium-aluminates in the presence of calcium hydroxide, these sulfates are consumed. Once the sulfate concentration in the pore solution reaches some lower value, the calcium-aluminates react with the already formed ettringite to produce monosulfoaluminate (Folliard et al. 2006). If sulfates are reintroduced to the pore solution, the monosulfoaluminate can revert back to ettringite, causing expansive forces and cracking. Note that sulfates can be reintroduced from external sources or from internal sources. Sulfate attack from external sources is not the topic of this research and will not be addressed here. It is believed that ettringite reformation in hardened concrete occurs when the concrete has been subjected to high early-age heat. When subjected to high early heat, it is believed that the majority of the sulfate ions are physically attached to the calcium silicate hydrate (C-S-H) and are therefore available as a mobile source of sulfate at later ages (Scrivener and Lewis 1997, Odler and Chen 1996). Thus, concretes that experience elevated temperatures during hydration, either from high cement contents or large placements (typical of structures exhibiting cracking in Texas), are subject to DEF.

Unlike ASR where the stresses and cracking initiate at the HCP-aggregate interface, internal stresses from DEF occur in the HCP (typically at void locations) (Folliard et al. 2008). Although damage initiates in different areas, both mechanisms (ASR and DEF) lead first to cracking of the HCP and depending on the degree of expansion, cracking of

the aggregates. Because both deterioration processes result in similar damage types, further discussions will focus on issues related to internal expansive forces (also referred to as premature concrete deterioration), unless specific characteristics of ASR or DEF lead to unique damage types.

1.3.3. Effects of Internal Expansion

It is clear that the expansive products of ASR and DEF lead to internal expansion in the concrete. A few studies have shown the impacts from internal expansion on material properties such as the compressive strength, tensile strength, flexural strength, and the modulus of elasticity on small scale samples (Table 1-1). Table 1-1 shows a reduction trend in the strength and stiffness of the material due to the internal expansive forces. As the material strength decreases, so potentially does the structural performance.

Table 1-1 Reported Influence of Internal Expansive Forces on Material Properties (from Trejo et al. 2006)

Author(s)	Material Properties			
	Compressive Strength	Tensile Strength	Flexural Strength	Modulus of Elasticity
Ahmed et al. (1999a&b)	⇩	⇩	⇩	⇩
Monette et al. (2002)	⇧			⇩
Swamy and Al-Asali (1986)	⇩	⇩	⇩	⇩
Zhang et al. (2002)				⇩[3]
Giaccio et al. (2008)	⇩			

⇩ - reduction; ⇧ - increase; ⇔ - no or minimal change

1. All sample sets (average values) obtained from cores exhibited lower strength values. All sample sets from exposed cylinders except 1 exhibited lower values.
2. Cubes. Results dependent on expansion; larger expansions resulted in reduced compressive strength.
3. Dynamic modulus.

Table 1-2 Reported Influence of Internal Expansive Forces on Structural Performance (from Trejo et al. 2006)

Author(s)	Structural Characteristic					
	Flexure	Bearing	Shear	Bond	Lap Length	Fatigue Life
Chana (1989)				⇔[1] & ⇧		
Ahmed et al. (1998)			⇧			
Ahmed et al. (1999a)	⇩			⇩		⇩
Ahmed et al. (1999b)		⇩				
Fan and Hanson (1998)	⇔					
Swamy and Al-Asali (1989)	⇩					

⇩ - reduction; ⇧ - increase; ⇔ - no or minimal change

1. Samples with small cover and no stirrups exhibited reduced bond. Samples with adequate cover and stirrups exhibited similar or increased bond when compared with control samples.
2. Only an approximate reduction of 4% was observed from samples with over 3000 microstrain
3. Increased shear for samples exhibiting moderate expansion and reduced shear for samples exhibiting severe expansion.

The results of testing small scale specimens exhibiting internal expansion for structural performance (Table 1-2) were similar to the material properties in Table 1-1. The majority of the results found a decrease in the structural capacity with a couple of exceptions. Take note of the lack of research done on the effects of internal expansion on the lap length of bars in the concrete, especially at large-scale. These data were primarily obtained from small-scale specimens, which likely do not have the same behavior as large-scale specimens.

A study on the structural behavior of concrete beams affected by ASR was done by Multon et al. (2005). The specimens were 9.8 in by 19.7 in by 118.1 in (0.25 m by 0.5 m by 3 m) and included a reinforcement structure. It was concluded that the effect of reinforcement on the internal expansion of the concrete is substantial, especially in the longitudinal direction where the largest decrease of strains and deflections took place. However, it was also found that the local offsets of the stirrups had little effect on the transverse deformations. That is, the concrete between the stirrups did not exhibit substantially different expansion than the concrete around the stirrups. Hamada et al. 2003 also found similar results where steel bars reduce the amount of strain in the surface. The closer the bar is to the surface, the higher the strains were in the steel and the smaller the strains were at the concrete surface.

Table 1-2 also shows a lack of research on the effect of internal expansion on the lap length. The present literature on lap length reductions pertain mostly to corrosion and studies on the confinement of the surrounding concrete.

1.4. Research Objectives

The major objectives of this thesis are:

- Evaluate the experimental behavior of large-scale specimens of a critical lap splice region in a bridge column under varying levels of premature concrete deterioration due to ASR and/or DEF
- Develop a preliminary analytical model that can evaluate the behavior of a splice region under varying levels of concrete deterioration based on calibration from experimental behavior

The specific tasks reported in this thesis are:

- The design and construction of the large-scale specimens, with a lap splice region similar to bridge columns in the field, to be load tested to failure
- To develop a construction methodology and deterioration environment for the large-scale specimens that can accelerate premature concrete deterioration and instrument the specimens to track the internal expansion due to ASR and/or DEF
- To develop a deterministic analytical model for the flexural capacity of a lap splice region in a bridge column that takes into account the possible deterioration in bond strength from ASR and/or DEF
- To validate the analytical mode using the structural testing of two large-scale control specimens (unaffected by premature concrete deterioration) and provide a baseline of results used to compare the test results of deteriorated specimens at a later date

1.5. Research Methodology

This research requires both an analytical and experimental program to reach the objectives defined in Section 1.4. The two programs are dependent on each other to successfully calibrate a model that can capture the structural effects of the ASR and/or DEF deterioration. Figure 1-3 shows the interdependence between the two programs. This thesis covers the first two boxes of each program as shown by the dashed box.

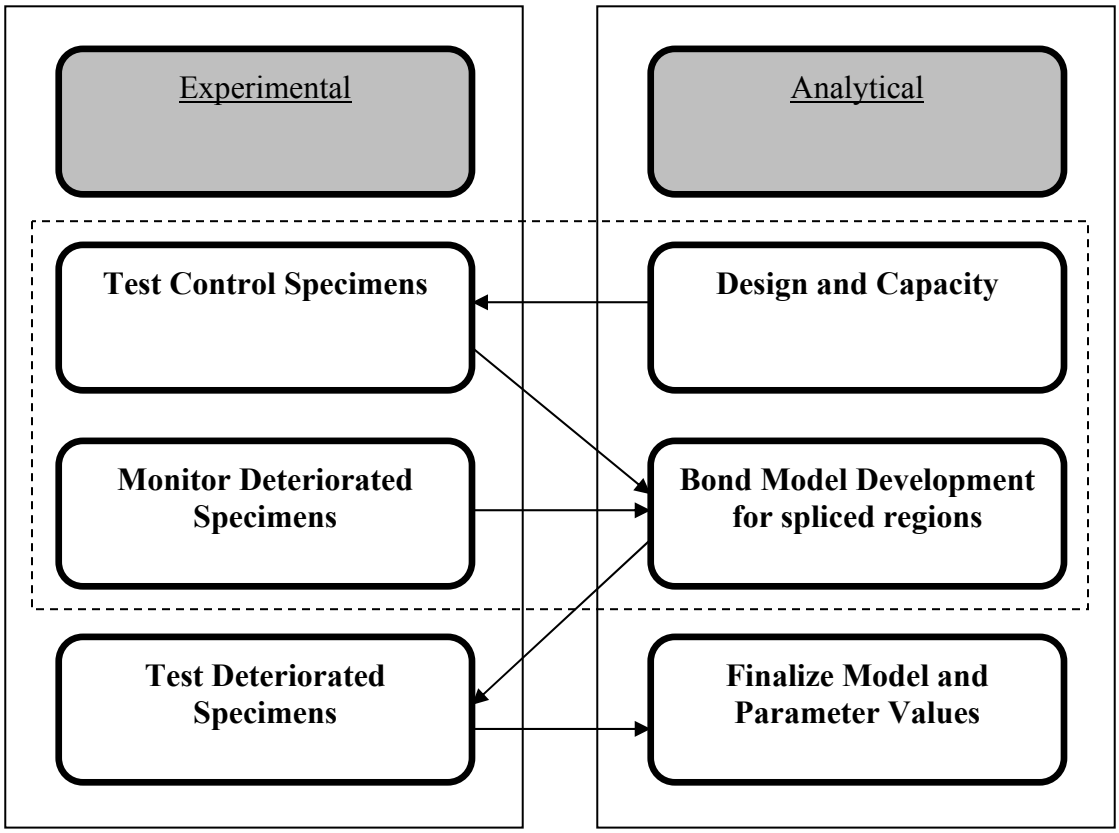

Figure 1-3 Research Methodology by Program Benchmarks

1.6. Scope of Thesis

A section-subsection format is used for this thesis. The term "section" refers to each of the 6 main levels of this thesis and the term "subsection" refers to each consecutive section embedded therein The progression of sections is as follows:

- Section 1 (the current section) has the problem statement and background. This is followed by a brief explanation of deterioration mechanisms and the lack of research on their effect on the bond between the reinforcing bars and the concrete in a lap splice region. After that, the research objectives and methodology of this research are discussed.
- Section 2 provides information on the methods and materials used in design, fabrication, and construction of the large-scale specimens with an emphasis on inducing ASR and DEF. This section also focuses on the implementation of instrumentation to capture the resulting internal expansions from ASR and/or DEF and later strains from load testing.
- Section 3 discusses the accelerated deterioration environment of the deterioration phase of the large-scale specimens and the current internal expansion strains of the specimens.
- Section 4 presents the deterministic analytical model that describes the flexural capacity in the splice region of the large-scale specimens (unaffected by ASR/DEF) relative to both a three- and four-point load test configuration.
- Section 5 presents the results from testing two large-scale control specimens and compares the results with the computations from the analytical model. Modifications to the analytical model to account for premature concrete deterioration are also discussed in terms of the future testing on the deteriorated specimens at a later date.
- Section 6 presents the summary, conclusion, and future work of this research.

2. SPECIMEN DESIGN AND CONSTRUCTION

2.1. Design of Large-Scale Specimens

This research focuses on the performance of the splice region of a typical reinforced concrete bridge column subject to ASR and/or DEF. Because in-service bridge columns can vary considerably in size and geometry, a large-scale column (LSC) specimen was designed to utilize a common splice found in the field at the column/foundation connection, which is typical in non-seismic regions.

Figure 2-1 shows an example of reinforcement details for a bridge column in Houston, TX. The footing has 48 #11 bars (Bars R) that are distributed evenly around the perimeter of the column (see Figure 2-2) and extend 107 in (2.72 m) into the column. The Bars R overlap with 48 #11 Bars V of the column reinforcing steel to form a lap splice. The hoops in the region are #5 reinforcing bars and are spaced at 12 in (305 mm) in this region. The column supports the loads from the bridge deck above, which can be assumed to be primarily an axial compression load. However, during high winds from hurricanes and vehicle collisions, large lateral forces can be exerted on the bridge that result in bending moment demands in the column splice region. The tensile strength of the splice is the limiting parameter of the flexural capacity of the column and overall lateral resistance of the bridge. Due to the fact that the strength of the lap splice is dependent upon the bond, the effects of ASR and/or DEF expansion on the bond is of concern. If the bond is decreased enough that the bars slip prior to reaching their yield strength, the capacity of the column may not be high enough to resist the structural demands and failure might be possible.

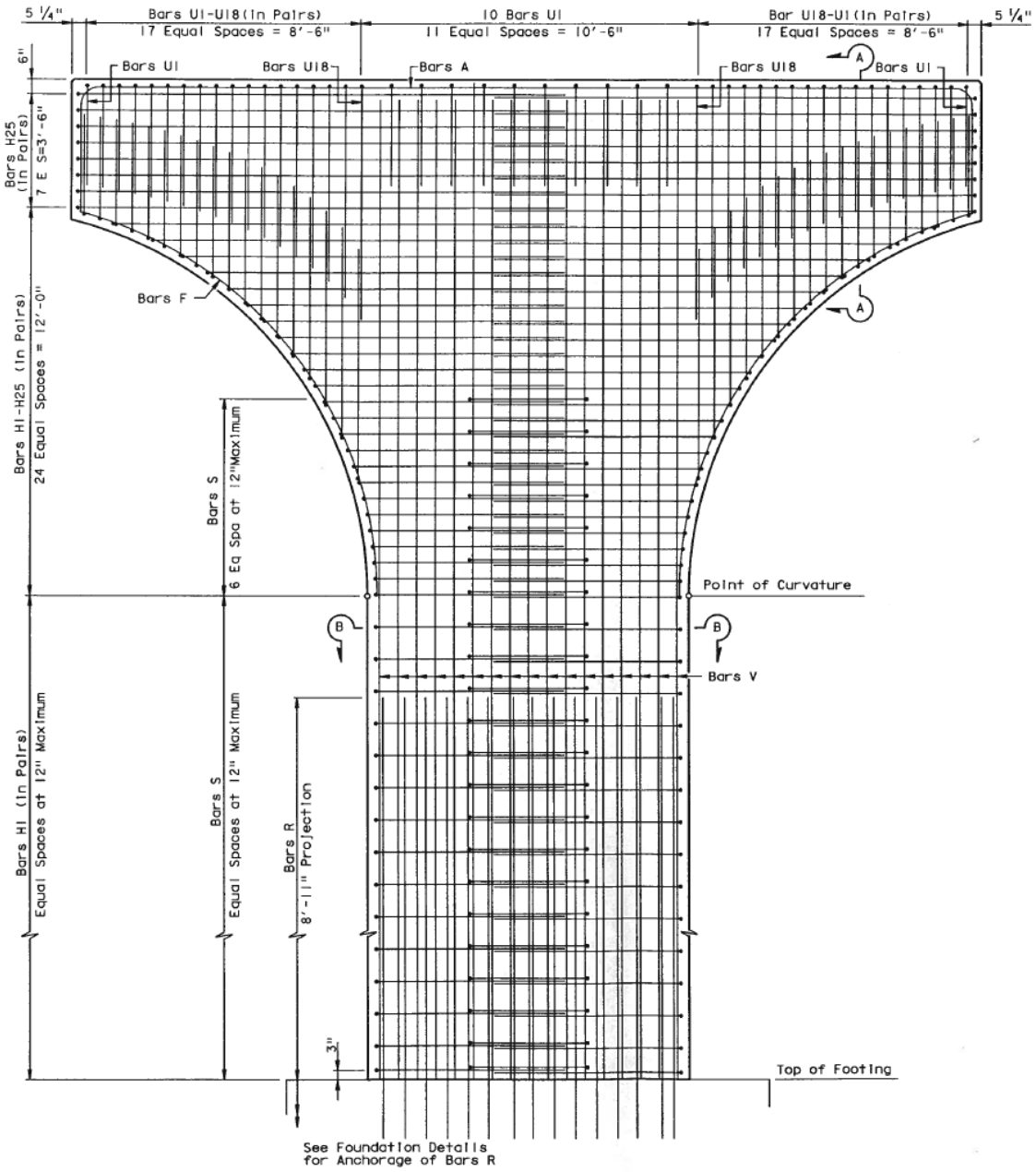

Figure 2-1 Sample TxDOT Column Reinforcement Detail

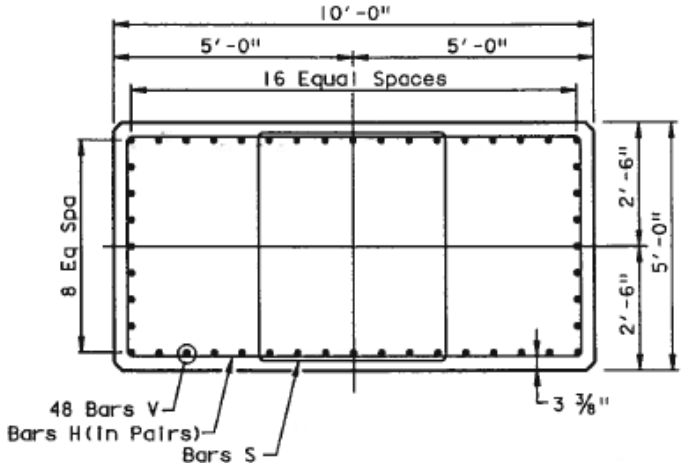

Figure 2-2 Section B-B of the Sample Column

In an effort to reduce costs and maximize the specimen size based on the constraints of the testing laboratory, sixteen LSC specimens were utilized in the experimental research program. Specimens were 2 ft x 4 ft (0.61 m x 1.22 m) in cross section with six #11 bars overlapped in the 9 ft (2.74m) splice region, which is the same overlap length used by TxDOT (see Figure 2-1). Figure 2-3 and Figure 2-4 show the dimensions and rebar layout of the LSC specimens. Additional information about the LSC specimens is presented in Section 2.4.1.

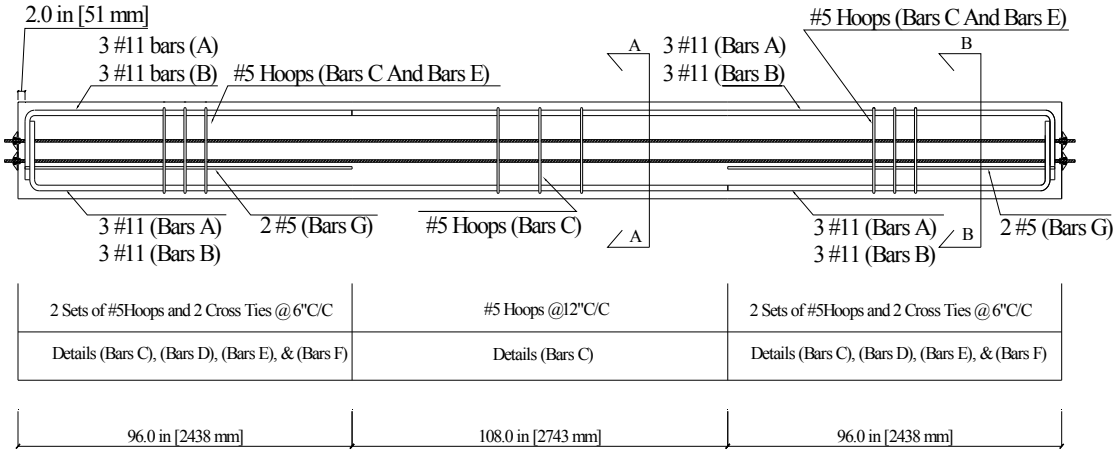

Figure 2-3 Reinforcement Layout

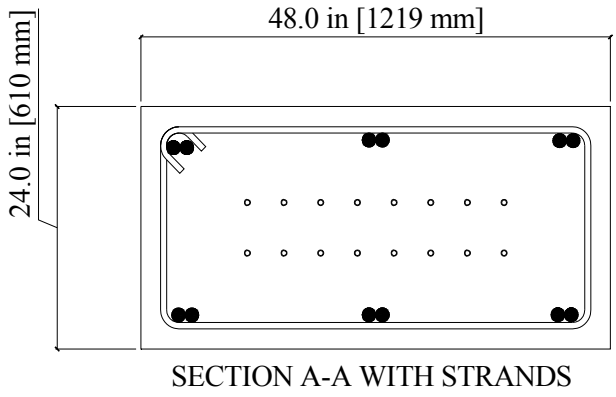

(a) Splice Region

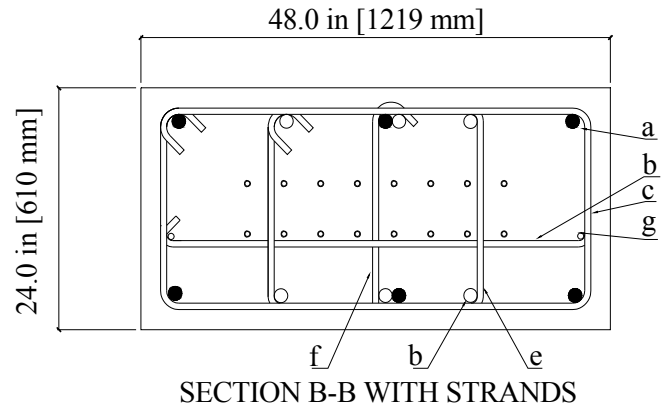

(b) End Region

Section B-B Parts	
a	6 #11 Bars A [marked with fill]
b	6 #11 Bars B [marked without fill]
c	#5 Hoops @ 6" C/C (Bars C)
d	#5 Cross Ties @ 6" C/C (Bars D)
e	#5 Hoops @ 6" C/C (Bars E)
f	#5 Cross Ties @ 6" C/C (Bars F)
g	2 #5 Bars (Bars G)

Figure 2-4 End View of the Reinforcement Layout

In ACI 318-08/318R-08 (2008), *Building Code Requirements for Structural Concrete and Commentary* and AASHTO LRFD *Bridge Design Specifications* (2004), the required splice length is a function of the required development length and a factor as presented in Section 1.2. For the #11 bars using f'_c =5000 psi (34.5 MPa) and Eq. (1.2), the required development length is 60 in (1.52 m) and 46.7 in (1.19 m) according to Eq. (1.1). Therefore, using the smaller of the two, the provided splice length of 9 ft (2.74 m) in the LSC specimens corresponds to 2.3 times l_d. In ACI 318-08 (2008), a Class B splice length (when the area of reinforcement provided is not at least twice that required by analysis over the entire length of the splice and when the splice is staggered) is required to have 1.3 times l_d, which means that the provided splice length is overdesigned by 78%.

Eq. (1.5) yields a required development length of 52 in (1.32 m) for a #ll bar. Therefore, the provided splice length in the LSC specimens corresponds to 2.08 times l_d. In the AASHTO LRFD (2004), this splice is required to have a Class C splice, which requires the splice length to be 1.7 times l_d. This means that the splice is overdesigned by 22% according to the AASHTO LRFD specifications (2004). Both ACI 318-08 and the AASHTO LRFD (2004) show this splice to be conservatively designed. The question is whether or not the effects of ASR and/or DEF will deteriorate the bond of the reinforcing steel in the splice region of the columns enough to overcome the conservative design. Continuing forward in this work, the AASHTO (2004) version of l_d will be used for all calculations in the specimens of the experimental program.

To evaluate the experimental performance of the splice regions, the LSC specimens will first be load-tested to failure using a four-point load test. Figure 2-5 shows that a constant moment is applied over the splice region which allows for the weakest section of the region to crack, yield, and ultimately fail. In this test setup a constant tension force across the entire splice length is created in the bottom longitudinal reinforcement. For an in-service cantilevered bridge column under lateral loading, the bending moment

in the column varies linearly from zero at the top to maximum at the column base, which implies that the splice reinforcement is not loaded uniformly along its length. However, the test setup will yield conservative values in terms of the splice performance.

Following the four-point load test, the LSC specimens will be further tested using a three-point test setup. Figure 2-6 shows that a three-point test creates a uniform shear force throughout the splice region and a linearly increasing moment demand from zero at the support to maximum at the reaction support. The provided splice length is reduced to half of that in the previous test, so the expectation is that bond failure in the splice end might develop. The test setups are further discussed in Section 5.l

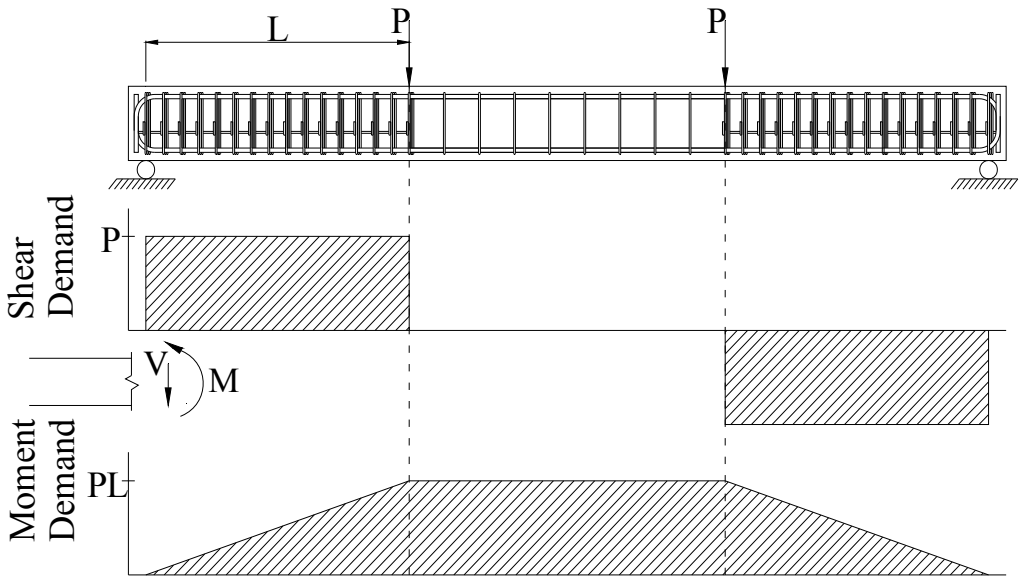

Figure 2-5 Four-point Load Test

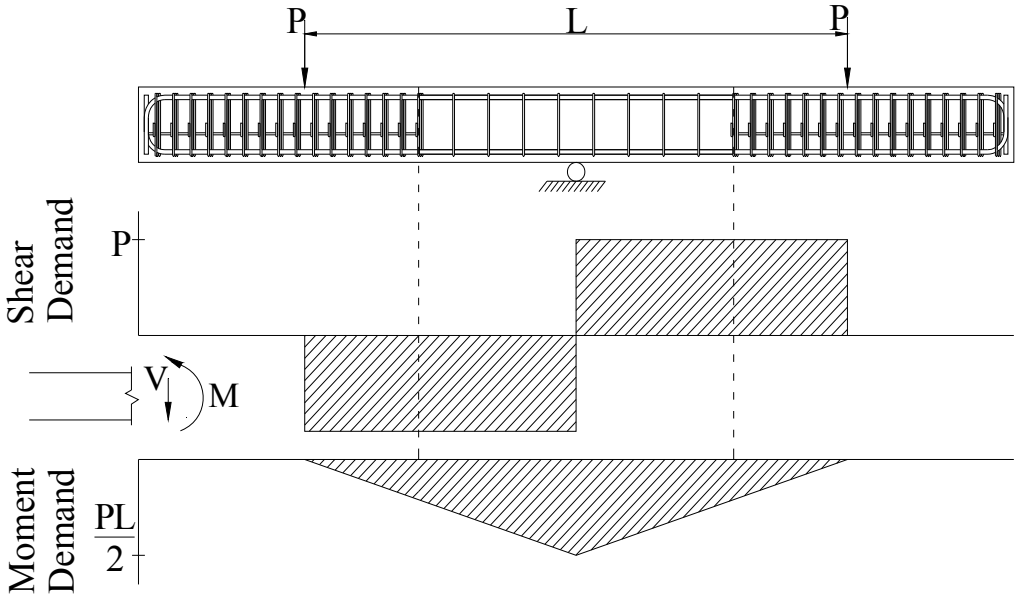

Figure 2-6 Three-point Load Test

2.1.1. Simulated Axial Load

To simulate in-service gravity loading on the bridge column, the specimens have sixteen 0.6 in (15 mm)-diameter, unbonded, post tensioning (PT) strands manufactured by VSL. The PT strands were centered throughout the specimen cross section as shown in Figure 2-7. The unbonded strands were bound in a plastic sleeve and coated with a lubricating grease to limit friction losses during post tensioning. The strands were terminated through a base plate that sat flush with the concrete on one side and flared out on the other side to accommodate 2 collets that held the tension in the strand. Figure 2-8 illustrates the strand extending out of the concrete through the base plate and collets. The strands were hydraulically jacked to 0.7 f_{pu}, ultimate tensile stress, as specified by the AASHTO (2004) Specification, which results in 36.3 kips (161.47 kN) per strand and a total of 580.5 kips (2582.19 kN) of compression on the column specimen. This level of axial load corresponds to about 10% of the axial compression strength of the column, which is commonly found in columns under service loading.

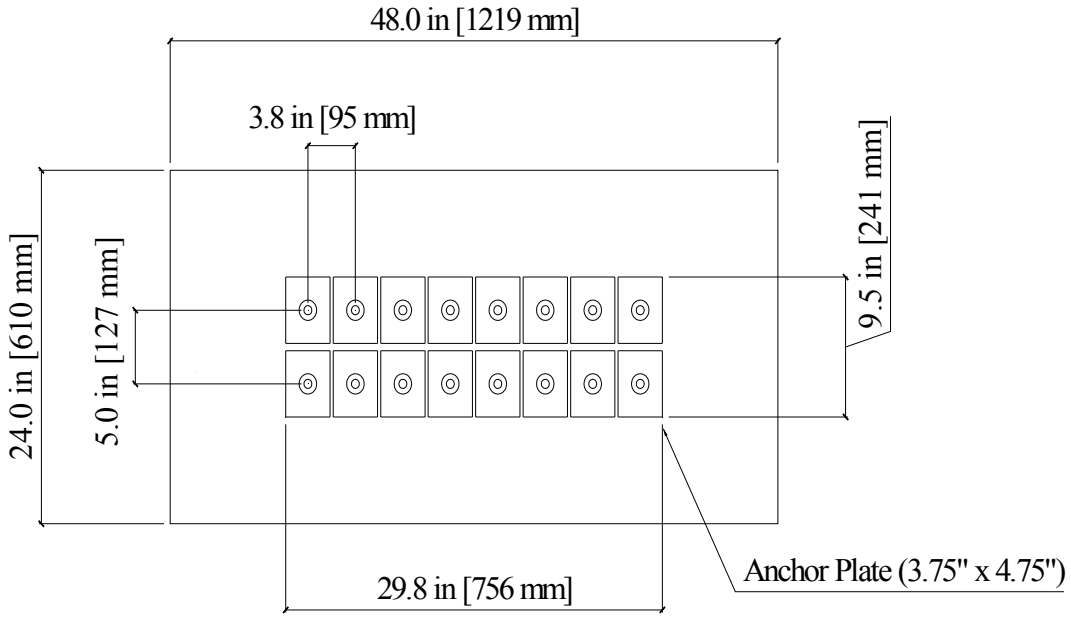

Figure 2-7 Strand Layout (End View)

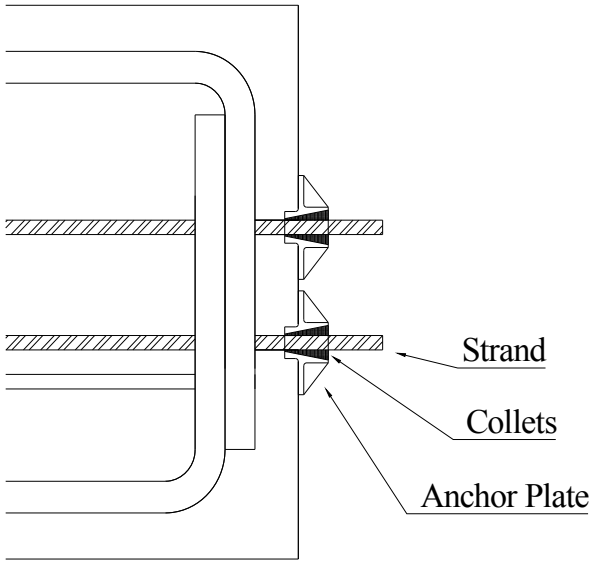

Figure 2-8 Strand End Termination

2.2. Instrumentation

During load testing and deterioration, strains in the LSC specimens need to be identified and documented. The LSC specimens are exposed to an environment that accelerates ASR and/or DEF which should induce large transverse strains (due to the tension field from Poisson's Effect), and potentially longitudinal strains in the column. These strains occur on the surface and internally in the concrete and reinforcement steel. Demountable mechanical (DEMEC) strain gages are used to measure the surface strains in the transverse and longitudinal directions of the LSC specimens throughout the splice length. Internally, 5 full-bridge, concrete embedment gages (type KM) were embedded in the concrete to capture the transverse strains of the concrete. Gages were placed 1 in (25.4 mm) on both sides of the reinforcing hoops. The KM gages were chosen because the KM series of strain gages are designed to be embedded in concrete; the gages are hermetically sealed, bond to surrounding concrete, and have a low elastic modulus which allows for more accuracy. Additionally, two half-bridge strain gages (SG) were attached to the hoops for transverse strain measurements. During load testing, the strains in the longitudinal reinforcement in the splice are also monitored to evaluate the tensile behavior of the bar. Ten SGs were installed on bars in the splice region. Additionally, during the curing stage of the concrete, the temperature distribution of the concrete throughout the specimen was monitored using thirty-two embedded thermocouples (TC) during the first 36 hours to ensure satisfactory temperatures for DEF.

2.2.1. DEMEC Strain Measurements

The DEMEC points consisted of a brass insert and a measurement tip that is screwed into the brass insert. Figure 2-9 shows the installed position of the brass inserts and measurement tips. Both the brass inserts and measurement tips are manufactured by ELE International. Holes, 1 in (25.4 mm) deep and 7/16 in (11.11 mm) in diameter, were drilled into the LSC specimen at a 10 in (0.254 m) grid spacing following

construction. The entire grid measured 40 in x 110 in (1.02 m x 2.79 m) in area on the long side and 20 in x 110 in (0.51 m x 2.79 m) in area on the 2 ft (610 mm) short side of the LSC specimens. Figure 2-10 shows the grids centered longitudinally and transversely on each respective face.

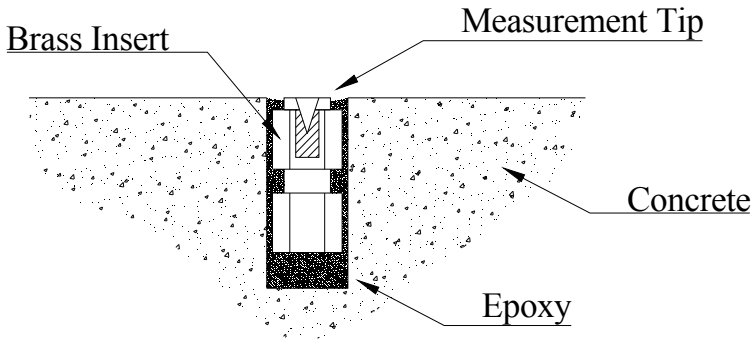

Figure 2-9 Brass Insert with Tip Installed in the Surface of the LSC

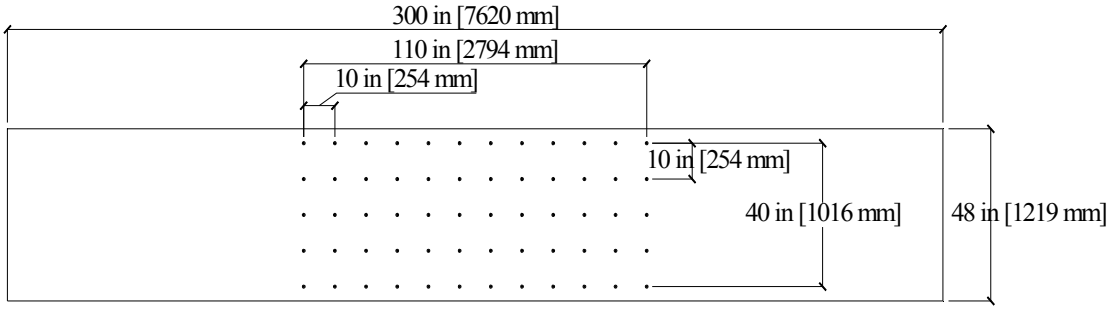

(a) Long Side of the LSC

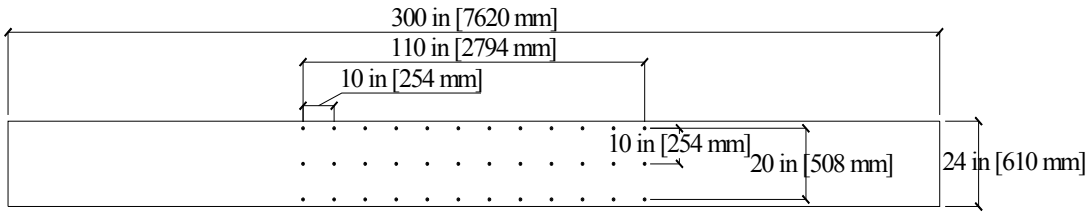

(b) Short Side of the LSC

Figure 2-10 DEMEC Layout in the Splice Region

Figure 2-11 shows the brass inserts attached to aluminum strips which were used to suspend the brass inserts in the holes and keep them flush with the surface until the epoxy set. A high-modulus epoxy was used to permanently attach the inserts and therefore reduce the error of strain measurements in the future. This was done on the long side first to use gravity in keeping the glue in the holes; then the LSC specimens were rolled onto their sides and the same procedure was used to install the DEMECs on the short side of the LSC specimens.

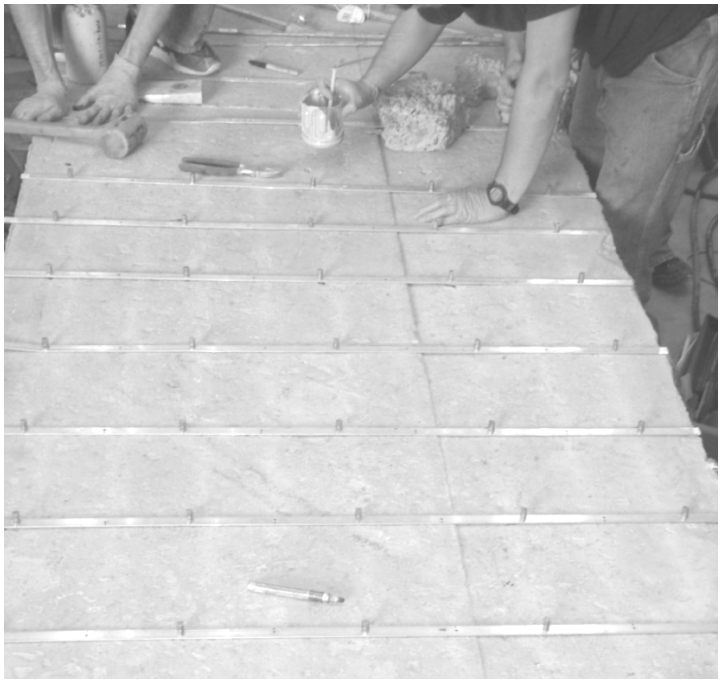

Figure 2-11 DEMEC Installation on the Long Side

Once the epoxy hardened, the aluminum strips were unscrewed from the brass inserts and peeled off the concrete. The tips were then inserted into the brass inserts and the grid was measured for initial gage lengths using a caliper with a precision of 0.0005 in (12.7 μm). This value was later used for strain calculations as the initial length prior to expansions from ASR/DEF.

2.2.2. Electronic Strain Gages

In addition to the DEMECs, several electronic sensors were installed in the specimens to measure the internal strains due to ASR/DEF deterioration and also from load testing. SGs were attached to the reinforcing steel as outlined in Section 2.4.2 and placed for monitoring of ASR/DEF expansive strains and stresses from the flexural load testing of the LSC specimens. Figure 2-12 shows 8 SGs placed on the longitudinal tension steel in the splice region, 4 on a center bar and 4 on a corner bar. SG 9 and SG 10 were placed on a compression bar in the middle of the splice and SG 11 and SG 12 were placed on two legs of a hoop in the middle of the splice region. SG 11 and SG 12 are used primarily for monitoring expansion in the field, but will pick up strain during load testing if shear forces are present (three-point load test).

The 5 KM gages were embedded in the concrete at the center of the splice to monitor expansive concrete strains during the deterioration phase. Four of the KM gages were placed such that they were 1 in (25.4 mm) and 3 in (76 mm) from each side of the specimen face and the final KM gage was placed perpendicular to the transverse steel. Note that the KM gages were placed between the column hoops. However, the control specimens were not instrumented with these gages because they were kept in the laboratory (or dry environment) which is not conducive to ASR/DEF deterioration. Figure 2-13 shows the orientation of the gages relative to the nearest hoop, with attached SG 11 and SG12. The embedment gages are used to measure the strain in the cover and the strain inside the hoop. Combined with the strain gages on the reinforcing steel hoop and the DEMECs, this allows for a strain distribution starting from the surface to 3 in (76.2 mm) below the surface to be generated at 1 in (25.4 mm) intervals.

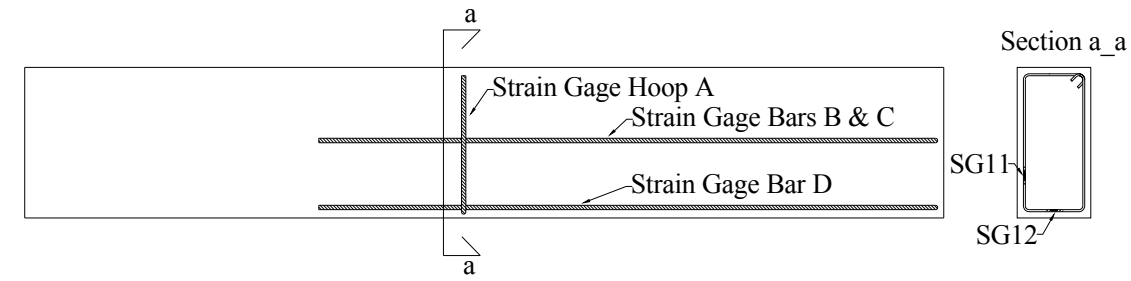

(a) Plan View and Side View of Strain Gage Hoop A

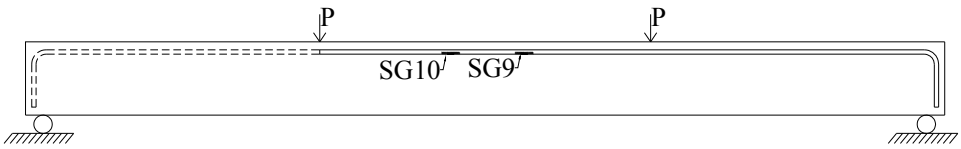

(b) Front View of Strain Gage Bar B (Compression Steel)

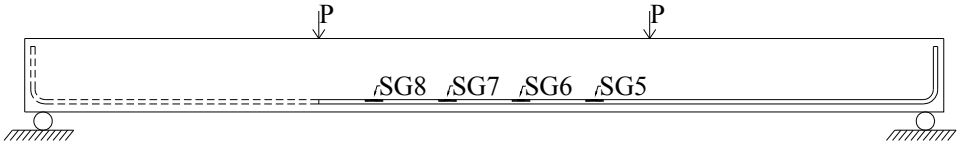

(c) Front View of Strain Gage Bar C (Tension Steel)

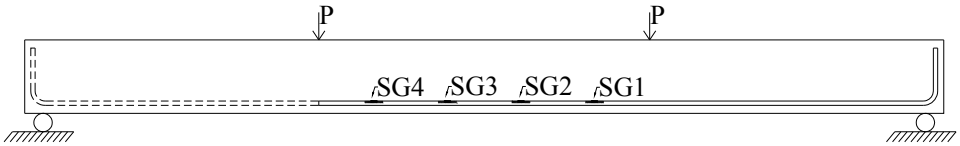

(d) Front View of Strain Gage Bar D (Tension Steel)

Figure 2-12 Internal Strain Gage Locations

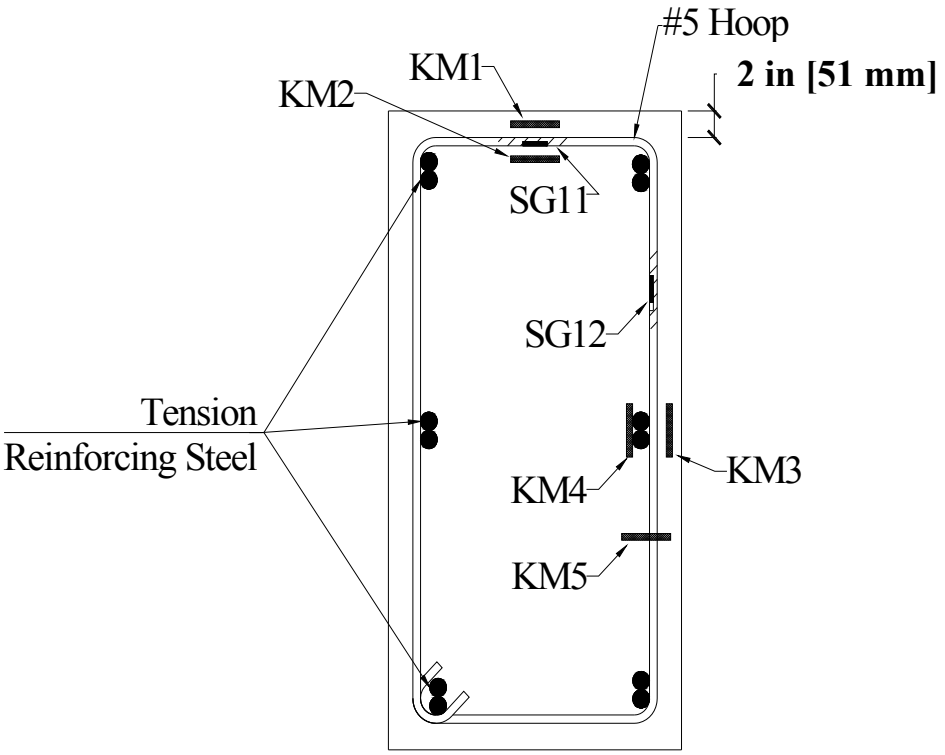

***Note: KM gages were placed in between the column hoops (i.e. 6 in [152 mm] from the instrumented hoop)**

Figure 2-13 Critical Section Instrumentation (KM Gages Were Placed in Between Column Hoops (6 in (152 mm) from Instrumented Hoop)

In addition to strain gages, 32 thermocouples (TC) were installed throughout the specimen to monitor the heat distribution during curing (see Figure 2-14). The TCs were attached to the reinforcing steel and the wire was routed outside the form for easy access. Figure 2-15 through Figure 2-17 show the typical recorded heat distributions from the TCs embedded in the LSC specimens.

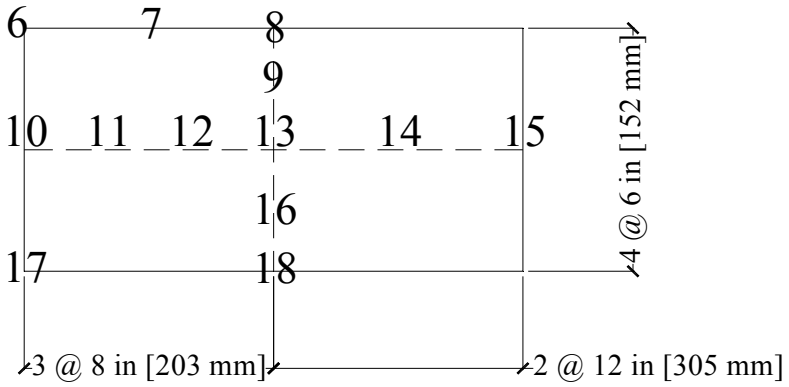

(a) Mid-Span Section

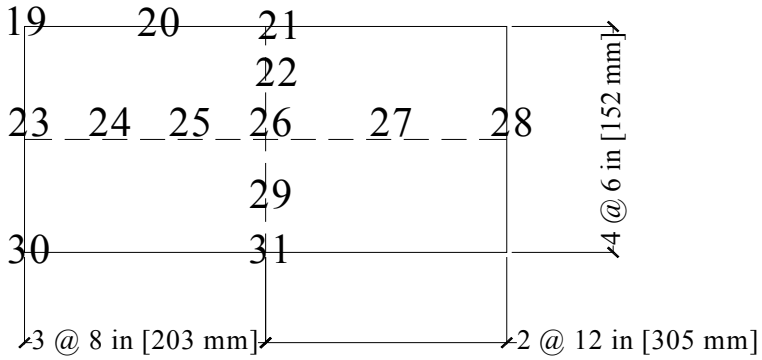

(b) Quarter-Span Section

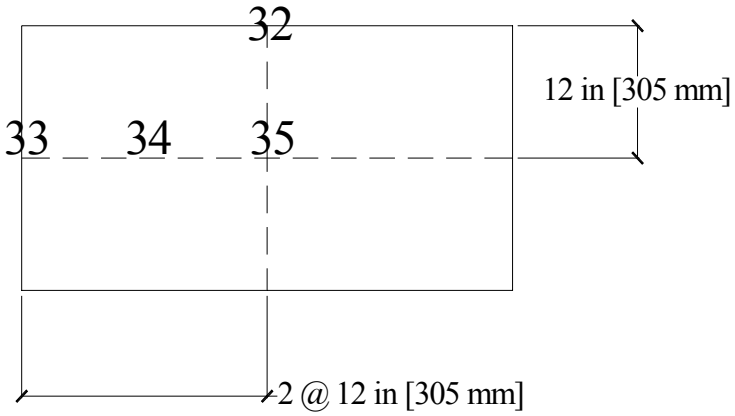

(c) End-Span section

Figure 2-14 Thermocouple Locations

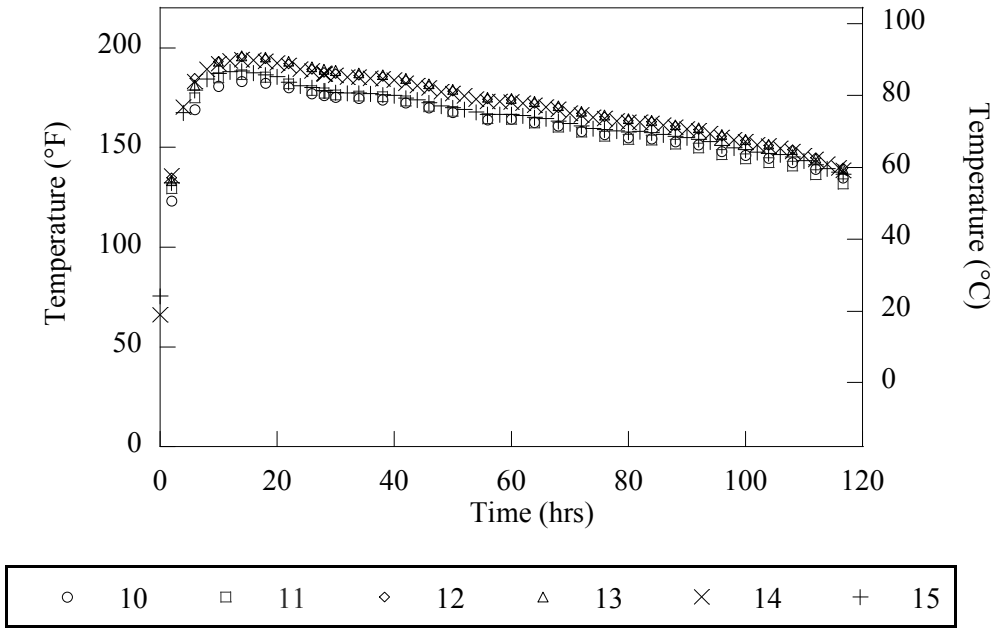

(a) Horizontal Measurements

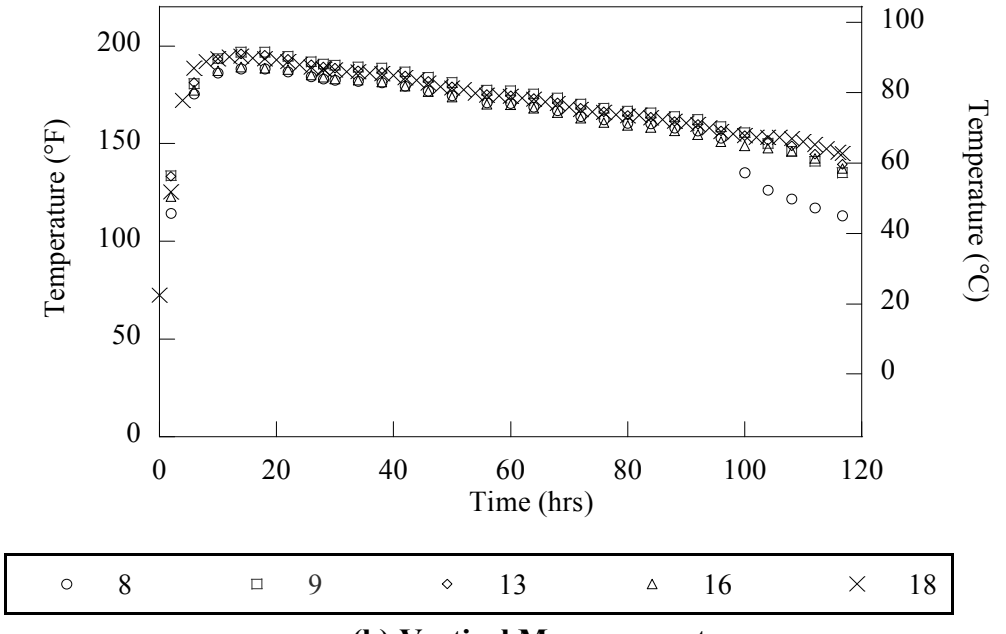

(b) Vertical Measurements

Figure 2-15 Typical Temperature History at Mid-span Section

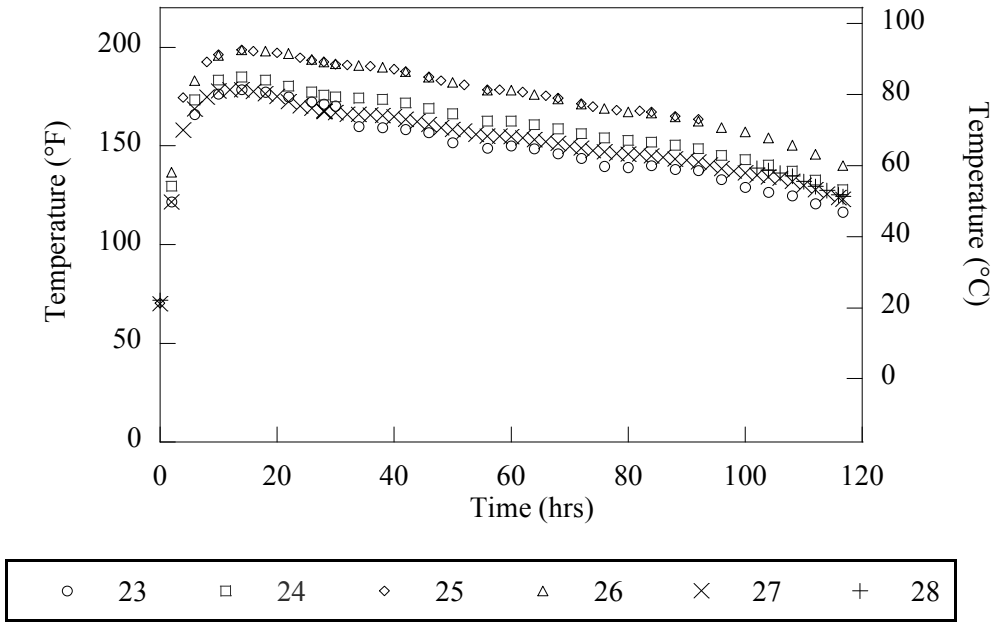

(a) Horizontal Measurements

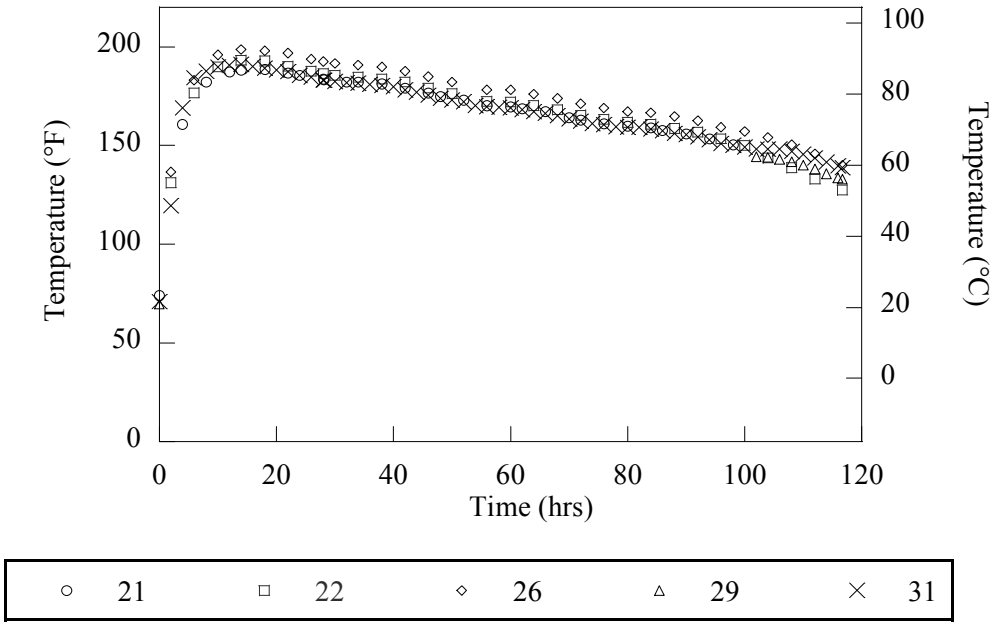

(b) Vertical Measurements

Figure 2-16 Typical Temperature History at Quarter-span Section

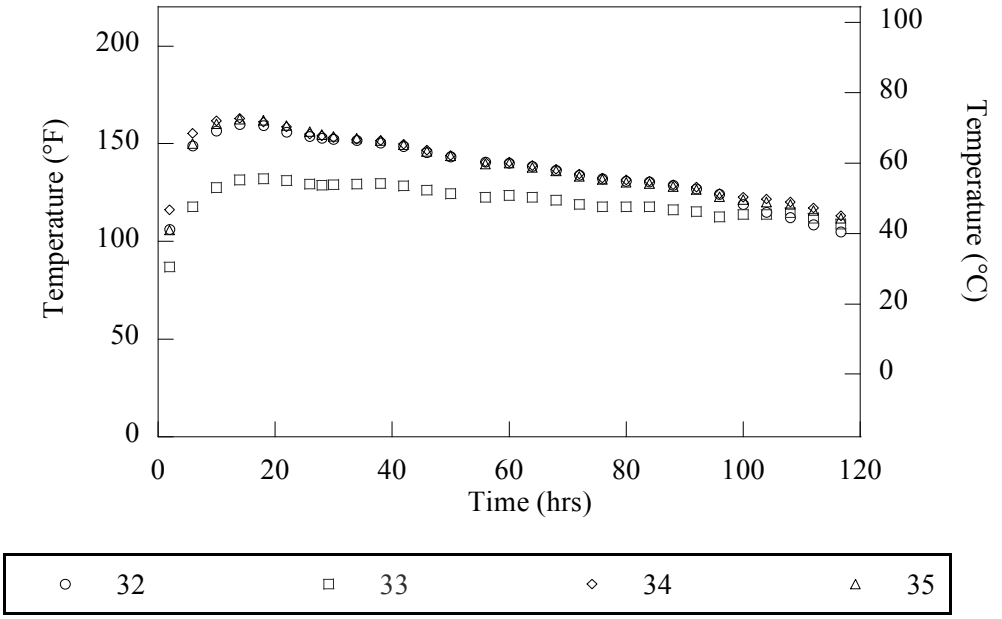

Figure 2-17 Typical Temperature History at End-span Section

2.3. Materials of Construction

The materials used in this research are discussed in this section. This is not an exhaustive analysis of the materials, but describes the type of materials used and some of the defining properties. More information and details on the materials used in this project are available in the materials report provided at a later date.

2.3.1. Coarse and Fine Aggregates

Aggregates were selected based on reactivity to promote ASR in the concrete, and therefore, not necessarily selected merely on price and location. The coarse aggregates had a maximum size aggregate (MSA) of 1 in (25.4 mm) and were river gravel from Hanson Aggregates in Garwood, Texas. Aggregates were transported from the quarry to the Texas A&M Riverside campus at the beginning of the project and stored to ensure one source for testing. Figure 2-18 shows the gradation curve of the coarse aggregates.

Fine aggregates were procured from Wright Materials in Robstown, Texas and stored next to the coarse aggregates at Riverside Campus. Figure 2-19 shows the gradation curve of the fine aggregates used in the concrete.

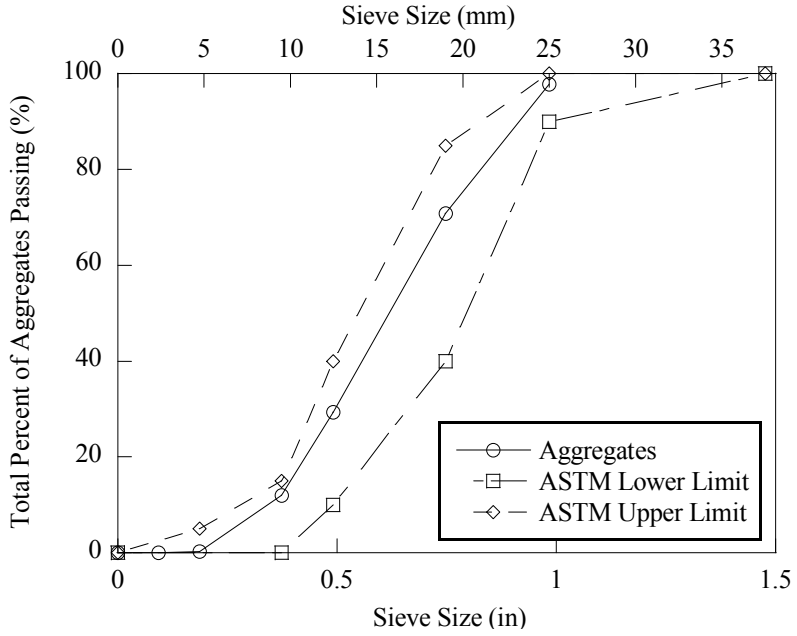

Figure 2-18 Gradation of the Coarse Aggregates

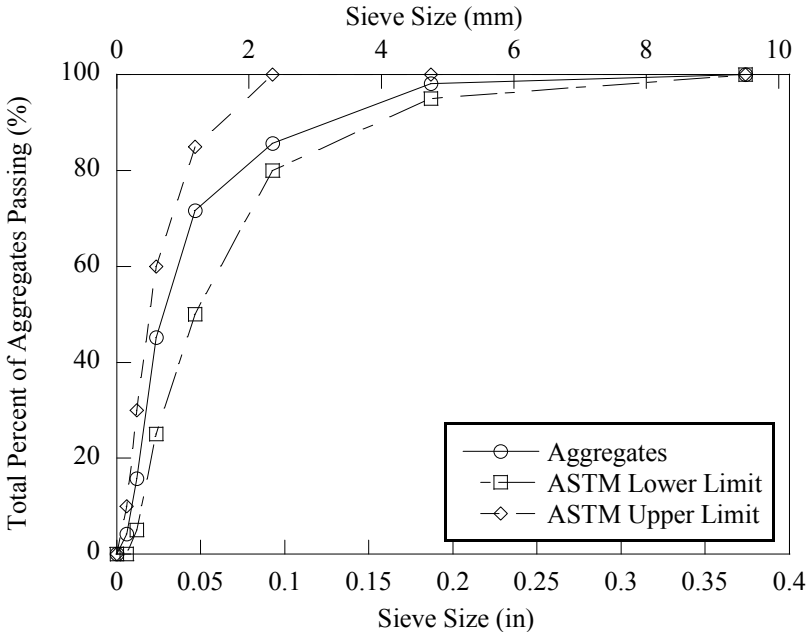

Figure 2-19 Gradation of the Fine Aggregates

Table 2-1 shows the measured properties of both coarse and fine aggregates. These properties were measured in accordance with ASTM C136 (Standard Test Method for Sieve Analysis of Fine and Coarse Aggregates), ASTM D 75 (Standard Practice for Sampling Aggregates), ASTM C 127 (Standard Test Method for Density, Relative Density, and Absorption of Coarse Aggregates), and ASTM C 128 (Standard Test Method for Density, Relative Density, and Absorption of Fine Aggregates).

Table 2-1 Measured Aggregate Properties

	Saturated Suface-Dry Density (g/cm^3)	Dry Density (g/cm^3)	Water Absorption (%)	Fineness Modulus
Coarse Aggregates	2.57	2.55	0.68	3.9
Fine Aggregates	2.58	2.55	1.44	2.79

2.3.2. Cement

Type III cement was used to fabricate all LSC specimens. The cement was procured from Lehigh Cement in Evansville, Pennsylvania, and transported to Texas A&M University in bags on pallets, and stored indoors. This particular cement was used because of the high alkali content to promote ASR in the LSC specimens. Table 2-2 shows the chemical composition of the cement.

Table 2-2 Lehigh Cement Analysis

Compound	% Wt.
Na_2O	0.3
MgO	2.8
Al_2O_3	4.8
SiO_2	19.48
P_2O_5	0.16
SO_3	3.66
K_2O	0.88
CaO	61.63
TiO_2	0.2
Fe_2O_3	3.43
as Na_2O_e	0.88
Total	99.71
C_3S	55
C_2S	14
C_3A	7
C_4AF	10

2.3.3. Water

Concrete mixing water was taken from a hydrant at the Riverside Campus during the batching process and dispensed directly into the concrete mixing truck. The water source is potable.

2.3.4. Sodium Hydroxide

To further increase the alkalis in the concrete mixture, sodium hydroxide (NaOH) was added to the mix. 51.3 lbs (23.3 kg) of NaOH tablets were mixed into a total of 21.1 gallons (80 L) of water in 4 containers. This created a supersaturated solution, which

was poured into the concrete mixing truck before the NaOH could settle from the solution.

2.3.5. Mix Quantities

The target compressive strength of the concrete mixture was 5000 psi (34.5 MPa). The specific quantities used in each specimen differed slightly due to the moisture content of the coarse and fine aggregates measured during the batching process. Table 2-3 shows the mixture characteristics and Table 2-4 shows the mixture proportions used for the LSC specimens.

Table 2-3 Mixture Characteristics

	Mix Values
coarse aggregate (absorption capacity) (%)	0.96
fine aggregate (absorption capacity) (%)	0.65
NaOH	51.3 lbs in 21.14 gallons (23.3kg in 80L)
anticipated air content (%)	1%
specific gravity of the cement	3.15
specific gravity of the coarse aggregates	2.57
specific gravity of the fine aggregates	2.65

Table 2-4 Mixture Proportions

Material	**SSD (lb/yd^3)**
Cement	752
Course Aggregate	1350
Fine Aggregate	1438
Water	361
NaOH	5.7
water/cement	0.48

2.3.6. Reinforcement Steel

Grade 60 reinforcing steel meeting ASTM A615 specifications was used to fabricate the LSC specimens.

2.4. Fabrication Procedure

Fabrication of the LSC specimens began in the summer of 2007. During the initial casting operations, the concrete began to flash-set and honeycombing was observed (see Figure 2-20). The flash-set was due to the Type III cement and the supplemental heating of the aggregates (to very high temperatures) used to promote DEF. Lack of control of temperature when heating the aggregates led to boiling of the water, which led to accelerated set times and introduced additional voids as shown in Figure 2-20.

Figure 2-20 Voids in the First Trials

This challenge required a new approach for fabricating and casting the LSC specimens. Because heating the water required for the mix to attain the 160 °F threshold for DEF was not an option due to the large quantity, two other possibilities were considered. The aggregates could be heated using a large aggregate furnace (used to batch asphalt), or electrical heating wires could be used to heat the concrete once it was placed. After investigating the asphalt batching plants and considering the costs and lack of control, the aggregate heater option was deemed unfeasible. In contrast, the electrical heating wires provided many benefits including the ability to regulate the heat using a feedback closed system with thermocouples. The heating wires were also much more cost effective, easier to implement, and safer in regard to the risk of fire hazard.

2.4.1. Reinforcement Cage Assembly

The longitudinal reinforcement consisted of twelve #11 bars that lapped over the middle 9 ft (2.74 m) of the LSC specimens. The transverse reinforcement consisted of #5 hoops placed at 12 in (305 mm) on center in the splice region and two overlapping #5 hoops placed at 6 in (152 mm) on center outside the splice region to deter failure in these regions. Figure 2-21 shows the individual bar details of the cage and the quantities of each for one specimen.

Starting with Bar A, the top bars were suspended above the ground using a fabricated stand and tied together over the a 9 ft (2.74 m) splice length. Careful placement of the instrumented bars allowed for the strain gages to remain untouched during the assembly of the reinforcement. The hoops, Bar C, were then placed over the longitudinal bars and the ends were tied together. Figure 2-3 and Figure 2-4 show overlapping hoops spaced at 6 in (152.4 mm) on the ends and a single hoop 12 in (304.8 mm) in the splice region. The top corners of the hoops were then tied to the longitudinal bars.

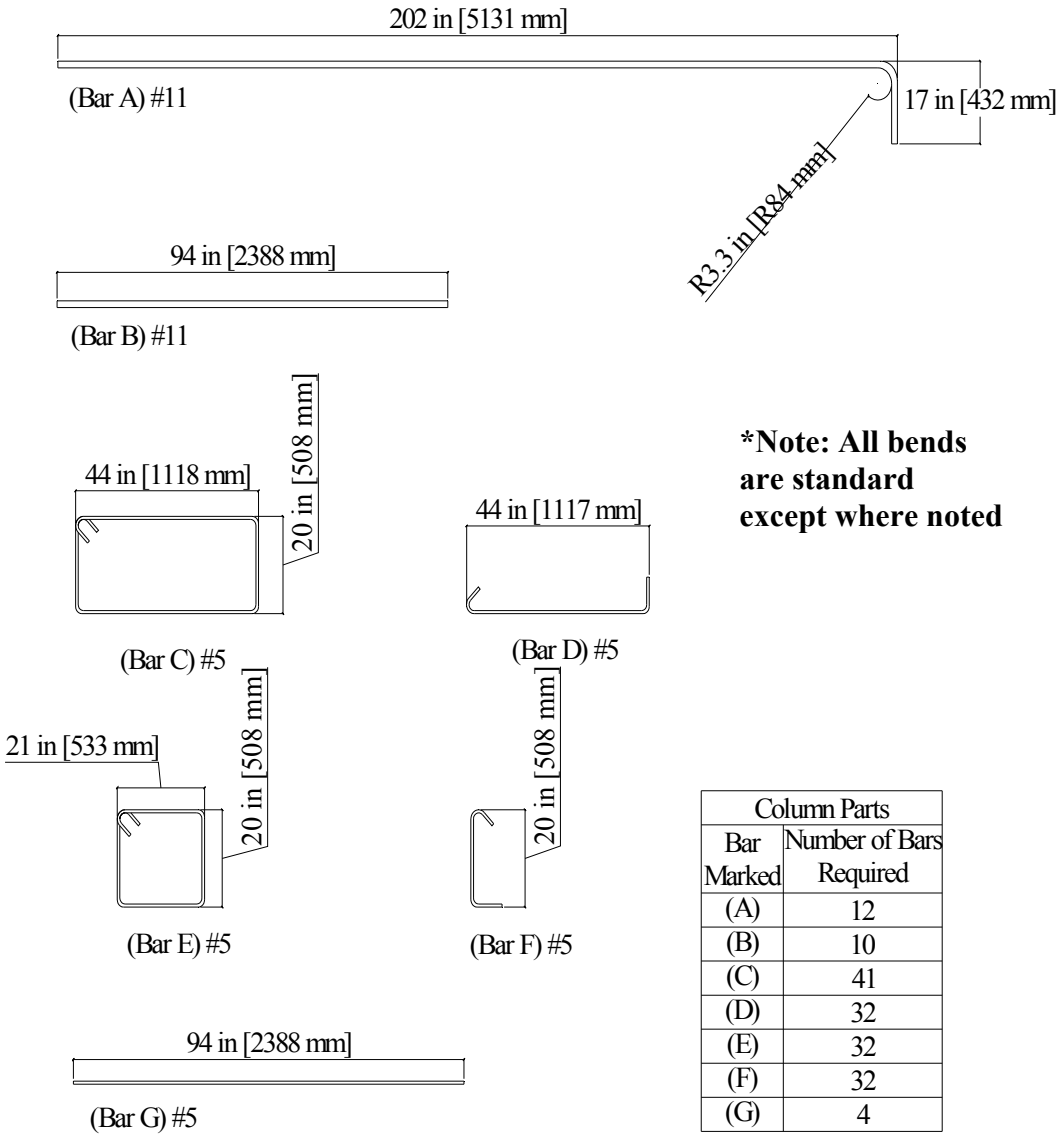

Column Parts	
Bar Marked	Number of Bars Required
(A)	12
(B)	10
(C)	41
(D)	32
(E)	32
(F)	32
(G)	4

Figure 2-21 Rebar Types, Quantities, and Dimensions

The pieces labeled Bar B were then slipped underneath the top side of the hoops on both sides of the center longitudinal bars. This allowed for the Bar E pieces to be placed around the center longitudinal bars and the Bar B bars in the end regions. The ends of the Bar E were tied together, centered, and attached to the hoops. Bar E was not used in the splice region of the column. Figure 2-4 shows the reinforcement layout as viewed from the ends of the LSC specimens at sections A-A and B-B in Figure 2-3.

With the hoops in place, the bottom longitudinal bars, including the two with strain gages were set in place and tied to the hoops in the corners. This allowed for the final pieces, Bar F and Bar D to be tied into place along the horizontal center and the vertical third point respectively. Bar G was used to hold Bar D into place and ensure accurate placing.

The last step of the reinforcement cage assembly was to attach chairs to the bottom of the cage to ensure the desired cover of 2 in (50.8 mm) was attained during the pour. With a spacing of 12 in (308 mm) in every direction, the chairs were tied to the reinforcement before placing in the form.

2.4.2. Strain Gage Application

Research was performed to ensure that the SGs would be readable and accurate after several months of exposure. The technique for applying the SGs to the rebar is outlined in a report by Liu et al. (2009). The ribs on the reinforcing steel were ground flat and then sanded to create a smooth surface for SG application. The SGs were glued to the reinforcing steel and covered with a series of protecting layers to ensure durability of the gages.

2.4.3. Post Tension Strand Installation

Once the reinforcement cage was placed into the formwork, the PT strands were put into place through the formwork. The plastic tubing for unbonding the strands was cut off the ends and the strands were placed through the anchor plates on the ends of the formwork. A hydraulic jack was used to put a slight tension on the strands until the sag was removed from the middle. Ties were also used to suspend the PT strands to avoid excessive sagging. After the concrete gained sufficient strength, the strands were then tensioned to the desired 36.3 kips (161.5 kN) as discussed in Section 2.1.1.

2.4.4. Electrical Resistive Wiring Installation

To promote DEF, the LSC specimens were supplemented with heat by Electrical Resistive Wiring (ERW) to ensure that the concrete temperature was above 160 °F (71.1 °C) during the curing of the concrete. The ERW was preinstalled in the bottom and top forms and then covered with stainless steel. In addition, ERW was required in the mid depth of the LSC specimens by one dimensional heat flow analysis. The ERW was pushed through PEX tubing that was strung through the vertical center of the cross section of the LSC specimens at four-points and passed through the end of the form (see Figure 2-22). This protected the ERW and allowed for the wire to be used multiple times. The ERW solution consisted of three controllable sections to apply heat, which allowed for a more uniform temperature distribution in the concrete throughout the specimen.

(a) ERW in the Top Panels (Plan View)

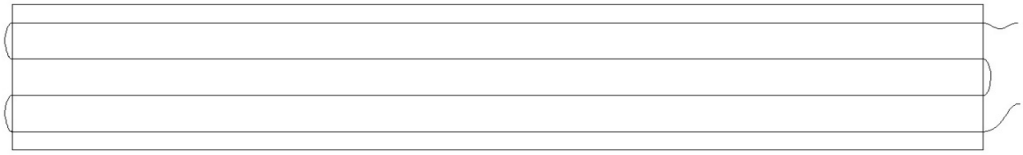

(b) ERW Through the Middle of the Concrete (Plan View)

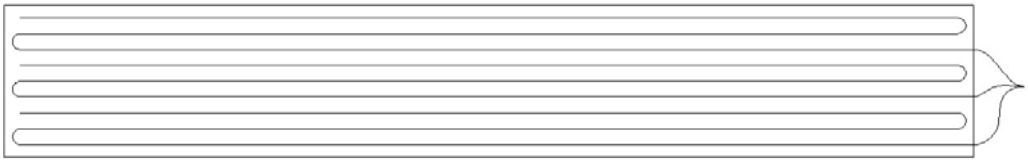

(c) ERW Embedded in the Bottom of the Form (Plan View)

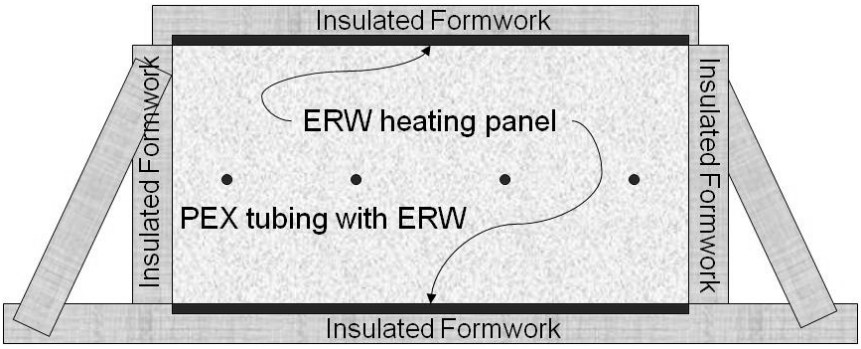

(d) End-View of Heated Formwork

Figure 2-22 ERW Layouts

2.4.5. Batching and Mixing Concrete

Concrete for fabricating the specimens was mixed using a concrete truck. Using a front-end loader and a forklift, the fine and coarse aggregates were first loaded into the truck as shown in Figure 2-23. The front end loader was used to fill a 2 yard bucket with up to 4000 lbs (17.79 kN) of material. Then the forklift would lift the bucket using straps and a load cell to weigh the aggregates. With the weight recorded, the forklift then set the bucket on the ground. From there, the bucket was picked up using the forks and lifted above the truck. The material was then dumped into the truck and the process was repeated until the required amount of fine and coarse aggregates were added to the truck. Aggregate weights were adjusted for moisture prior to mixing. Water was then added. The truck was filled with the prescribed amount of water minus 21.14 gallons (80 L), which was added later with the Sodium Hydroxide (NaOH) tablets. This completed the batching operation at the Riverside campus. The concrete truck was then transported to the Structural and Materials Testing Laboratory at the Texas A&M University campus. In the Structures and Materials Testing Laboratory, sodium hydroxide tablets were batched into four 5-gallon containers and mixed with the water prior to the concrete mixing truck's arrival.

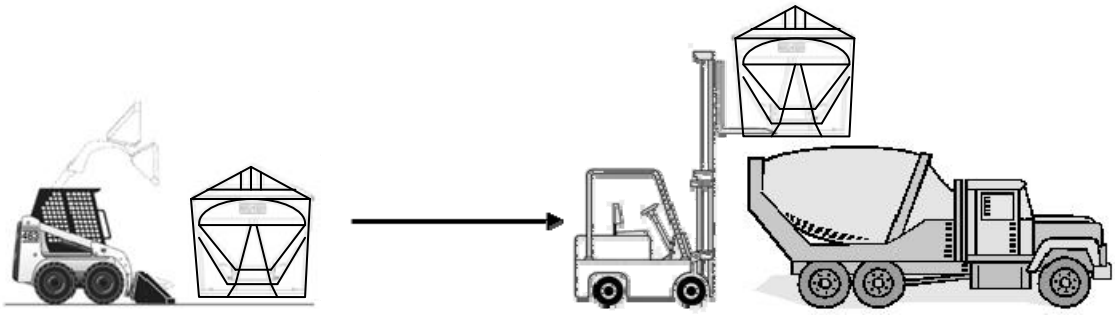

(a) Adding Fine and Coarse Aggregates

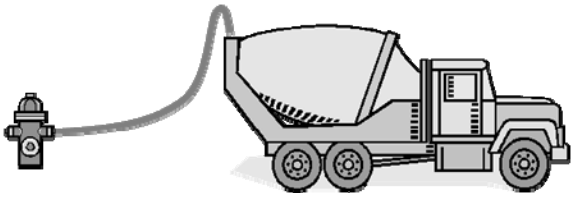

(b) Adding Water

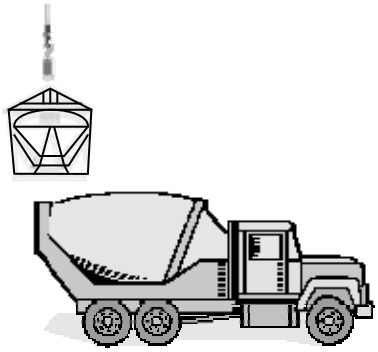

(c) Adding Cement

Figure 2-23 Batching Operations

After arrival of the truck in the Structures and Materials Testing Laboratory, the cement was added to the truck (see Figure 2-23c and Figure 2-24). After the cement was added, the 4 containers of sodium hydroxide solution were added into the mixer, which had an added benefit of washing the remaining cement into the mixer as it was poured into the drum. After adding the NaOH solution, the concrete mixing truck mixed the concrete materials for 15 minutes at high speed, which is typical for normal batching operations. Table 2-5 shows the approximate length of time for each operation of the batching process in the laboratory.

Figure 2-24 Dumping Cement into the Mixer

Table 2-5 Fabrication Procedure in the Structures and Materials Laboratory

Operation	Approximate Time
Add Cement to the Concrete Truck	30 minutes
Add NaOH solution to the Concrete Truck	5 minutes
Mix Concrete	15 minutes
Perform Slump Test	1 minute
Cast Concrete in LSC specimens Form	15 minutes
Finish Concrete (Screed and Bull Float)	30 minutes
Connect ERW	15 minutes
Cover LSC specimens with Insulating Panels	15 minutes

2.4.6. Casting Specimens

After the concrete materials were mixed for 15 minutes, a sample was taken from the mixer for a slump test according to ASTM C143 (2000). To assess slump loss over time, the slump was taken every 10 minutes. Figure 2-25 shows the slump loss for all 16 specimens.

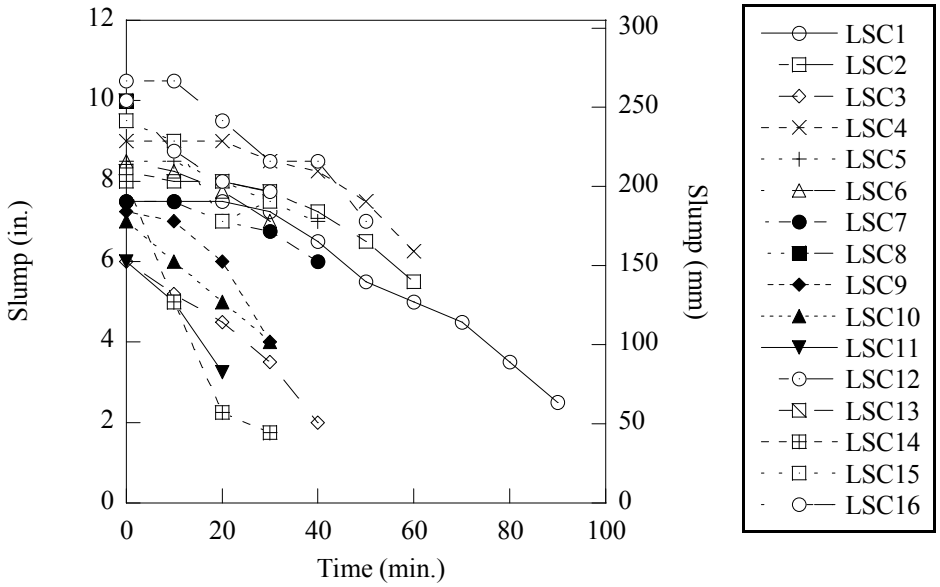

Figure 2-25 Slump Versus Time

Concrete was set aside to fabricate test samples. Test Samples included 4 in x 8 in (102 mm x 204 mm) cylinders for compressive strength testing according to ASTM C39 (2001), Fu prisms for DEF expansion measurements, prisms for ASR/DEF expansion measurement according to ASTM C1293 (2008), and prisms for flexural strength tests in ASTM C78 (2007). The details of each test sample are further discussed by the materials report provided at a later date.

Figure 2-26 shows the concrete placement. After the form was filled and the concrete consolidated, the concrete was screeded and floated. This process concluded the casting of the concrete.

Figure 2-26 Pouring Concrete in the Form

2.4.7. Early Age Specimen Conditioning

Shortly after the concrete was floated, the top ERW panels were placed directly on the concrete. Placed end-to-end, the panels covered the top of the specimen except for the last 6 in (152 mm) on the ends. The wires were routed out the sides of the form for connection to the power supplies. Insulated panels (6 in [152.4 mm] thick), were then placed on top of the ERW panels to reduce heat loss as shown in Figure 2-27. These ran the length of the form and completed the insulated form, entombing the specimen. The ERW was connected to the power supplies which controlled the temperature of the concrete to 180 °F (82 °C) in the bottom, middle and top of the specimen. The ERW was run for 2 to 3 days and then switched off to allow the specimen to gradually cool.

Figure 2-27 Insulated Form with ERW Power Supplies on Top

During the curing process, the data acquisition system (DAQ) logged data for all sensors in the specimen. The data from the strain gages fluctuated during the placement of the concrete and the heat application period. However, once the heat was switched off and the specimen began to cool, the strain gages stabilized.

The cooling process consisted of disconnecting the ERW from the power. The top insulation boxes and ERW panels were then removed the next days to allow for further heat loss. After an additional 1 to 3 days, the side forms were removed to allow the specimen to reach room temperature. At this point, the strain gages had reached a stable value and this value was considered as the zero point for testing at a later date.

This concluded the placement procedure. Constructed specimens were stored in the lab until four specimens were completed. Once the fourth specimen was fully completed, the four specimens were transported to the Riverside campus for atmospheric exposure.

2.5. Summary

Fourteen specimens were constructed and transported to the Riverside campus for deterioration and two control specimens remained in the lab without any premature concrete deterioration. The fabrication process for all 16 specimens lasted from January of 2008 to September of 2008. Due to the research done on the front end of the project, each LSC specimen had minimal voids and were exposed to the summer heat as soon as possible.

3. DETERIORATION OF LARGE-SCALE SPECIMENS

3.1. Introduction

Multon et al. (2005) reported that the effects of water substantially increased the amount of ASR in a specimen half submerged in water. Folliard et al. (2008) reported that ASR progresses faster in a warmer climate than a colder climate. Hence, to promote the formation of ASR and DEF, the LSC specimens were stored in atmospheric conditions in Texas and exposed to wetting for 15 minutes four times a day. Normally ASR and/or DEF takes many years to exhibit damage and cracking. However, due to the materials selected, the fabrication process, and the exposure conditions of wetting/drying cycles used in this research project, the LSC specimens are expected to deteriorate more rapidly.

3.2. Specimen Exposure Conditions

The LSC specimens were placed on their short side (2 ft dimension) at about 3 ft (0.91 m) clear distance between the specimens. Figure 3-1 shows the placement of the LSC specimens at the Riverside Campus. To accelerate the ASR/DEF deterioration mechanisms, a watering system was installed to wet each side of a specimen for 15 minutes every 6 hours. Figure 3-2 shows that during normal wind conditions, the entire specimen, minus the specimen ends, were soaked in water.

Figure 3-1 Specimens Exposed to Atmospheric Conditions at Riverside Campus

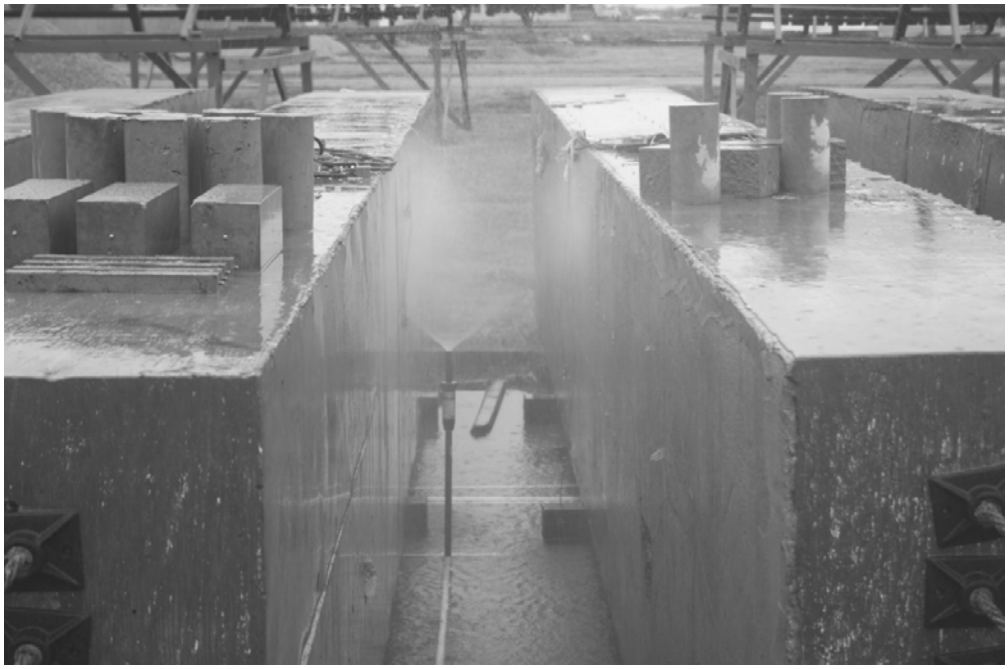

Figure 3-2 Sprinkler System between Two Specimens

3.3. Specimen Behavior during Deterioration Phase

DEMEC strain measurements, strain gages on the reinforcing steel, embedded concrete gages, and crack width measurements were taken and recorded every two weeks. As outlined in Section 2.2, the DEMEC points, embedded concrete gages, and strain gages were installed prior to placement at Riverside. LSC1 through LSC6 were stored outside for up to 3 months before the sprinkler system was installed. The strain measurements were recorded during that time, but little expansion was apparent until the sprinkler system was installed. Therefore, all data and results in this report use the initial time of exposure to the wet/dry cycles as time equal to 0.0, not the time after casting.

3.3.1. Strains between DEMEC Points

DEMEC points mounted on the surface of the LSC specimens provide measurements for surface expansion. Calipers were used to measure the distance between the points with a precision of 0.0005 in (12.7 μm), which corresponds to a resolution of approximately 50 microstrain on the readings. Coupled with errors during the measurement process, the values obtained were found to have an error of approximately +/- 100 microstrain. As the strains approach 5000 microstrain or larger, the error measurement is about 2%.

Figure 3-3 and Figure 3-4 show the average transverse surface expansion along the short and long sides of the LSC specimens during the first 300 days of exposure to the wet/dry cycles. The transverse surface strain for each set of DEMEC points is calculated by averaging the measured lengths between DEMEC points on each cross section as follows:

$$\delta_i = \sum_{i=1}^{n} \frac{L_{existing} - L_{initial}}{L_{initial}} \tag{3.1}$$

where $L_{existing}$ is the current transverse length between the DEMEC points, $L_{initial}$ is the original transverse length before deterioration, and n is the number of DEMEC measurements on a line. This is done separately for the long and short sides of the LSC specimens. Two readings per section are used for the short side and four readings per section are used for the long side. Figure 3-3 and Figure 3-4 show the average transverse strain, δ_{total}, for all 12 DEMEC sections of the LSC specimens as follows:

$$\delta_{total} = \frac{\sum_{i=1}^{12} \delta_i}{12} \tag{3.2}$$

where δ_i is the transverse strain of one set of DEMEC points.

The measured strains on the short (top) side of the LSC specimens were almost two times higher than those on the long side of the specimen. This may be attributed to the warmer surface temperature due to exposure of direct sunlight. The short side receives direct sunlight from dusk till dawn, while the long side receives less than half the amount of time due to the east/west progression of the sun. Likewise, Figure 3-5 shows that the top of the long side is receiving more direct sunlight than the lower portion. This is because the longitudinal axis of the LSC specimens is oriented north-south, which means the sun passes over the specimens in the transverse direction.

Figure 3-6 and Figure 3-7 show the individual transverse strain measured on the top and bottom half of the long side of the LSC specimens. The figures show that the upper quarter of the long side is expanding more than the other section along the long side and are comparable to that on the short (top) side of the LSC specimens (see Figure 3-3). A combination between direct sunlight, higher temperatures, and ponding water on the top the LSC specimens could be the cause of this increase in expansion.

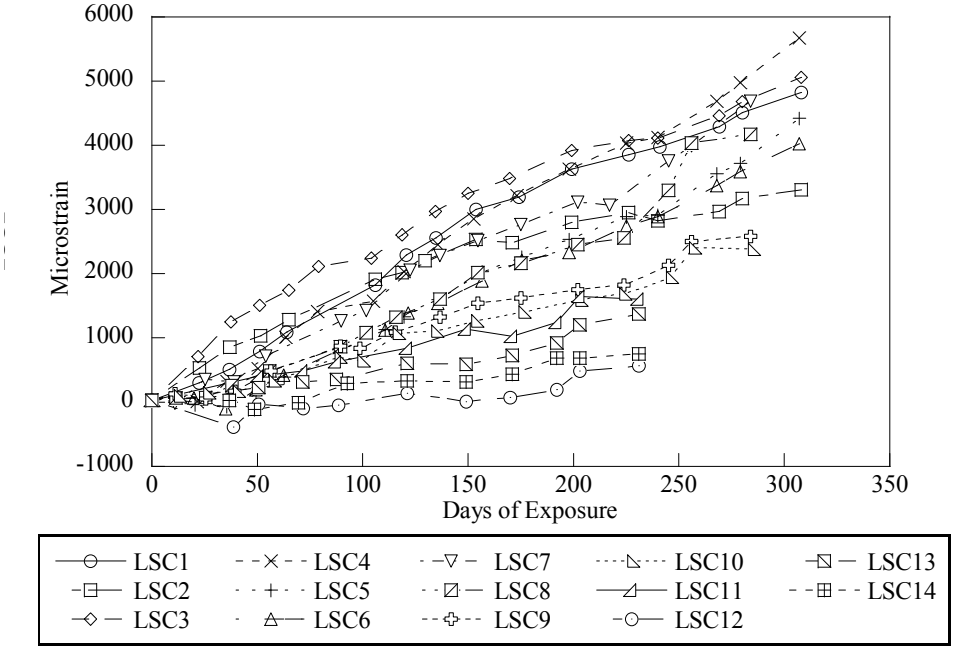

Figure 3-3 Transverse Surface Strains on the Short Side of the LSC

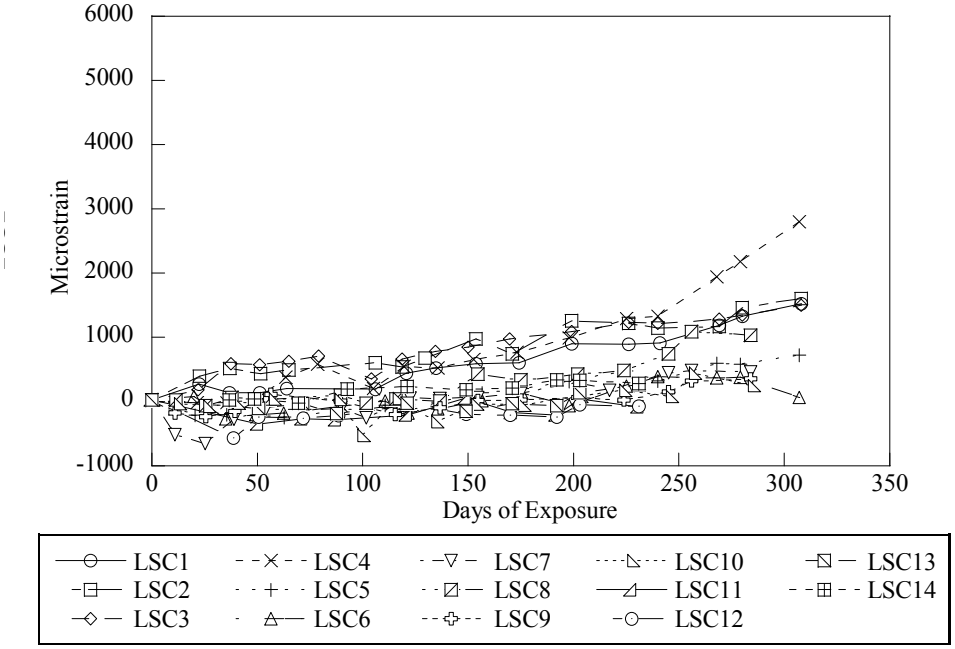

Figure 3-4 Transverse Surface Strains on the Long Side of the LSC

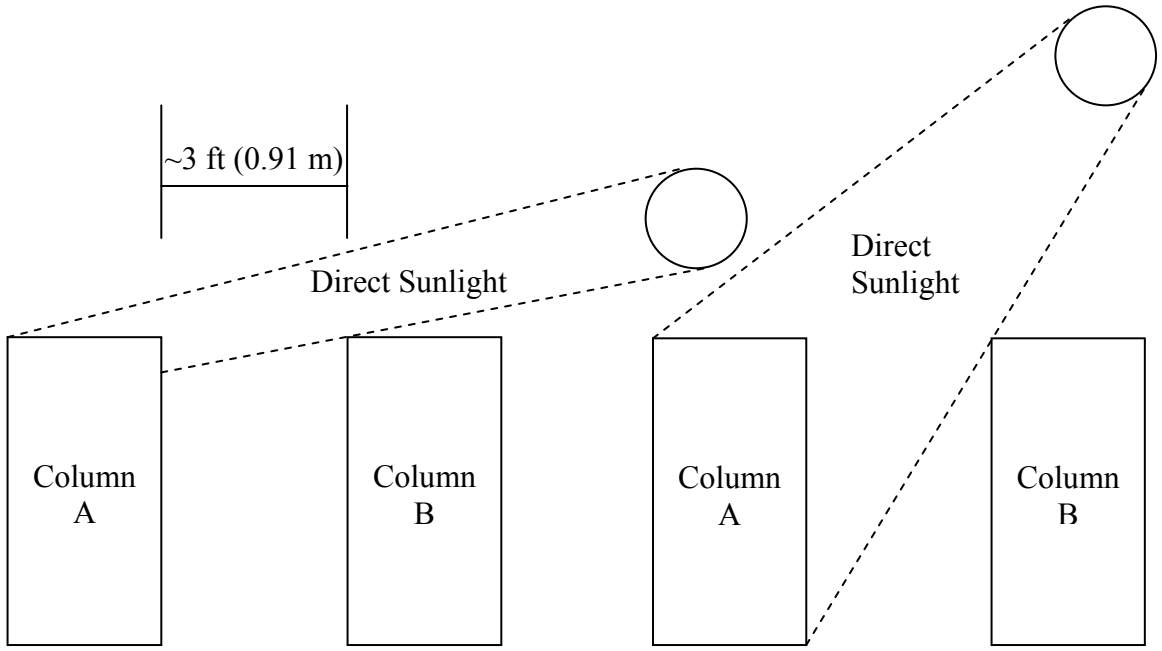

(a) Dawn/Dusk **(c) Morning/Evening**

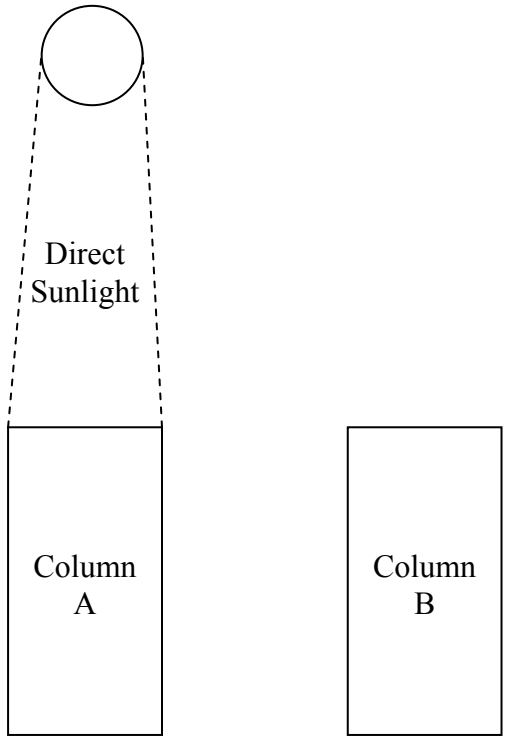

(e) Midday

Figure 3-5 Direct Sunlight Exposure of Columns at Riverside

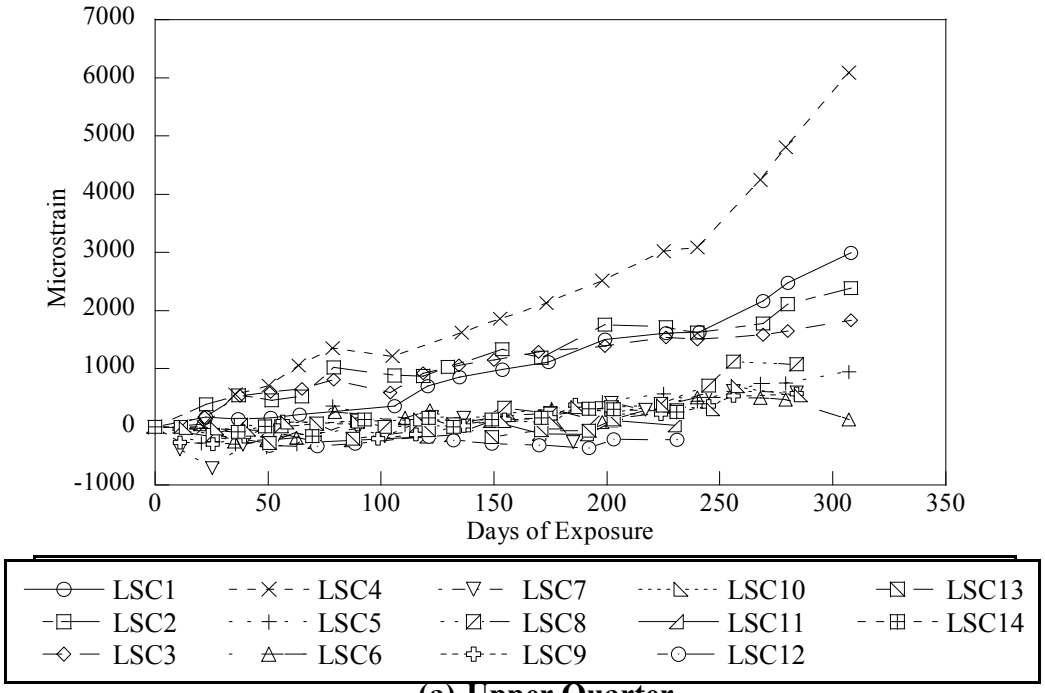

(a) Upper Quarter

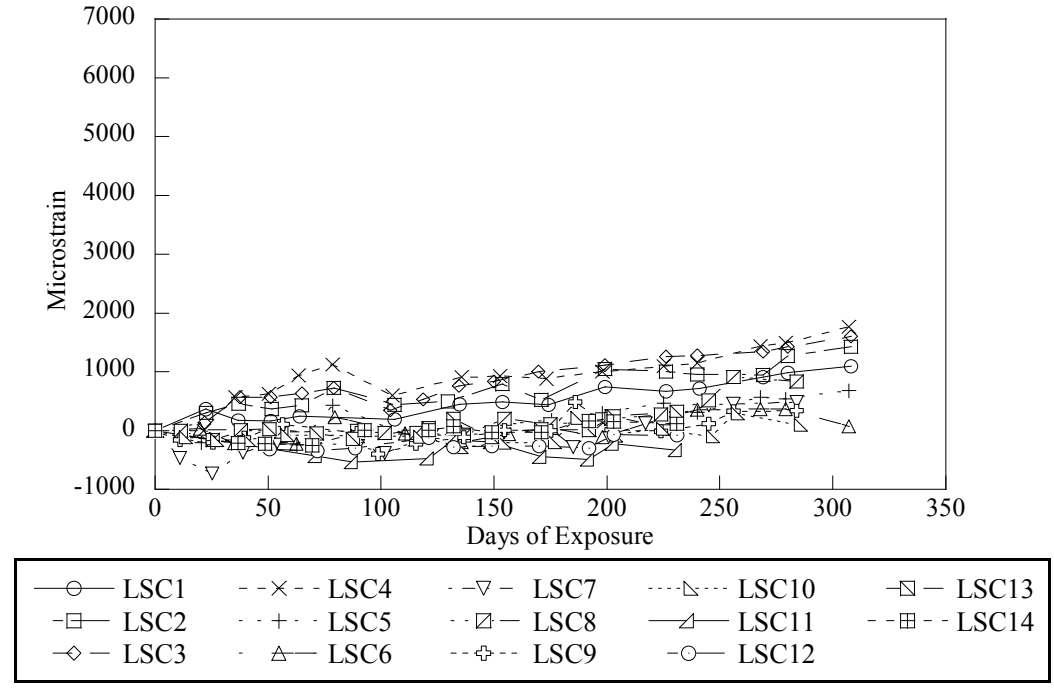

(b) Middle-Upper Quarter

Figure 3-6 Individual Transverse Strain Measurements on the Top Half of the Long Side of the LSC Specimens

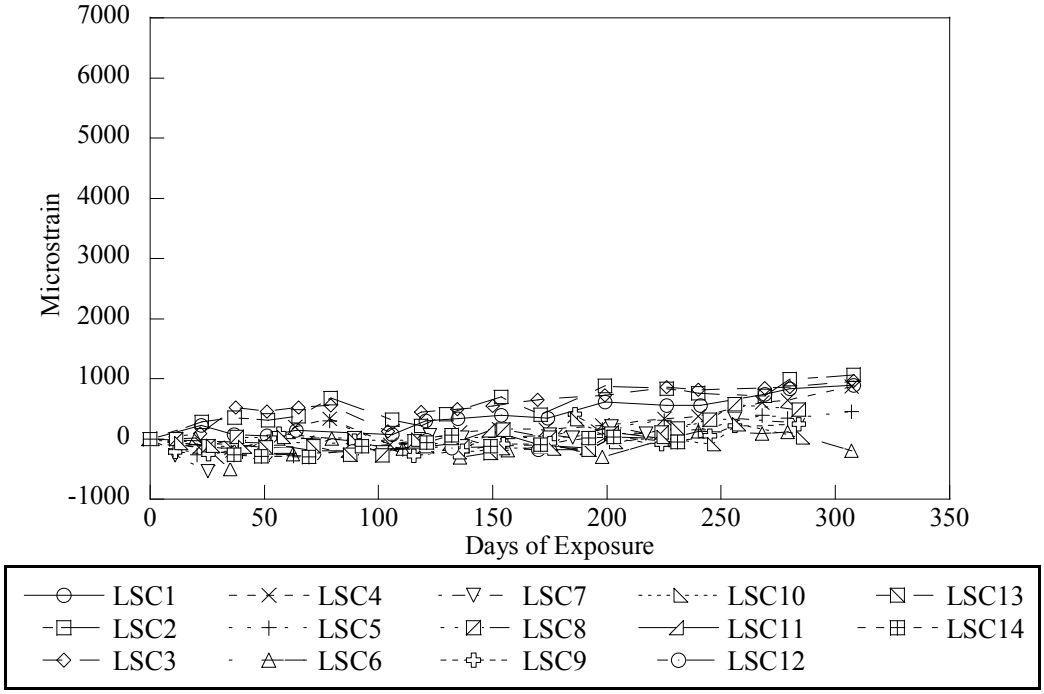

(a) Middle-Lower Quarter

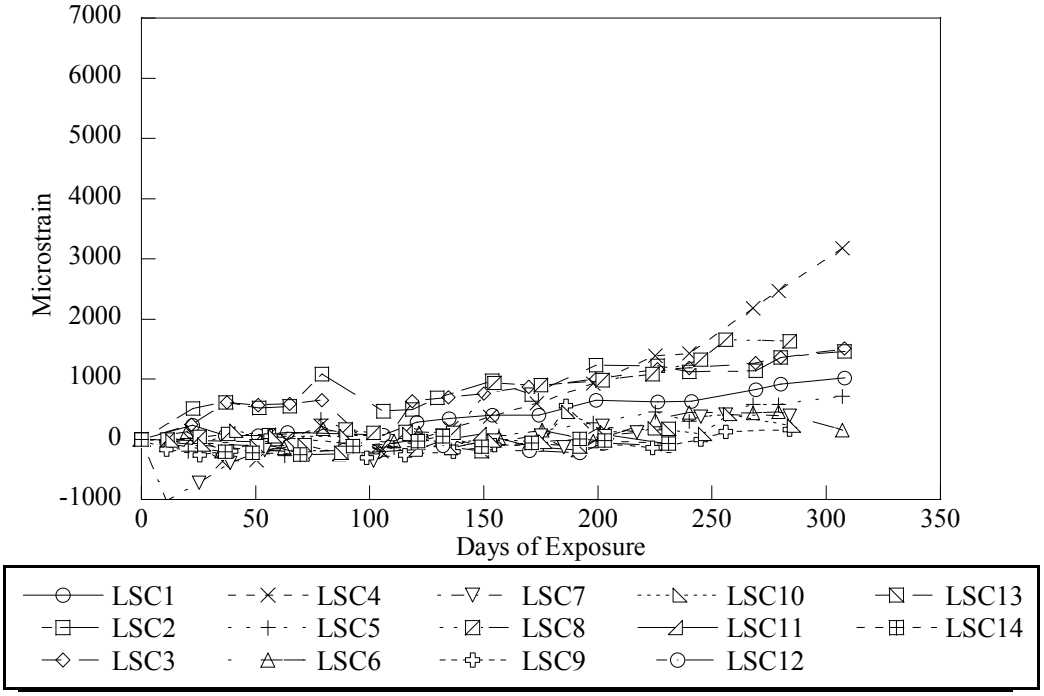

(b) Lower Quarter

Figure 3-7 Individual Transverse Strain Measurements on the Bottom Half of the Long Side of the LSC Specimens

3.3.2. Embedded Full-bridge Concrete Gage Measurements

During fabrication, 5 KM embedded concrete gages were installed into the concrete specimen. KM gages 1 and 2 were placed on the short side of the column with KM1 embedded 1 in (25.4 mm) from the surface and KM2 embedded 3 in (76.2 mm) from the surface (1 in [25.4 mm] inside the hoop). Likewise, KM3 and KM4 were placed on the long side with KM3 in the cover and KM4 embedded 3 in (76.2 mm) from the surface (1 in [25.4 mm] inside the hoop). KM1 through KM4 were placed to measure (column transverse expansive) strains and KM5 was placed on the long side perpendicular to KM3 and KM4 to measure column radial strains.

In Figure 3-8, the strains from KM1 and KM2 are shown for all 14 LSC specimens in the deterioration phase. These results indicate that the cover region of the specimens are expanding more than the confined concrete region within the hoops, most likely due to the hoops restraining the expansion. However, in Figure 3-9, the difference between the strains inside the hoop and outside is not as clear. This might be attributed to the long side having strains approximately only ~25% of the short side, again this may be due to the amount of exposure to sunlight. KM3 and KM4 are located at the center of the long side and therefore receive less sunlight than the upper half of the long side. In addition, it is evident that the trends found in both the DEMEC measurements and the KM gages are similar in magnitude on both the short and long sides of the column.

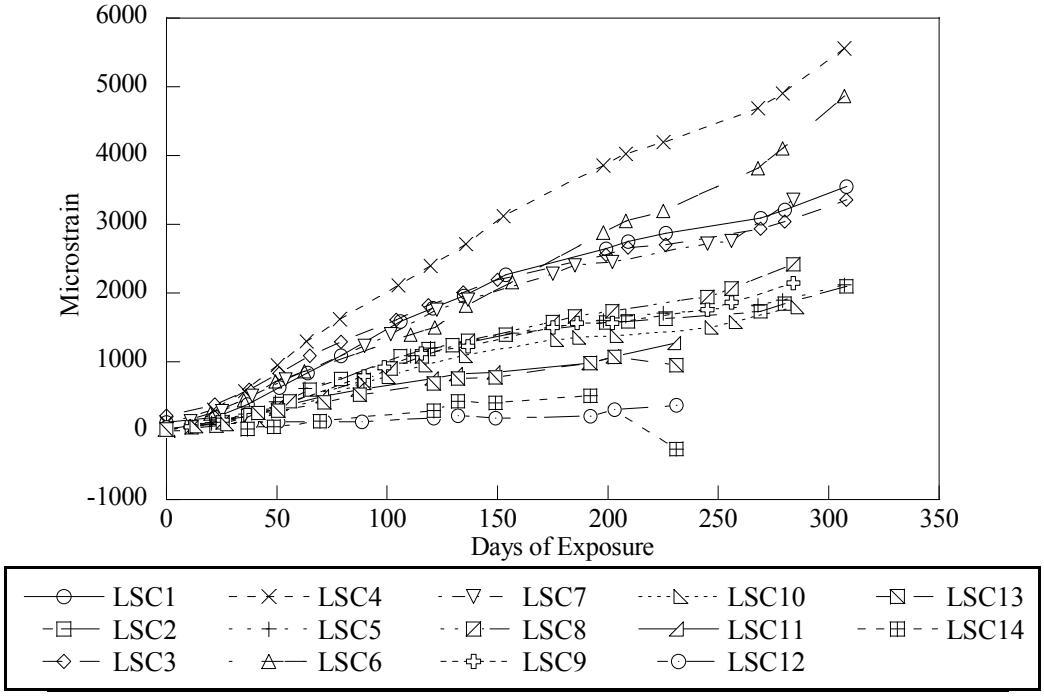

(a) KM Gage 1 – 1 in (25.4 mm) Outside the Hoop

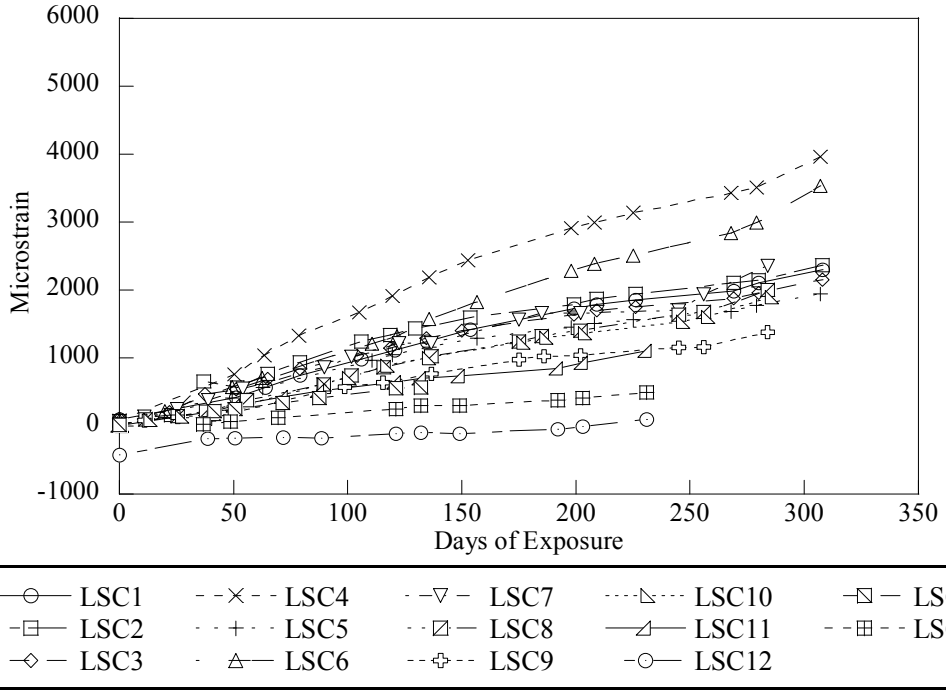

(b) KM Gage 2 – 1 in (25.4 mm) Inside the Hoop

Figure 3-8 KM Gage Transverse Expansion on the Short Side of the LSC Specimens

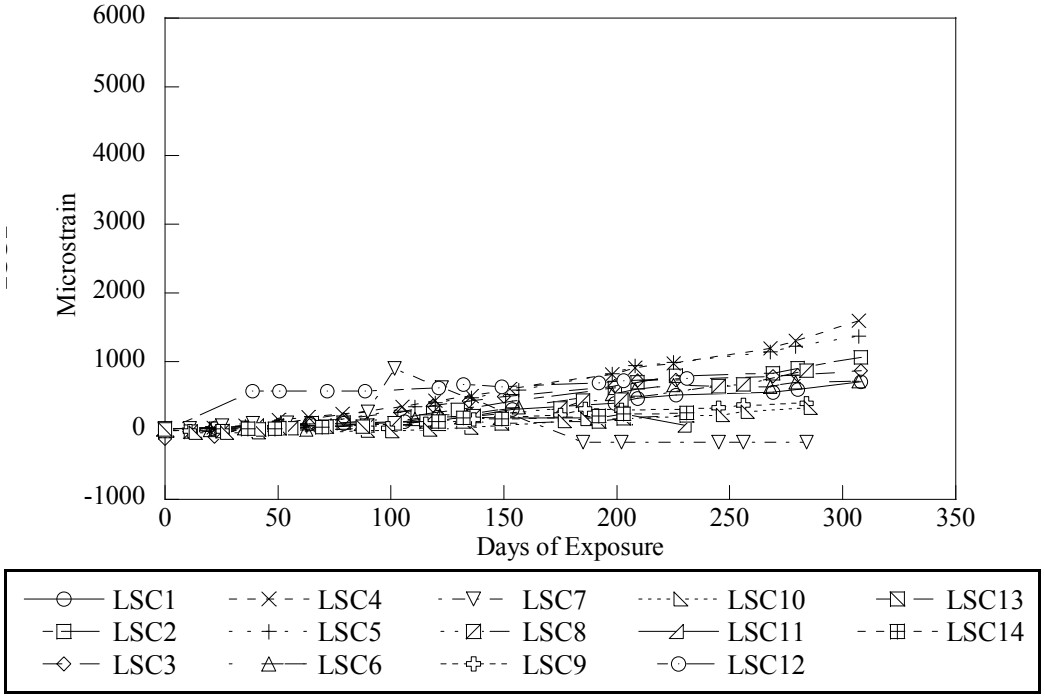

(a) KM Gage 3 – 1 in (25.4 mm) Outside the Hoop

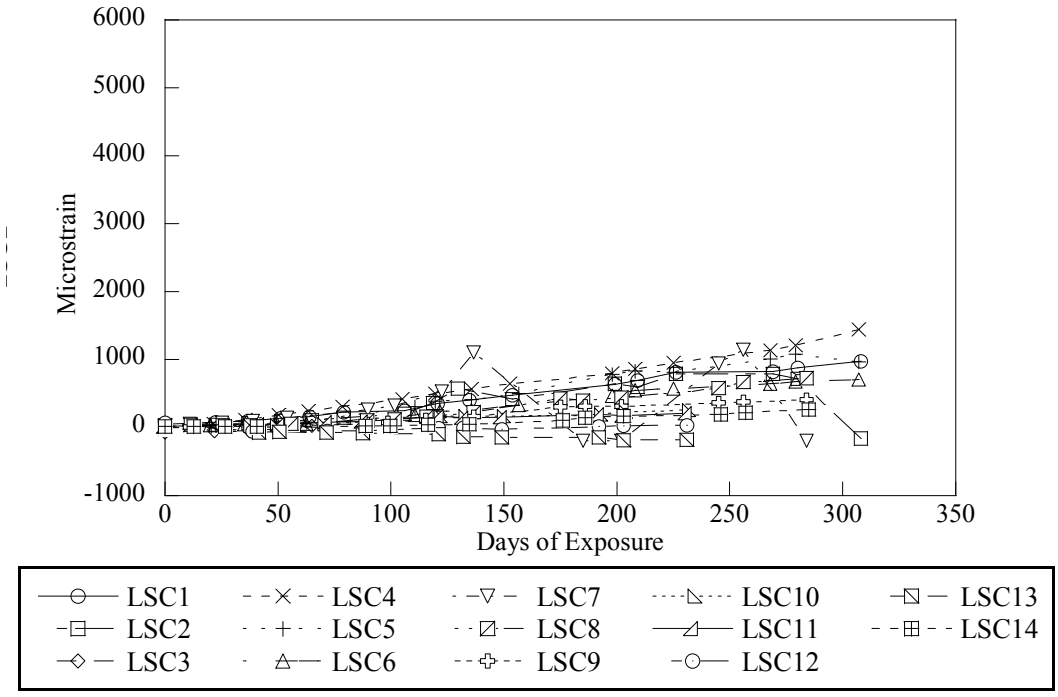

(b) **KM Gage 4 – 1 in (25.4 mm) Inside the Hoop**

Figure 3-9 KM Gage Transverse Expansion on the Long Side of the LSC Specimens

It can be observed that, in general, the KM gages on either side of the hoop have higher strains than the hoop itself. This might indicate that the local effects of the hoop reduce the expansion strains in the concrete since the KM gages are placed midway between the hoops (see Figure 3-10). However, Multon et al. (2005) found that stirrups had little to no effect on the transverse strains. Another possibility is that the discrepancy might be due to bond-slip condition in the reinforcement. Further measurements that will be collected later in the research may provide more insight into why the strains are smaller in the SGs on the hoops versus the KM gages in the concrete.

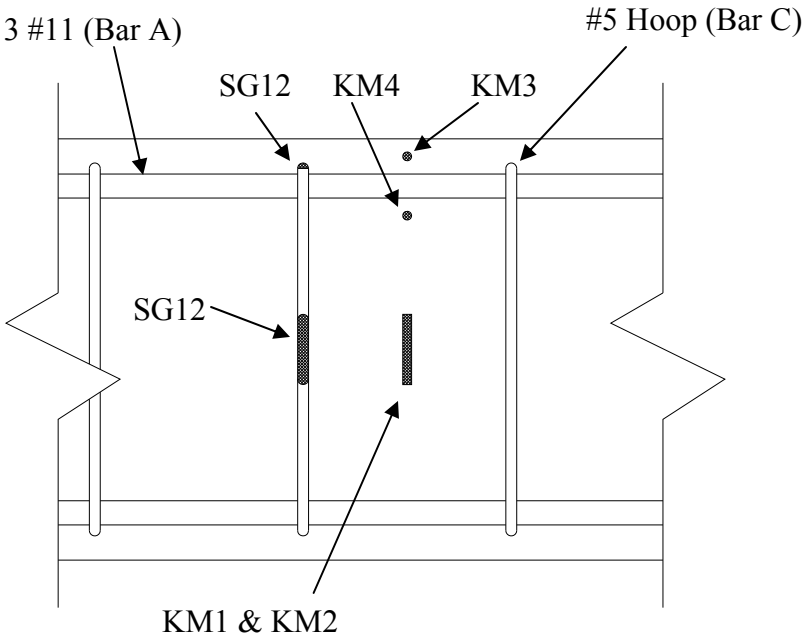

Figure 3-10 Location of the KM Gages Relative to the Hoops

3.3.3. Strain Gage Measurements

A total of 12 strain gages (SG) were attached to the reinforcing steel of each specimen as discussed in Section 2.2.2. Two gages, SG11 and SG12, were applied to a hoop reinforcement to measure transverse expansions along the short and long sides of the specimen respectively. The remaining strain gages are used during load testing. SG11 and SG12 were placed in the center of the short side and the third point of the long side respectively. Because of SG12's placement on the upper portion of the long side, higher strains were observed when compared to the average DEMEC measurements of the long side and the KM gages, which are centered on the side. Figure 3-11 and Figure 3-12 show the expansion of SG11 and SG12, respectively. The strains on the short side are marginally higher than the strains on the long side. On the short side of the hoop, the data indicates that the reinforcement steel has begun to yield (strain > 0.002) in LSC specimens 4 and yielding may occur soon in the other specimens.

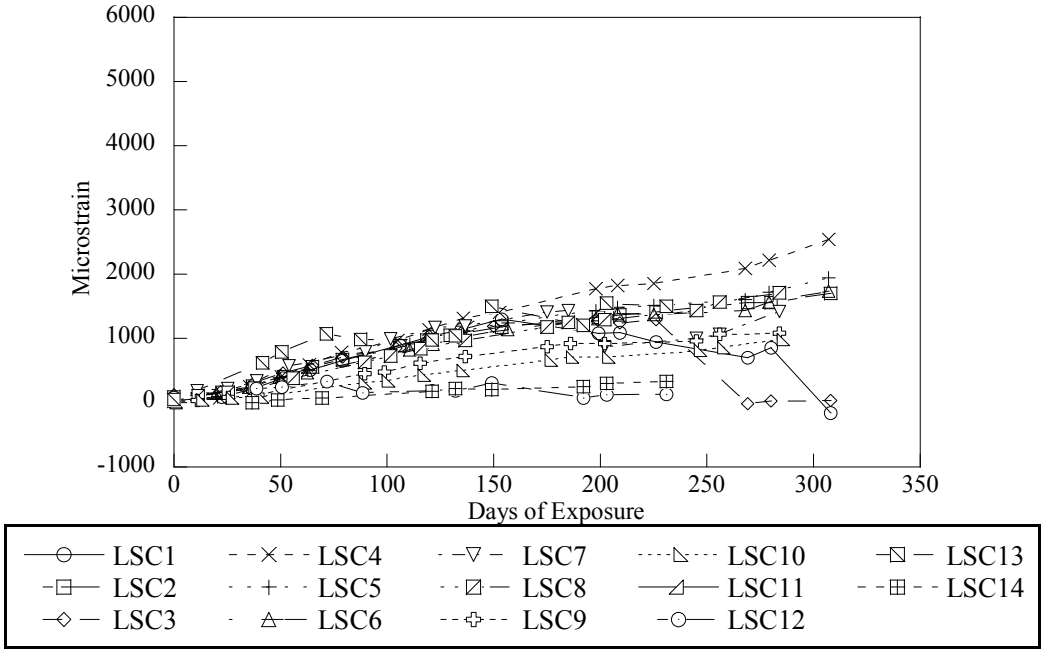

Figure 3-11 Strains in the Hoop on the Short Side of the LSC Specimens (SG11)

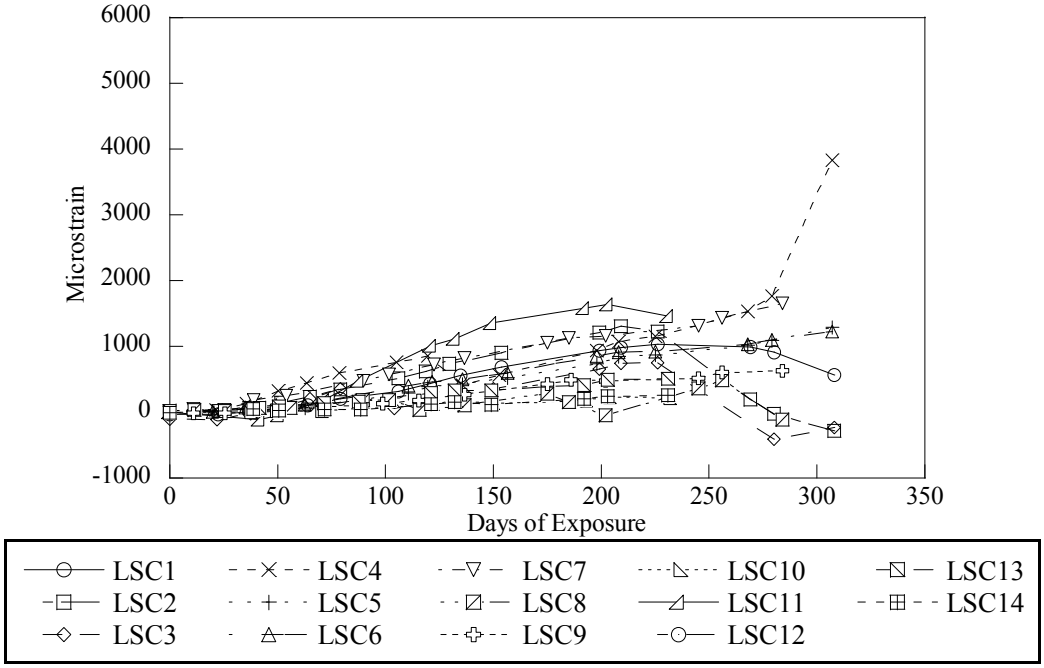

Figure 3-12 Strains in the Hoop on the Long Side of the LSC Specimens (SG12)

3.3.4. Crack Width Measurements

Figure 3-13 shows a longitudinal crack beginning to form on a LSC specimen. The cracks were measured with a crack comparator card that can be used to visually assess crack widths as small as 0.005 in (0.13 mm).

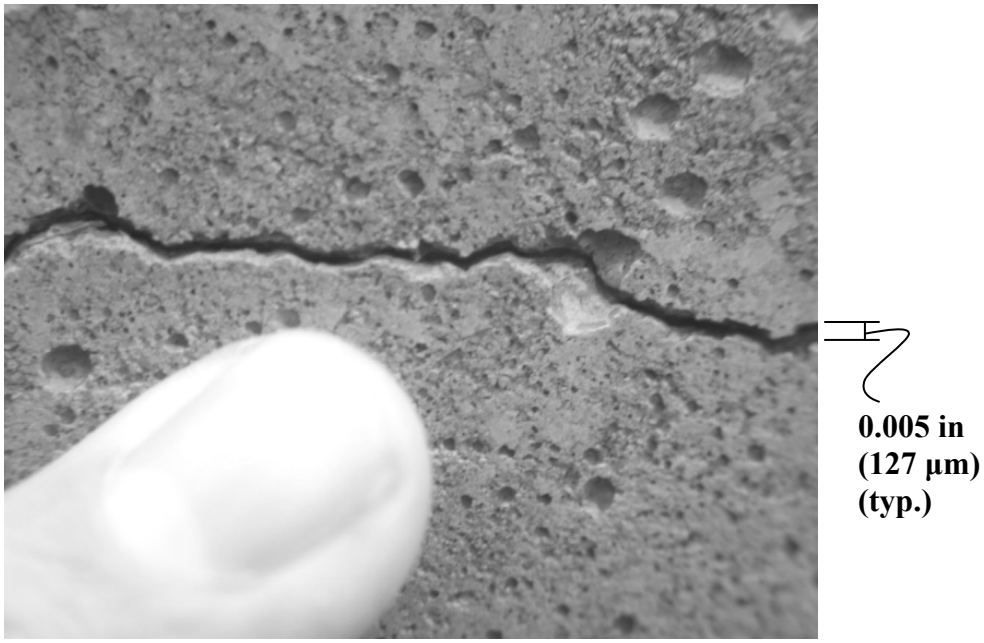

Figure 3-13 Longitudinal Crack from ASR/DEF Expansion

To obtain an equivalent strain across a section, the cracks between DEMEC points were measured and summed to obtain the total expansion across the specimen side. The total expansion was then divided by the original length between the DEMEC points and an equivalent strain, δ, was determined as follows:

$$\delta = \frac{\sum crack\ widths}{Length\ between\ DEMECs} \tag{3.3}$$

Figure 3-14 shows the recorded data from the cracked columns. The data does not start until after 100 days of exposure because prior to this, the cracks were very small or did not exist. This method results in significantly lower values of surface strains as compared to the DEMEC measurements in Figure 3-3. This is due to the inability to capture strains in the concrete in between the cracks. As the columns continue to crack, the data will be compared to the DEMEC data and strain gage data to identify if a correlation exists between summing the crack widths and the actual strains inside the column. This could allow for simple diagnostics to be performed on deteriorated columns in the field.

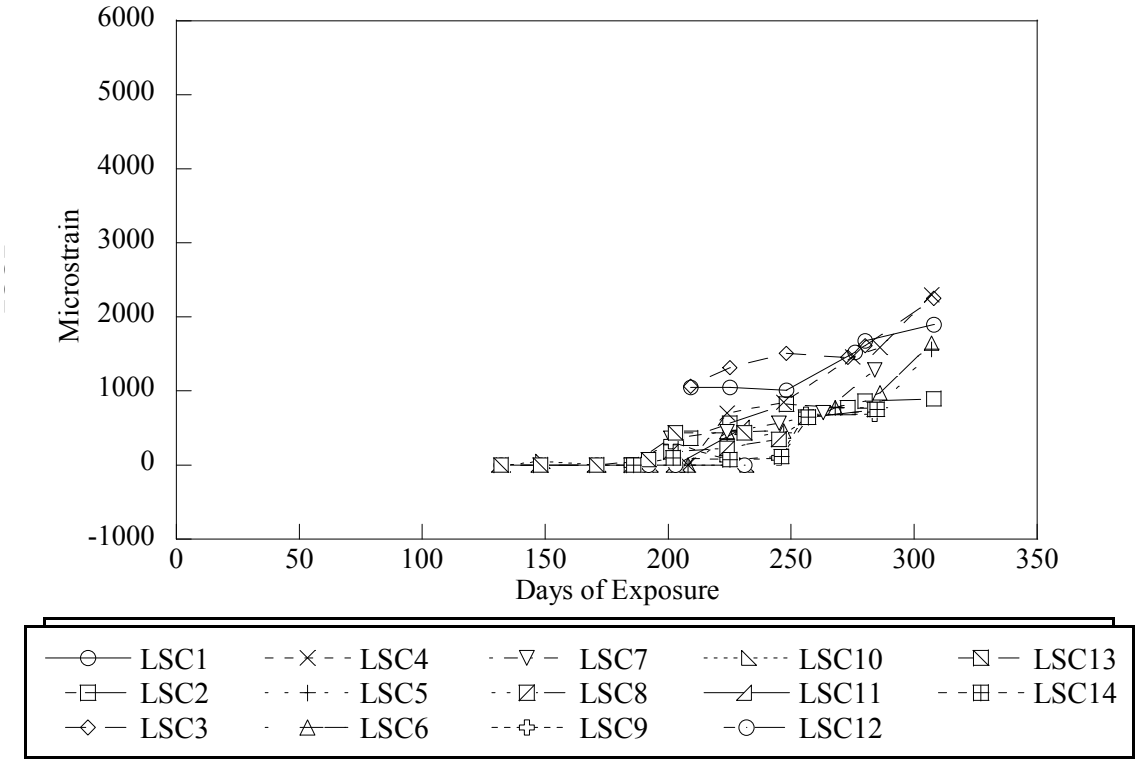

Figure 3-14 Transverse Strains on the Short Side by Summing Crack Widths

3.3.5. Comparison of Measurements

A comparison of each measurement method was completed for the LSC specimens. The comparison allows for a strain distribution to be identified from the surface of the concrete to a 3 in (76.2 mm) depth; the DEMECs are on the surface, one KM gage was placed at 1 in (25.4 mm) inside the surface, the hoop reinforcement has a strain gage attached 2 in (50.8 mm) from the surface, and the other KM gage is embedded at 1 in (25.4 mm) below the hoop. As shown in Figure 2-13, the strain gage on the long side of the column is positioned higher up than the KM gages and the DEMEC averaging. This provides for slightly higher strains. Figure 3-15 shows the location of the 5 different gages for the short side of the columns.

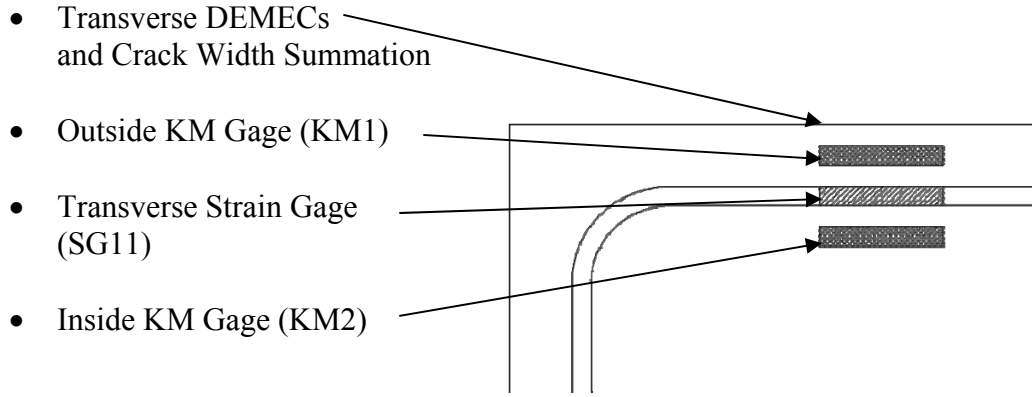

Figure 3-15 Strain Distribution from Surface

Figure 3-16 shows the results from LSC1 through LSC4. In each LSC specimen the surface measurement by the DEMEC points shows the highest strains except for LSC4 where the outer KM gage is slightly higher. The outer KM gage is also the second highest strain in each column except for column 2 where the inside KM gage is slightly higher. The inside KM gage measurement is higher than the strain gage on the hoop for all columns and as expected, the crack width summation method has the smallest strain

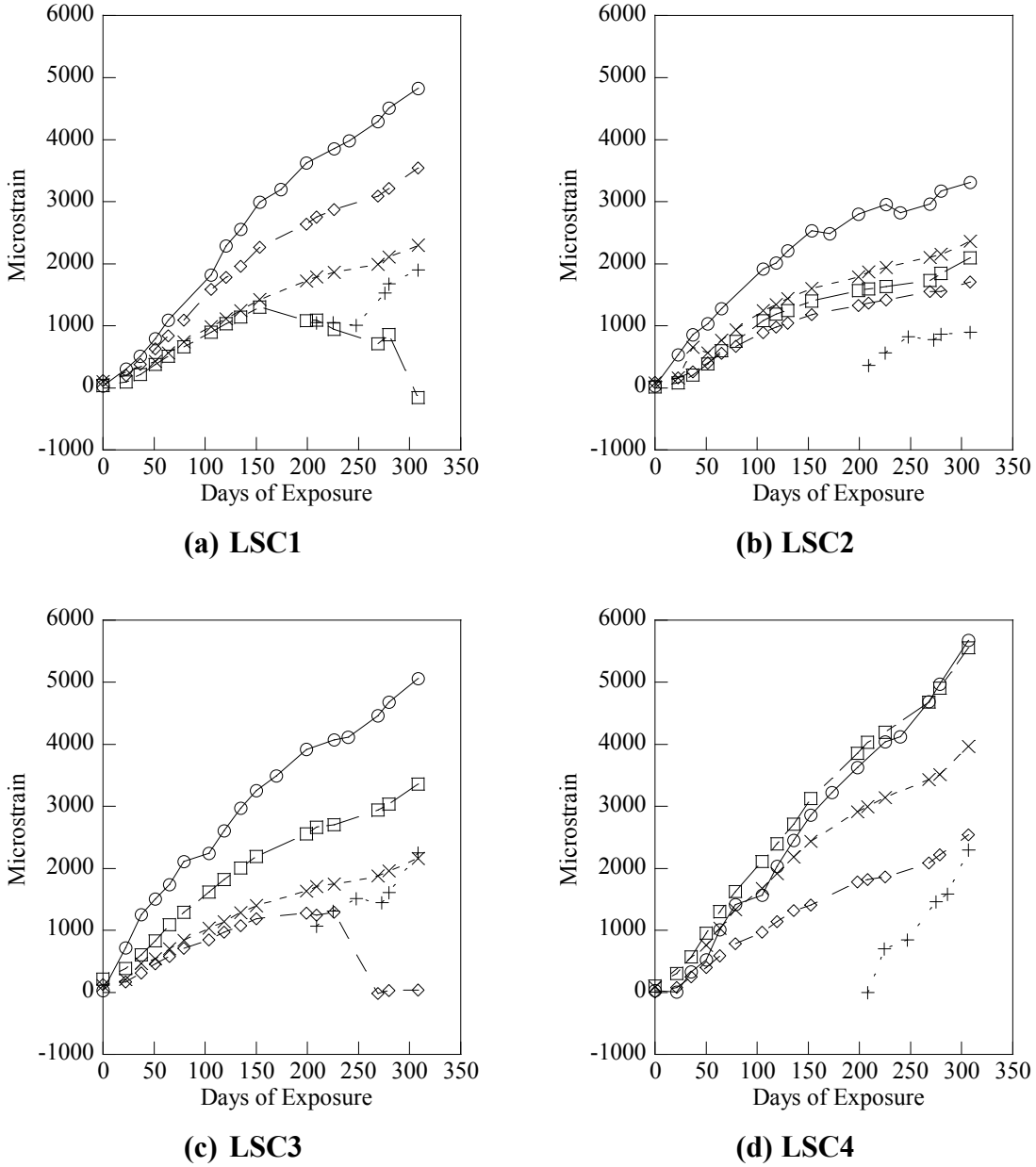

Figure 3-16 Comparison of Transverse Strain Measurements

3.4. Summary

The specimens that have been exposed for the longest duration have been stored at the Riverside campus and have exhibited significant expansion in a relatively short duration. Several observations on the behavior of ASR/DEF expansion can be made.

- Significant expansion and cracking in the tension field has developed in the specimens
- Higher strains were measured at the surface when compared to internal strains
- The strain in the KM gages positioned between the hoops is larger than the strain in the SG on the hoops.
- The short side of the LSC specimens is expanding faster than the long side, especially below mid height.

4. ANALYSIS OF COLUMN SPLICE REGION

4.1. Introduction

Columns are vertical prismatic members designed to carry compressive axial loads, shear forces and bending moments. Events such as hurricanes can provide large flexural and shear demands to the columns due to overturned or sidesway failure mechanisms. Because past research has shown that ASR may not significantly affect the compression strength, the LSC specimens are tested to evaluate the flexural capacity of the splice region, or more significantly, the tensile capacity of the spliced longitudinal reinforced section. If ASR/DEF deteriorate the bond, the capacity of the column can be decreased. Alternatively, if the bond is not affected by ASR/DEF, the capacity of the column may not be reduced.

In this work, the strength of the splice is calculated using flexure theory for reinforced concrete sections. A factor for the development length calculations is added to the theory to account for the loss of bond strength due to premature concrete deterioration. The analytical program also focuses on the test setup that simulates an overturning moment near the base of a column. Though a lateral force distribution is triangular for cantilevered columns, a four-point test provides a conservative constant moment across the splice length. Additionally, a three-point test was designed to create a high demand on the undeveloped region of the splice to promote bond failure.

4.2. Analytical Program - Capacity Analysis Using Flexure Theory

4.2.1. Objectives

The objectives of the analytical program are to:

- Develop an analytical model that accounts for bond and its affect on the structural capacity of a column lap splice region;

- Calibrate the analytical model with test results from the four-point and three-point tests of the undamaged control specimens; and
- Identify the possible severity of bond degradation due to ASR/DEF and develop reduction factors for the required splice length based on the severity of ASR/DEF deterioration.

4.2.2. Modeling Assumptions

The following assumptions were used in the analytical methodology:

- Plane sections remain plane (compatibility),
- The reinforcing steel is perfectly bonded with the surrounding concrete, which means the strain in the steel is equal to the strain in the surrounding concrete,
- Both concrete and steel were assumed to behave linearly in the elastic region according to Hooke's Law,
- Bars develop strength proportional to the ratio of the embedment length provided to the development length required for the reinforcing steel,
- The concrete contributes no strength in tension after it has cracked, which places additional load on the reinforcement,
- Concrete crushes at a compressive strain of 0.003 as specified by AASHTO LRFD (2004), and
- The stress-strain relationship of the reinforcing steel is modeled as elastic-perfectly plastic.

4.2.3. Splice Capacity Model

A capacity model for the splice region of a RC column was developed using the basic laws of mechanics with the assumptions described in Section 4.2.2: (1) Compatibility - plane sections remain plane and the strain in the bars is equal to the surrounding concrete, (2) Constitutive - Hooke's Law governs the relationship between stress and

strain up to yielding, and (3) Equilibrium. Figure 4-1 shows the theory for the three different limit states of structural flexural capacity; (1) at first crack in the concrete, (2) when the tensile reinforcing steel first yields, and (3) ultimate caused by crushing of the concrete in compression.

The flexural capacity calculations in the splice region are dependent on the area of the tensile reinforcing steel at a particular section of the LSC, which is dependent on whether the bar is properly embedded in the concrete (development length, l_d). The development length is defined as the shortest length of bar in which the bar stress can increase from 0 to the yield strength, f_y (MacGregor 1997). Therefore, l_d is dependent on the location of the bar ends, which will be referred to as geometrical boundaries. Geometrical boundaries consist of reinforcement discontinuities (bar ends) and mid-sections of the reinforcement where the development length criterion switches direction. The effective area of steel is calculated relative to the geometric boundaries and is a critical parameter of the strength associated with the concrete in the analytical model proposed in this thesis. Figure 4-2 shows the additive nature of the effective area of steel in the splice region and Figure 4-3 shows the effective area of steel available at each cross section presented as a piecewise linear curve with nodes at the critical cross sections where a geometrical boundary occurs. The geometrical boundaries are designated by sections A through F, which are mirrored to both sides of the column (Table 4-1). The effective area of steel is a critical parameter of the strength associated with the concrete in the analytical model proposed in this thesis.

Table 4-1 Geometric Boundaries of Tensile Reinforcement

Cross Section	Geometric Boundary
A	Reinforcing steel begins with hooked end
B	Hooks on the splice bars fully develop
C	Mid-section of the straight bars
D	Splice end (one splice bar begins while the other is continuous)
E	One development length from the end of the spliced bar
F	Mid-section of the LSC

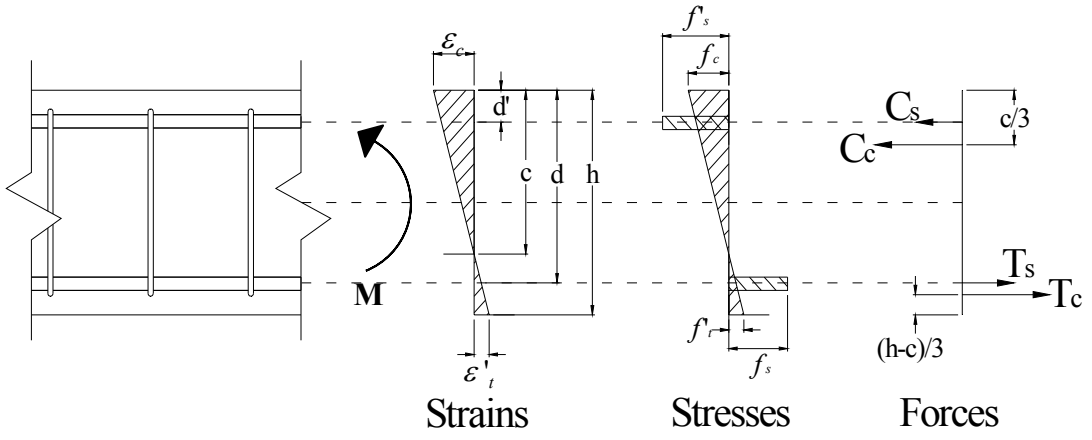

(a) Cracking of the Concrete in Tension

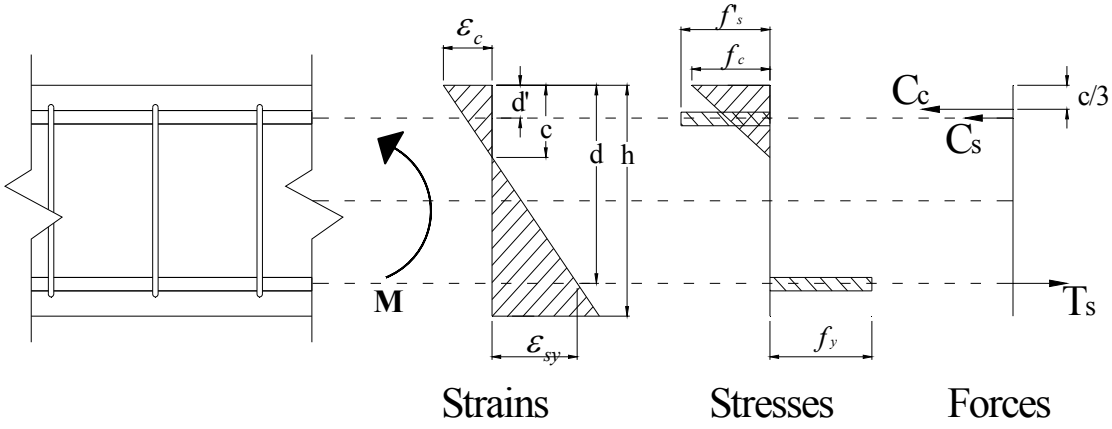

(b) Yielding of the Reinforcing Steel

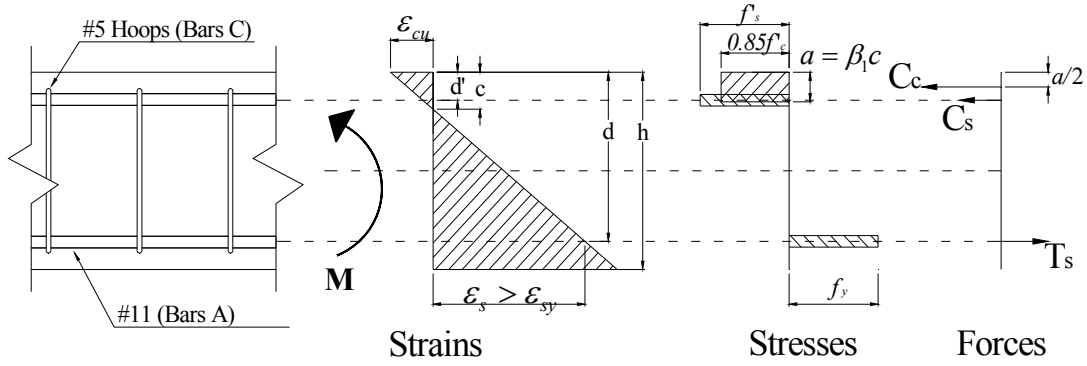

(c) Ultimate Crushing of the Concrete

Figure 4-1 Structural Flexural Limit States

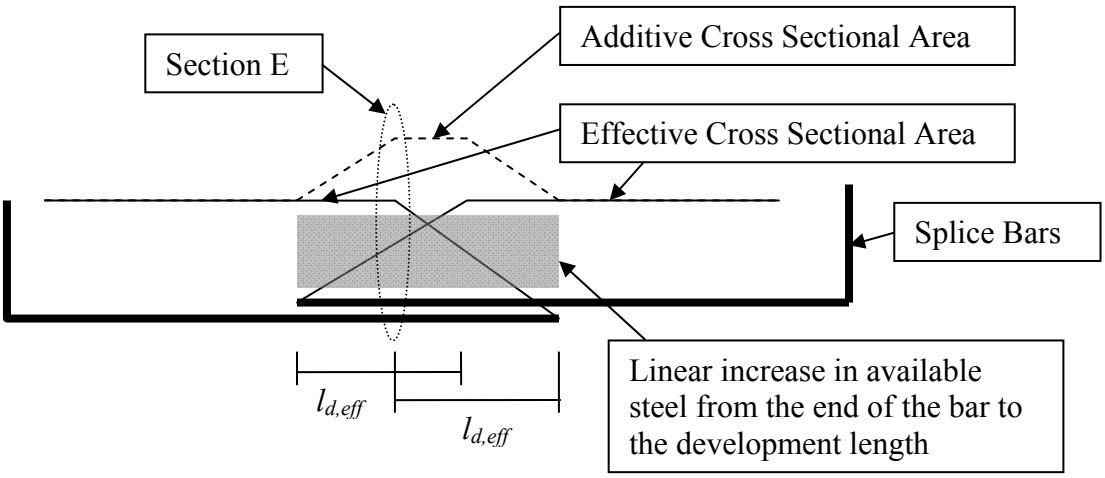

Figure 4-2 Linear Addition of Undeveloped Steel

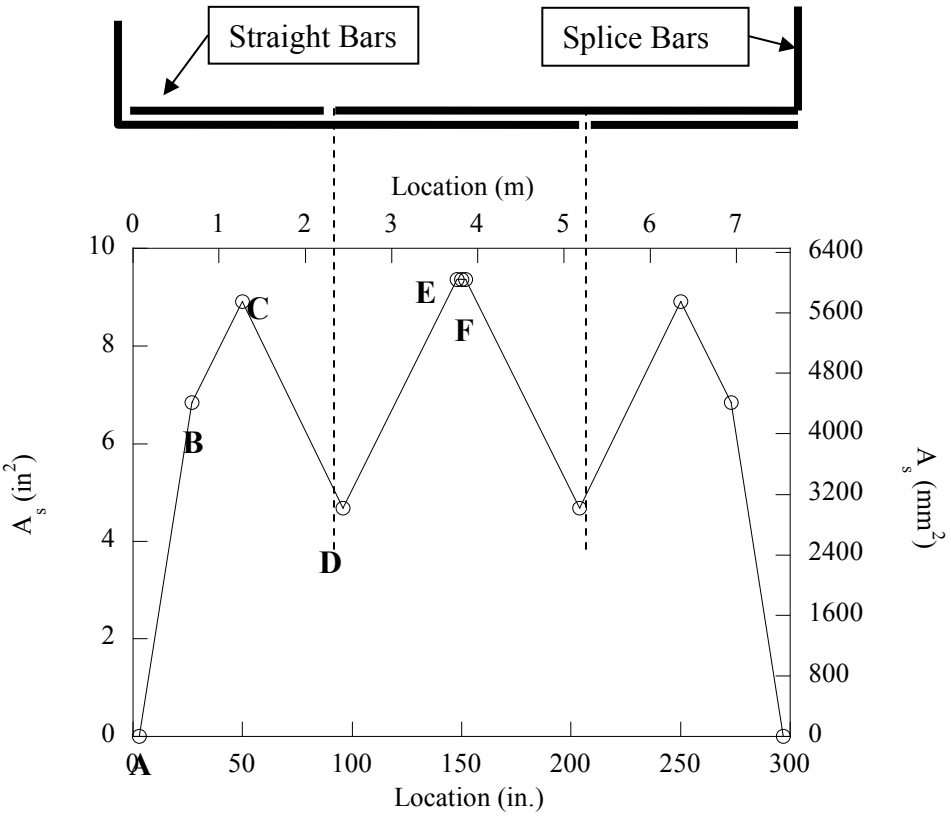

Figure 4-3 Area of Tension Steel in the LSC Specimens Based on Reinforcement Layout

Section A represents the location where the 90° hook on the splice bars begins near the end of the beam. Eq. (4.1) shows the area of reinforcing steel used for the capacity calculations. This identifies the beginning of the load bearing portion of the column and all equations are calculated using inches.

$$A_{s,A} = 0 \tag{4.1}$$

As the hooked end of the splice and straight bars develop, the amount of available steel increases. The area of available steel at section B (when the hooked splice bar is fully developed), $A_{s,B}$, can be determined as follows:

$$A_{s,B} = 3A_{bar} + \frac{l_{hb}}{l_{d,eff}}\left(3A_{bar}\right) \tag{4.2}$$

where A_{bar} is the area of one bar (note that there are three bars in tension at this location), $l_{d,eff}$ is the effective development length derived from multiplying Eq. (1.5) by an effective development length factor to be determined experimentally by load testing of the deteriorated LSC specimens later in the research. For this thesis, the factor is taken as 1.0 because the control specimens used to validate this model exhibited no deterioration. According to the AASHTO LRFD Design Specifications (2004), the development length for the deformed hook, l_{hb}, (identifies location of point B) is defined as follows:

$$l_{hb} = \frac{38.0 d_b}{\sqrt{f'_c}} \tag{4.3}$$

where f'_c is the compressive concrete strength in ksi, and d_b is the reinforcement diameter in inches.

The next geometrical boundary occurs at the mid-section of the straight bar. At this point, section C, the straight bar is not fully developed, but it has reached the most developed section of the bar and the effective area can be determined as follows:

$$A_{s,C} = 3A_{bar} + \frac{47}{l_{d,eff}}\left(3A_{bar}\right) \tag{4.4}$$

The next point, section D, is located at the beginning of the splice. The straight bars end at this location and no longer contribute any area (or strength), which leaves the section with only one set of bars, the splice bars. The amount of equivalent steel area can be determined as follows:

$$A_{s,D} = 3A_{bar} \tag{4.5}$$

The location of Section E is defined by the effective development length, $l_{d,eff}$ of the straight end of the spliced bar. From the splice end, the effective area in one splice bar increases while the other will decrease because of the straight end on the other end of the splice.

The capacity at section E is based on the full development of one set of splice bars and the partial development of the opposite set of slice bars and the equivalent area can be determined as follows:

$$A_{s,E} = 3A_{bar} + \frac{108 - l_{d,eff}}{l_{d,eff}}(3A_{bar}) \tag{4.6}$$

where $A_{s,E}$ cannot exceed a value of $6A_{bar}$, which is possible for $l_{d,eff}$ < 54 in (1.47 m). This is also true for $A_{s,F}$.

Figure 4-2 shows the linear increase in the effective area of the steel and the additive nature of the splice, which provides additional strength (Ferguson 1966). As shown in Figure 4-3 and Figure 4-2, the $l_{d,eff}$ is significantly less than the provided splice length. In this case, there is significant flexural over-strength throughout the splice region (i.e. conservative design). However, as the concrete deteriorates, $l_{d,eff}$ will potentially increase (determined by testing at a later date), and as such, reduces the over-strength of the splice region.

From section E to the center of the splice, the effective area is the same. This is also due to the linear addition of the total undeveloped splice steel. Rearranging Eq. (4.6), Eq. (4.7) shows the summation of two sections of undeveloped splice steel at section F. This is based upon the assumption that the reinforcement gains strength linearly from the end of the reinforcement to the developed length as discussed in Section 4.2.2. This can be can be determined as follows:

$$A_{s,F} = 2 * \frac{54}{l_{d,eff}} (3A_{bar}) \qquad \left\{ \begin{array}{l} *\text{where } l_{d,eff} \leq 54, \\ \text{since the bar is not developed} \end{array} \right\} \tag{4.7}$$

Additionally, Figure 4-4 shows that as $l_{d,eff}$ approaches the splice length of 108 in (2.74 m), the additive cross-sectional area is constant across the entire length of the splice with an effective area for 3 bars of reinforcement ($3A_{bar}$). When $l_{d,eff}$ is longer than the splice length, bond failure can occur, resulting in a brittle failure mechanism.

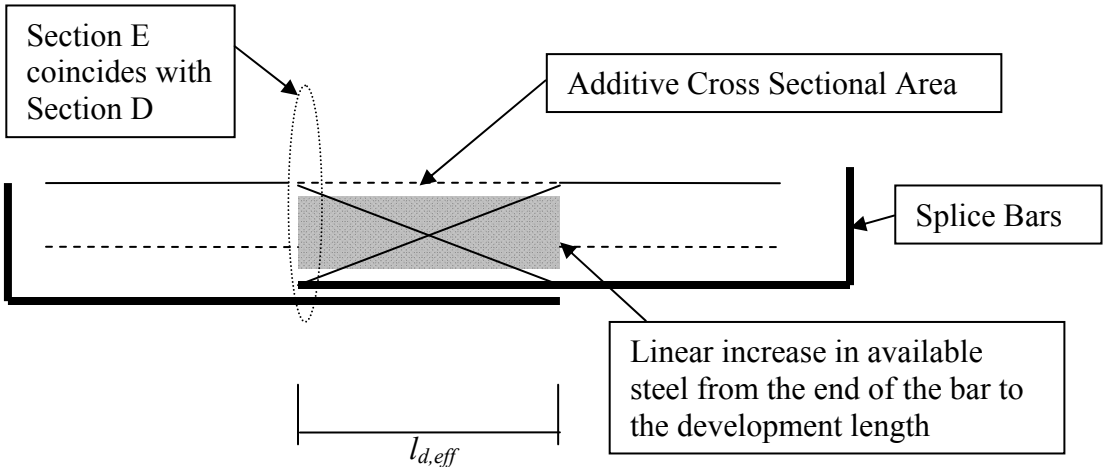

Figure 4-4 Linear Addition of Undeveloped Steel When $l_{d,eff}$ Equals the Splice Length

4.2.4. Iterative Analytical Model for Flexural Capacity

With the effective cross-sectional area of the longitudinal reinforcement established at each section along the LSC specimen, the flexural capacity is calculated using an iterative approach based on flexure theory. Due to the axial load from the PT strands, the neutral axis of the column shifts from the center, creating a larger compression region. Figure 4-1 shows the strain diagram at each stage of loading; cracking of the concrete in tension, yielding of the reinforcement, and ultimate failure with crushing of the concrete.

At first cracking, the strain and stress diagrams are calculated across the entire cross section because the entire section contributes structurally to resisting the load. The limiting criterion is based upon the ability of the concrete to resist tensile loads. The tensile stress in concrete is based upon the tensile strength, f'_t, which is calculated from the compressive strength, f'_c (AASHTO LRFD 2004) as follows:

$$f'_t = 0.24\sqrt{f'_c} \tag{4.8}$$

where f'_t and f'_c (28-day cylinder strength) are in ksi. The critical value of each stage of failure is also shown in Figure 4-1. The concrete cracks at 237μst which is based on the tensile strength of the concrete (MacGregor 1997) as follows:

$$\varepsilon'_t = 1.8 * \frac{f'_t}{E_c} \tag{4.9}$$

where E_c is the modulus of concrete calculated by:

$$E_c = 57000\sqrt{f'_c} \tag{4.10}$$

where E_c and f'_c are in psi.

As the section continues to bend, Figure 4-1 depicts the upward movement of the neutral axis from approximately 4 in (102 mm) below the centroid at first cracking to approximately 6 in (152 mm) above the centroid at ultimate failure. This is based on the assumption that plane sections remain plane and satisfying equilibrium through an iterative approach.

At first yielding of the tensile steel (see Figure 4-1b), a tensile strain of 2069μSt is calculated according to Hooke's law:

$$\varepsilon_{sy} = \frac{f_y}{E_s} \tag{4.11}$$

where f_y is the yield strength of the steel and E_s is the modulus of the steel taken as 60 ksi (414 MPa) and 29,000 ksi (200 GPa) respectively.

Finally, at ultimate capacity, the steel continues to yield and the concrete begins to crush in compression. Using a conservative concrete crushing strain, ε_{cu}, of -3000μSt, (from AASHTO LRFD (2004) and ACI 318-08), it can be shown for the LSC specimen that the strain diagram allows the steel to deform perfectly plastic to about 4 times the yield strain, resulting in a fairly ductile section.

In addition to the critical values mentioned (ε'_t, f_y, and ε_{cu}), equilibrium must be satisfied for the cross section. The iteration revolved around an assumed depth for the neutral axis. By moving the neutral axis towards the compressive region, the total axial force on the section would decrease and vice versa with a move towards the tension region of the section. Because the depth and strain of both the critical value and the neutral axis are now known, the strain between these points can be assumed to be linear. From this strain distribution across the section, the stress in each component of the cross section can be calculated using Hooke's Law. With a stress identified for each component of the section, a force can be calculated based on the stress distribution. For the reinforcement steel, the stress distribution is assumed to be constant and therefore results in a force centered on the reinforcement depths, both top and bottom. The concrete, however, forms different stress distributions across the depth of the section as the load increases. Figure 4-1 shows the progression of the calculations from strain to stress to force for all three stages of loading. At cracking, the concrete has a triangular distribution in both the compression and tension regions, and after the concrete has cracked, Figure 4-1b shows that only the compression region remains. After the reinforcement yields, the compressive stress in the concrete begins to take on a parabolic shape that can be represented as a rectangular block (Whitney's stress block) in Figure 4-1c. With the stress distributions identified, forces can be generated for the cross section. These forces can then be used used to calculate the total axial force, P_{axial}, on

the column by summing the forces and to calculate the moment applied to the section by taking moments of the forces about the centroid.

P_{axial} is equal to the load applied by the PT strands, which is 580.8 kips (2.58 MN) for the LSC specimen. If the calculated value for P_{axial} is higher than 580.8 kips (2.58 MN), then the neutral axis is raised and vice versa. This is done until the calculated value for P_{axial} is equal to 580.8 kips (2.58 MN), then the moment is taken to find the moment capacity of the section for each different stage of loading.

Table 4-2 shows the data from an example calculation for identifying the moment capacity of the splice end, which has an effective area of reinforcement of 4.68 in^2 (3019 mm^2) or three #11 bars. The value c is the distance from the top of the column to the neutral axis and is the value of iteration. The values P_{axial} and M_{cr} are the axial load in the column taken as 580.8 kips (2.58 MN) and the moment capacity at cracking taken as 5783.4 kip-in (94.1 MN-m), respectively.

Table 4-2 Sample Values from Iterative Calculations Based on Equilibrium at Cracking

Variable	Units	Values
A_s	in^2	4.68
c	in	15.88
ε_c	$^{in}/_{in}$	0.000463
f_c	ksi	1.69
C_c	$kips$	643.72
T_c	$kips$	93.63
ε_s	$^{in}/_{in}$	0.000140
f_s	ksi	4.05
T_s	$kips$	18.99
$\varepsilon_{s'}$	$^{in}/_{in}$	0.000366
$f_{s'}$	ksi	10.6
C_s	$kips$	49.7

All calculations used inches for length, kips for force, and ksi for stress. From an initial estimate for c, the compressive strain, ε_c was calculated for the outermost fiber of the compression region as follows:

$$\varepsilon_c = \left(\frac{c}{h-c}\right)\varepsilon'_t \tag{4.12}$$

where h is the height of the cross section and ε'_t is the tensile strain of concrete at first crack. The compressive stress of the concrete, f_c, at the same location was calculated using Hooke's Law. Using the compression and tensile stresses at the outermost fibers, the compression and tensile forces, C_c and T_c respectively, can be calculated as follows:

$$C_c = \frac{f_c c b}{2} \tag{4.13}$$

$$T_c = f'_t b\left(\frac{h-c}{2}\right) \tag{4.14}$$

where b is the width of the section and f'_t is the tensile strength of concrete.

In addition to the concrete, the reinforcing steel also contributes strength to the section. Because $f_s \le f_y$, the strain in the tension steel, ε_s, is calculated as follows:

$$\varepsilon_s = \left(\frac{d-c}{h-c}\right)\varepsilon'_t \tag{4.15}$$

where d is the depth of the tension steel from the top of the section calculated as follows:

$$d = h - l_c - d_{b,hoop} - \frac{d_{b,long}}{2} \tag{4.16}$$

where l_c is the concrete cover, $d_{b,hoop}$ is the diameter of the hoops, and $d_{b,long}$ is the diameter of the longitudinal steel. The strain is used to calculate the stress and subsequently the force in the tension steel as follows:

$$f_s = E_s \varepsilon_s \tag{4.17}$$

$$T_s = f_s A_s \tag{4.18}$$

where f_s is the stress in the tension steel, E_s is the modulus of the steel, T_s is the force in the steel, and A_s is the area of the tension steel calculated in Section 4.2.3. Similarly, the strain, stress, and force in the compression steel, $\varepsilon_{s'}$, $f_{s'}$, and C_s respectively were calculated as follows:

$$\varepsilon_{s'} = \left(\frac{c - d'}{h - c} \right) \varepsilon'_t \tag{4.19}$$

$$f_{s'} = E_s \varepsilon_{s'} \tag{4.20}$$

$$C_s = f_{s'} A_s \tag{4.21}$$

where d' is the depth of the compression steel from the top of the section as calculated by:

$$d' = l_c + d_{b,hoop} + \frac{d_{b,long}}{2} \tag{4.22}$$

Using the forces calculated in Eqs. (4.13), (4.14), (4.18), and (4.21), the axial force, P_{axial}, in the section can be calculated as follows:

$$P_{axial} = C_c + C_s - T_c - T_s \tag{4.23}$$

By equilibrium, the summation of the forces will need to be equal to the 580.8 kips (2.58 MN) of axial compression exerted by the PT strands. If this is not the case, the neutral axis will be shifted until the equation is satisfied.

Once equilibrium has been satisfied for the section, the moment capacity of the section at first crack, M_{cr}, of the concrete is calculated as follows:

$$M_{cr} = C_c \left(\frac{h}{2} - \frac{c}{3} \right) + C_s \left(\frac{h}{2} - d' \right) + T_c \left(\frac{h}{2} - \frac{h - c}{3} \right) + T_s \left(\frac{h}{2} - (h - d) \right) \tag{4.24}$$

where the variables have been defined earlier. The calculations above are visually represented in Figure 4-1a.

When the concrete cracks, the stresses are redistributed in the section because the concrete no longer contributes any tensile strength. This leads to new equations for the strain distribution because the limiting value of ε'_t is replaced by the strain in the tension steel ε_{sy}. The strain in the outermost fiber of the concrete in compression ε_c is calculated as follows:

$$\varepsilon_c = c\left(\frac{\varepsilon_{sy}}{d-c}\right) \tag{4.25}$$

This also results in a new value for the strain in the compression steel as follows:

$$\varepsilon_{s'} = \left(\frac{c-d'}{d-c}\right)\varepsilon_{sy} \tag{4.26}$$

which leads to new values for f_c and $f_{s'}$ as calculated by Hooke's Law and Eq (4.20) respectively. In conjunction with $f_s = f_y$ and $T_c = 0$, the forces calculated in Eqs. (4.13), (4.18), and (4.21) are used to recalculate P_{axial} in Eq. (4.23). If P_{axial} is not equal to the axial force induced by the PT strands, the iterative process is repeated to find the new depth of the neutral axis, c. Finally, the moment capacity at yielding of the steel is calculated as $M_y = M_{cr}$ with T_c again equal to 0. The conditions and parameters for the structural capacity at yield are visually shown in Figure 4-1b.

Once the steel yields, the stress, f_s, in the tension steel is always taken as f_y as the load increases. This allows the steel to yield uninhibited, which makes the crushing of the concrete, the limiting value. For this scenario, the strain in the compression concrete, ε_c, is equal to ε_{cu}, which is taken as -0.003.

At this phase of the loading, the stress curve in the concrete takes on the shape of a parabola and is idealized as a rectangle with a depth of a from the top of the section and a stress, f_c, of 0.85 f'_c (Whitney's stress block). The depth a and f_c are calculated as follows:

$$a = \beta_1 c \tag{4.27}$$

$$f_c = 0.85 f'_c \tag{4.28}$$

where c is the depth of the neutral axis and Section 10.2.7 of ACI 308-05 shows β_1 is a factor taken as 0.8 for 5000 psi (34.5 MPa) concrete. The equivalent force of the compression concrete is calculated as follows:

$$C_c = abf_c \tag{4.29}$$

In addition to the change in the stress distribution in the concrete, the strain of the tension and compression steel is recalculated as follows:

$$\varepsilon_{s'} = \left(\frac{c - d'}{c} \right) \varepsilon_{cu} \tag{4.30}$$

$$\varepsilon_s = \left(\frac{d - c}{c} \right) \varepsilon_{cu} \tag{4.31}$$

which changes the values of f_s and $f_{s'}$ in Eqs. (4.17) and (4.20), respectively. The value of C_c in Eq. (4.29) and the recomputed forces T_s and C_s in Eqs. (4.18) and (4.21) respectively are combined to recalculate P_{axial} in Eq. (4.23) where T_c is taken as 0. The iterative process is completed again to reestablish the correct axial force in the section and then the moment capacity can be calculated as follows:

$$M_u = C_c\left(\frac{h}{2}-\frac{a}{2}\right)+C_s\left(\frac{h}{2}-d'\right)+T_s\left(\frac{h}{2}-(h-d)\right) \tag{4.32}$$

The conditions and parameters of the ultimate capacity of the section are visually represented in Figure 4-1c.

This section provided calculation procedures for determining the moment capacities M_{cr}, M_y, and M_u at cracking of the concrete, yielding of the steel, and crushing of the concrete, respectively. This was completed at each section by first determining the area of steel, then using an iterative process to apply compatibility and equilibrium to a section subject to an axial load.

4.2.5. Strain Gage Predictions in Longitudinal Steel

Eight SGs were positioned on the longitudinal tension reinforcement in the splice region, 4 on a splice bar in the middle of the section and 4 on a splice bar in the corner of the tension region. These strain gages were spaced at 24 in (610 mm) intervals beginning 18 in (457 mm) from the splice end. Figure 4-5 shows the locations of SG1 through SG4. From the analytical model, the strains in the center reinforcing bar are equal to those in the corner as it is assumed that plane sections remain plane. For simplicity, only SG1 through SG4 will be referenced for the remainder of this section.

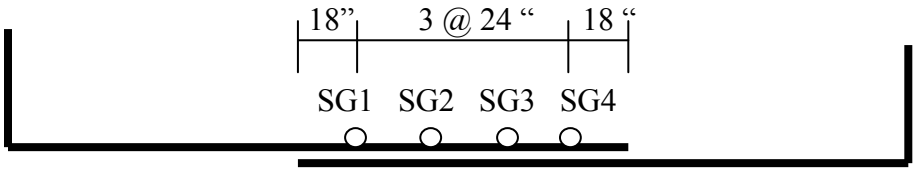

Figure 4-5 SG Locations on Center Bar

Using the capacity analysis described in Section 4.2.4, the section strength at SG1 and SG4 as well as SG2 and SG3 are the same due to symmetry. However, the values measured by the SGs should be different. For example, SG1 is on the portion of the bar that is fully developed for small values of $l_{d,eff}$ and SG4 is in the undeveloped portion of the bar. This results in larger strains in SG1 because it can develop and potentially yield at that location. SG4 will slip before it yields and therefore will exhibit lower values. To capture this behavior, a factor to compensate for the equivalent amount of steel that the SG is attached to was added to the strain capacity calculated for the sections as follows:

$$\text{SG1 Factor} = \frac{A_{s,SG1}}{A_{s,SG1} + A_{s,SG4}} = \frac{\frac{l_{splice} - 18}{l_{d,eff}}(A_{bar})}{\left(\frac{l_{splice} - 18}{l_{d,eff}} + \frac{18}{l_{d,eff}}\right)A_{bar}} = \frac{l_{splice} - 18}{l_{splice}} = 0.83 \qquad (4.33)$$

where l_{splice} is the length of the splice taken as 108 in (2.74 m) from geometry and $A_{s,SG1}$ and $A_{s,SG4}$ represent the effective area of the bar that the SG is attached. Basically, a ratio is calculated based on the area of the instrumented bar to the total area of both bars in the splice. All variables are calculated in inches.

The remaining SG factors are calculated using the same methodology:

$$\text{SG2 Factor} = \frac{A_{s,SG2}}{A_{s,SG2} + A_{s,SG3}} = \frac{\frac{l_{splice} - 42}{l_{d,eff}}(A_{bar})}{\left(\frac{l_{splice} - 42}{l_{d,eff}} + \frac{42}{l_{d,eff}}\right)A_{bar}} = \frac{l_{splice} - 42}{l_{splice}} = 0.61 \qquad (4.34)$$

$$\text{SG3 Factor} = \frac{A_{s,SG3}}{A_{s,SG2} + A_{s,SG3}} = \frac{\frac{42}{l_{d,eff}}(A_{bar})}{\left(\frac{l_{splice} - 42}{l_{d,eff}} + \frac{42}{l_{d,eff}}\right)A_{bar}} = \frac{42}{l_{splice}} = 0.39 \tag{4.35}$$

$$\text{SG4 Factor} = \frac{A_{s,SG4}}{A_{s,SG1} + A_{s,SG4}} = \frac{\frac{18}{l_{d,eff}}(A_{bar})}{\left(\frac{l_{splice} - 18}{l_{d,eff}} + \frac{18}{l_{d,eff}}\right)A_{bar}} = \frac{18}{l_{splice}} = 0.17 \tag{4.36}$$

where 42 in (1.07 m) and 18 in (457 mm) are the distances from the end of the splice to the symmetric section of SG2/SG3 and SG1/SG4 respectively.

The factors are multiplied by the calculated strain in the section using the iterative method described in Section 4.2.4 as follows:

$$\varepsilon_{s,gage} = \text{SG Factor} \times \varepsilon_s \tag{4.37}$$

where ε_s is the strain in the tension steel as calculated in Eqs. (4.15), (4.31), and $\varepsilon_s = \varepsilon_{sy}$ at the respective limit states. Figure 4-6 shows the analytical moment capacity versus strain for the bar instrumented with the SGs using the appropriate SG factors. Note that the reduction from the factor is only applied to the strain as the moment capacity of SG1/SG4 and SG2/SG3 are equal. Because the splice end has the least tensile area of steel, the lowest moment capacity of all the sections occurs at this point (splice end).

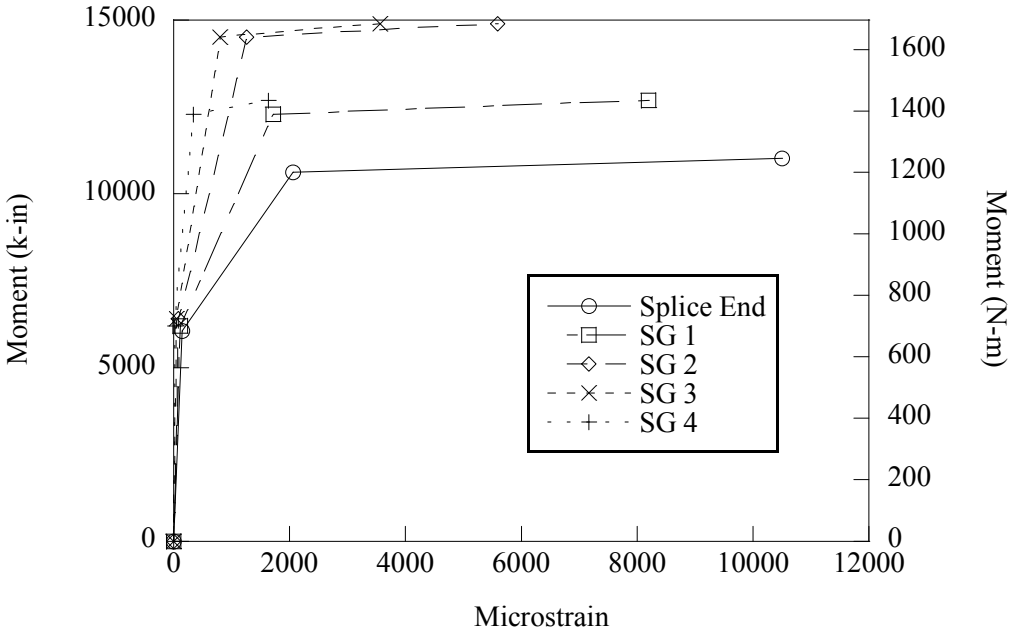

Figure 4-6 Analytical Moment Capacity and Strains of an SG Instrumented Bar

4.3. Analytical Predictions of Undamaged Control Specimens

The analysis in Section 4.2 yields moment-curvature curves for each section of the specimen. Figure 4-7 shows the moment-curvature at three locations in the LSC specimen; the splice end and the symmetric sections of SG1/SG4 and SG2/SG3.

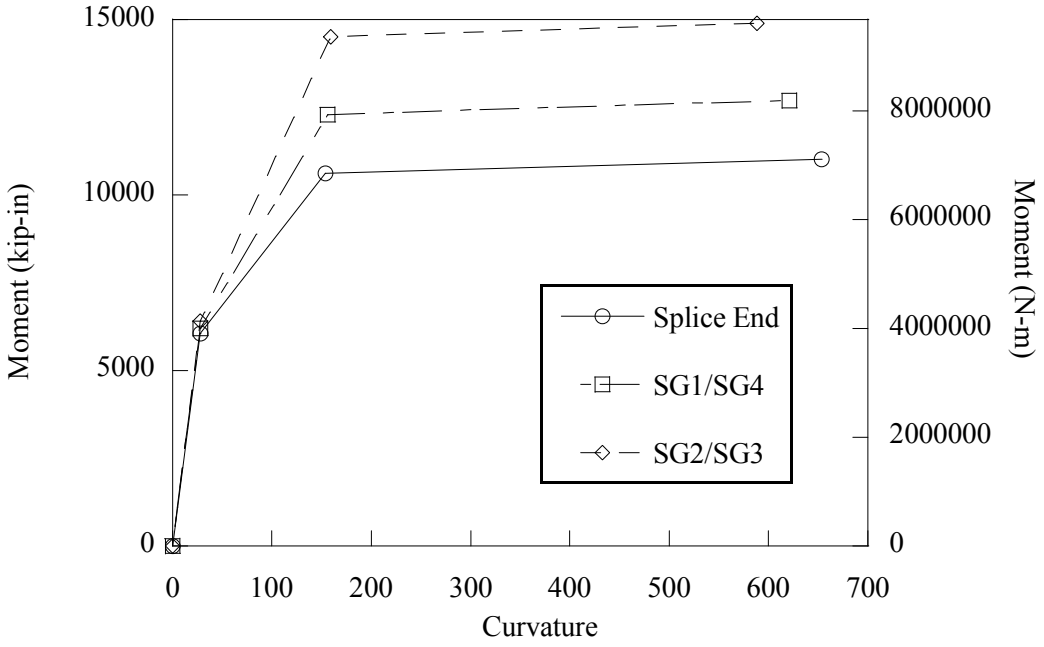

Figure 4-7 Moment-curvature of Splice and SG Locations

The sections at SG1/SG4 and SG2/SG3 have the same capacity, but the SG will read different strains as discussed in Section 4.2.5. Using this analysis, predictions are made on the performance of the LSC specimens during three- and four-point flexural load testing.

4.3.1. Four-point Test Predictions

Figure 4-8 shows that the four-point load test applies a constant moment and no shear stress across the splice length as discussed in Section 2.1. Pure flexural failure will occur where the demand exceeds the capacity at any section in the splice region. Figure 4-9 shows a figure that overlays the demand (Figure 4-8) and capacity. This figure shows that the demand and capacity are equal at the splice end located at 96 in (2.43 m)

from the end of the LSC specimens. Note the over-strength through the splice region due to conservative design of the splice (using an undeteriorated $l_{d,eff}$). Therefore, the largest cracks, yielding of the steel, and ultimately crushing of the concrete should occur at the location directly below the loading points.

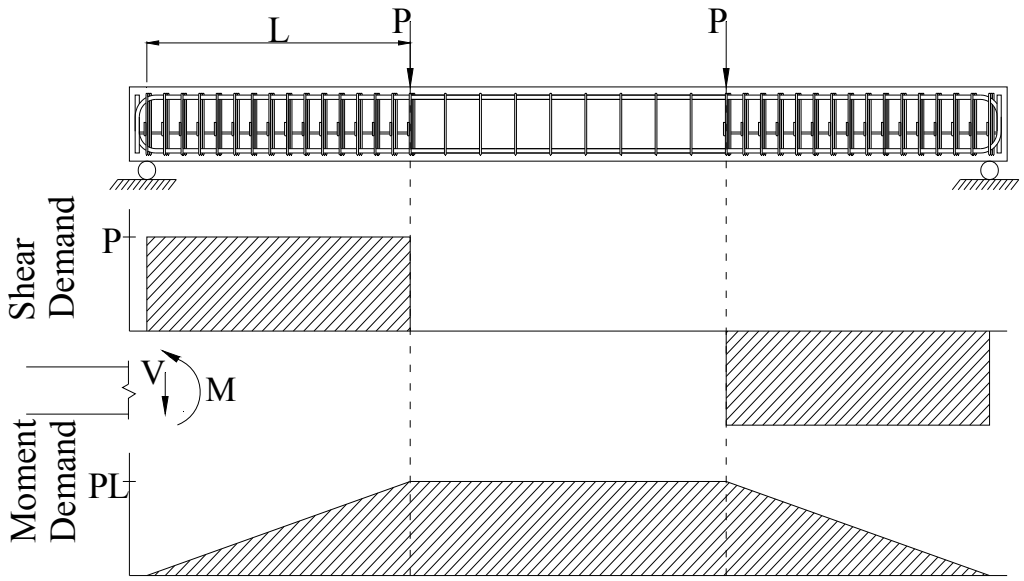

Figure 4-8 Four-point Load Test

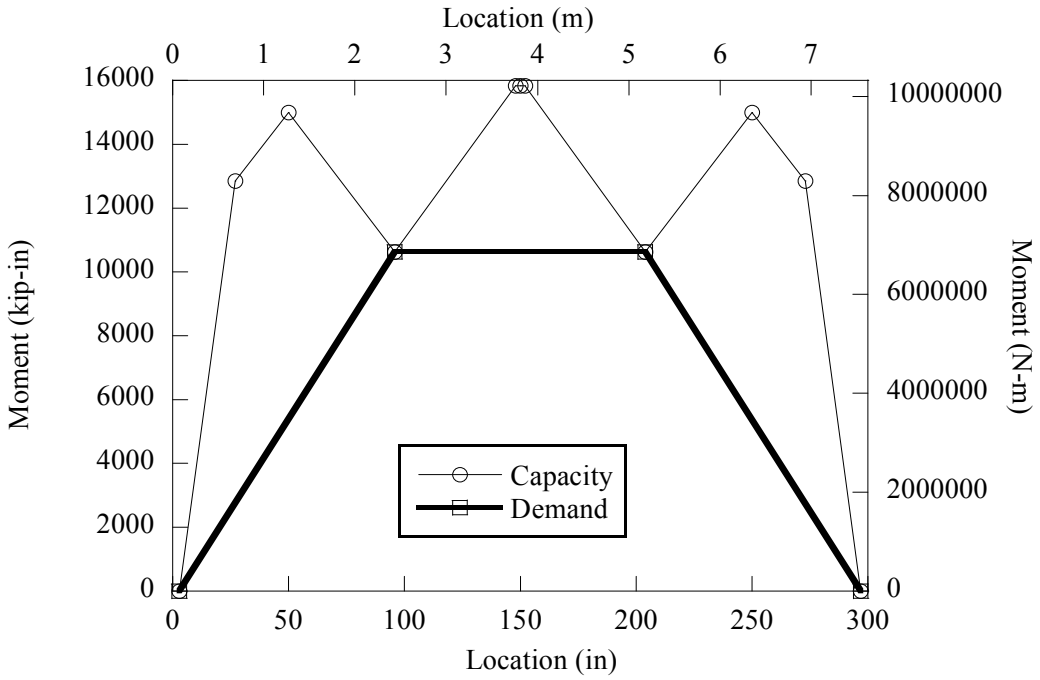

Figure 4-9 Four-point Load Test at Yield Capacity versus Demand

The strains on the tension steel in the splice are a function of the applied moment (or loading) similar to Figure 4-6. Note that once the bars in the splice end section have yielded, the strains throughout the splice should remain elastic and increase minimally as the bars begin to plastically deform at the splice end. Thus, the majority of the vertical deformations should be due to the plastic rotation at the splice ends. Figure 4-10 shows the load, *P*, versus the expected SG measurements. Notice that the strains are predicted to stop increasing once the splice end reaches yield and begins to behave plastically. The actuator load, *P*, can be calculated as follows:

$$P = \frac{M_{Load}}{L} = \frac{M_{Cap} - M_{Weight}}{L} \tag{4.38}$$

where L is the length from the end support to the actuator, M_{Cap} is the moment capacity at the respective limit state calculated in Section 4.2.4., and M_{Weight} is the moment demand from the self-weight of the specimen calculated as follows:

$$M_{weight} = w\frac{L_s}{2}\left((2L + L_{splice}) - L_s\right) \tag{4.39}$$

where L_s is the length from the end support to the desired cross section, L_{splice} is the length of the splice, and w is the weight per unit length of the LSC specimens.

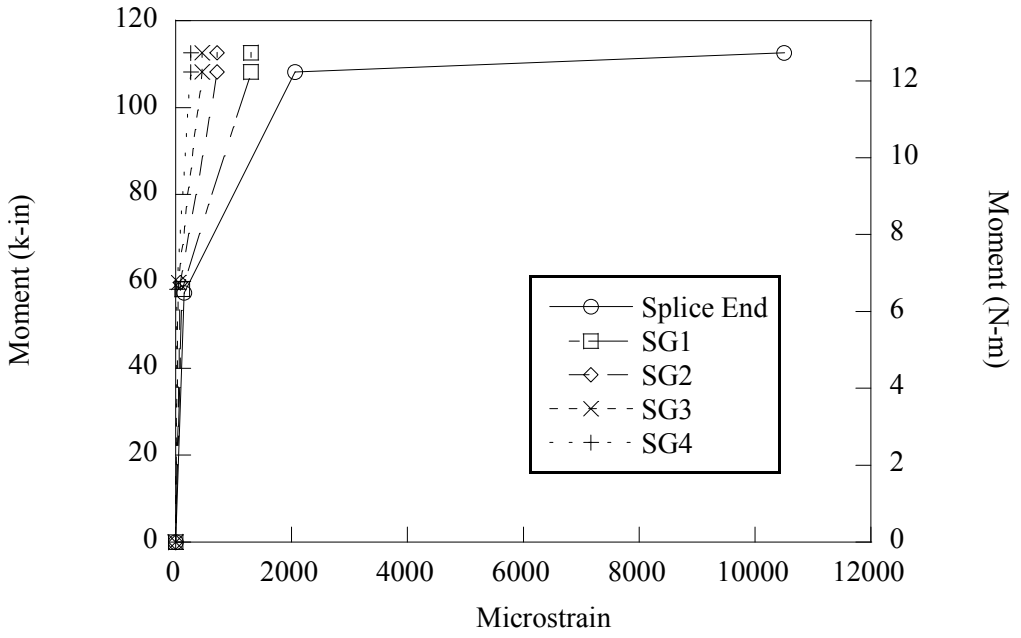

Figure 4-10 SG Measurement Predictions for the Four-point Test Setup

Additionally, deflections were calculated for the four-point load test. To calculate the deflection based on the load P, calculations were completed for each stage of the capacity curves; cracking of the concrete, yielding of the tension steel, and crushing of the concrete. The deflection at the cracking stage, Δ_c, can be calculated as follows:

$$\Delta_c = \frac{PL}{6E_c I_{xx}}\left(3\left(2L + L_{splice}\right)L_s - 3\left(L_s\right)^2 - L^2\right) \tag{4.40}$$

where E_c is the modulus of the concrete as calculated in Eq. (4.10) and I_{xx} is the moment of inertia of the cross section calculated as follows:

$$I_{xx} = I_{steel} + I_{concrete} \tag{4.41}$$

where I_{steel} and $I_{concrete}$ are the moment of inertia of the steel and concrete respectively and are calculated as follows:

$$I_{steel} = A_{s,eff}\left(y_{comp}\right)^2 + A_{s,eff}\left(y_{ten}\right)^2 \tag{4.42}$$

$$I_{concrete} = \frac{bh^3}{12} \tag{4.43}$$

where b is the width of the section, h is the height of the section, $A_{s,eff}$ is the effective area of steel in the cross section, y_{comp} is the distance from the neutral axis to the compression steel, and y_{ten} is the distance from the neutral axis to the tension steel. These can be calculated as follows:

$$A_{s,eff} = \left(A_s - 1\right)n = \left(A_s - 1\right)\frac{E_s}{E_c} \tag{4.44}$$

$$y_{comp} = c - d' \tag{4.45}$$

$$y_{ten} = d - c \tag{4.46}$$

where n is the ratio of the modulus of the steel and the modulus of the concrete.

After the concrete cracks, the moment of inertia shifts and can be calculated as follows:

$$I_e = \frac{bc^3}{3} + bc\left(\frac{h}{2} - c\right)^2 + I_{steel} \tag{4.47}$$

where I_e is the effective moment of inertia at yielding of the rebar and I_{steel} is recalculated using the new value of c at the yielding stage. The deflection at yielding of the steel, Δ_y, is calculated as:

$$\Delta_y = \frac{PL}{6E_c I_e}\left(3\left(2L + L_{splice}\right)L_s - 3\left(L_s\right)^2 - L^2\right) \tag{4.48}$$

Because the concrete is not contributing strength in the tension region of the section, the section loses stiffness and the specimen will deflect more as the load increases. The ultimate deflection at crushing of the concrete, Δ_u, is calculated considering the plastic rotation at the splice ends and the elastic deformations as follows:

$$\Delta_u = \phi_p \frac{d}{2} L + \Delta_y \tag{4.49}$$

$$\phi_p = \phi_u - \frac{M_u}{I_e E_c} = \frac{\varepsilon_{cu}}{c} - \frac{M_u}{I_e E_c} \tag{4.50}$$

where ϕ_p is the curvature of the section due to plastic deformation, ϕ_u is the curvature at crushing of the concrete, and M_u is defined in Eq. (4.32). Figure 4-11 shows the

deflection curve for the four-point test with nodes at the three limit state capacities of cracking, yield, and ultimate.

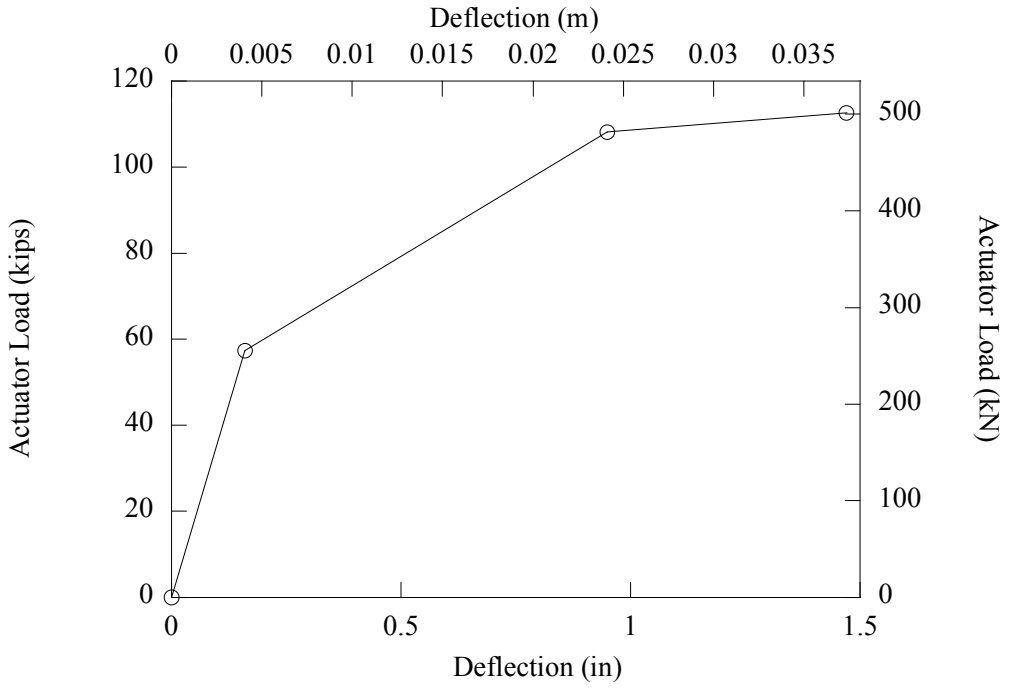

Figure 4-11 Actuator Load versus Splice End Deflection for the Four-point Actuator Load

4.3.2. Three-point Test Predictions

The three-point load test configuration differs from the four-point load test configuration in that it subjects the specimen to a constant shear across the splice length with varying moment loads. Figure 4-12 shows the shear force and moment demands on the LSC specimens with reference to the splice ends (hatched lines). The loads, *P*, are spaced 15 ft (4.57 m) apart and induce a triangular moment demand on the middle section of the specimen.

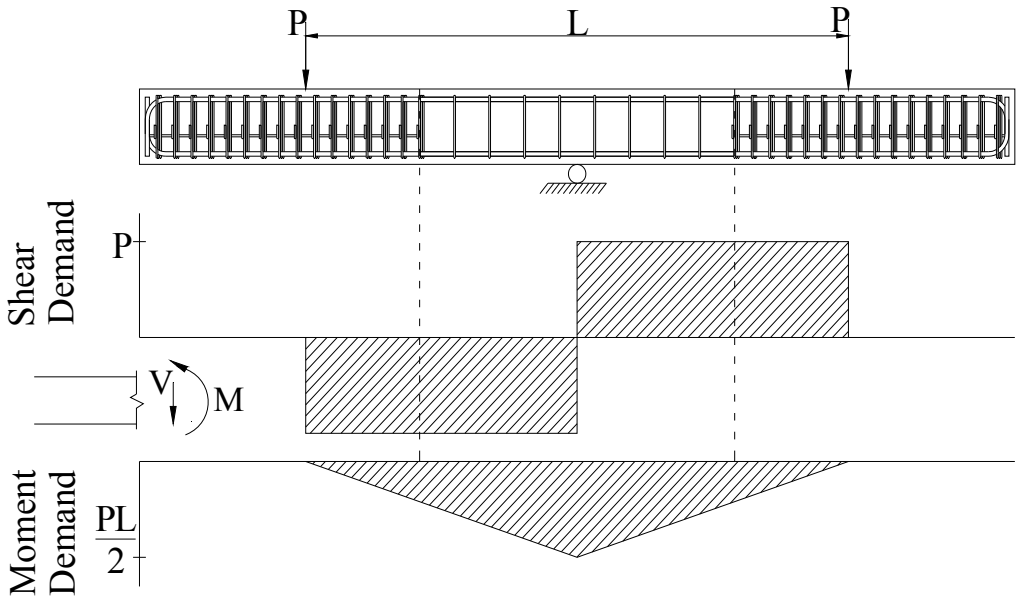

Figure 4-12 Three-point Load Test

Figure 4-13 shows the moment capacity of the LSC specimens (using an undeteriorated $l_{d,eff}$) relative to the moment demand of the three-point load test setup. The figure shows that the LSC specimens should fail under flexural loading at the center of the splice when the specimen is in a non-deteriorated state. However, if bond slip occurs, the tensile steel will not be able to yield and reduced strength would occur.

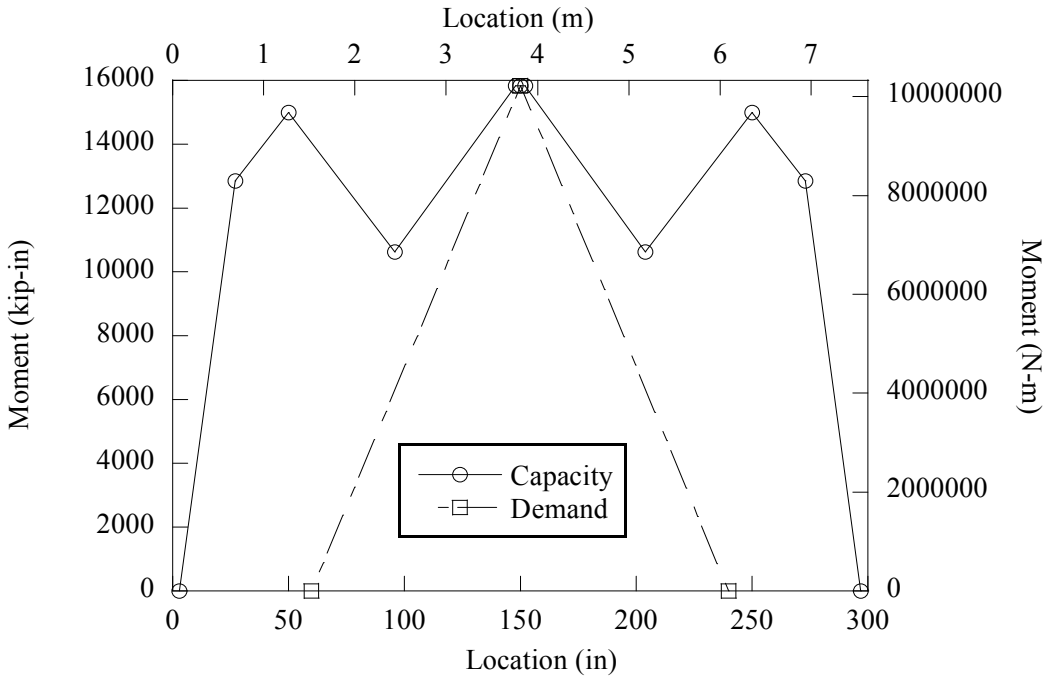

Figure 4-13 Three-point Load Test at Yield Capacity versus Demand

Shear failure also has to be considered during the three-point test due to the high shear loads across the splice. The nominal shear capacity in the specimen, V_n, is calculated according to AASHTO LRFD (2004) as follows:

$$V_n = V_c + V_s \tag{4.51}$$

where V_c is the shear resistance from the concrete and V_s is the shear resistance from the transverse steel. These can be calculated as follows:

$$V_c = 0.0316\beta\sqrt{f'_c}\,b\left(d - d'\right) \tag{4.52}$$

$$V_s = \frac{A_v f_y \left(d - d'\right)\left(\cot\theta + \cot\alpha\right)\sin\alpha}{s} = \frac{A_v f_y \left(d - d'\right)}{s} \tag{4.53}$$

where A_v is the area of steel in the hoops, s is the spacing between the hoops, and β is a factor indicating the ability of diagonally cracked concrete to transmit tension; taken as 2.0. The variables θ and α are taken as 45° and 90° respectively (AASHTO LRFD (2004)). Figure 4-14 shows the shear demand relative to the capacity at each location measured from the end of the specimen. Notice that the splice region in the middle of the LSC specimens is the critical region where shear failure might occur.

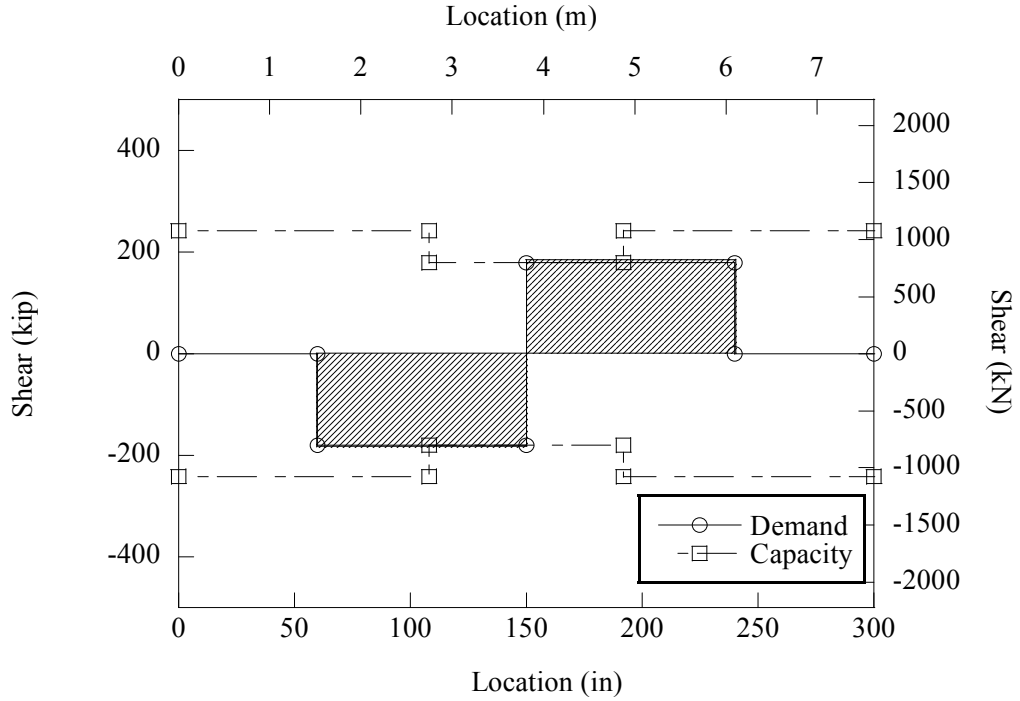

Figure 4-14 Three-point Load Test Shear Demand and Capacity

Each LSC specimen will be tested first in the four-point test then in the three-point test. This means that the tension regions will be cracked prior to loading in the three-point test, which might result in a slightly different flexural capacity prediction for the LSC specimens. With cracks already present in the concrete, the cracking stage is omitted. Figure 4-15 shows the strain predictions for the SGs versus the load, P, in the LSC specimens. The mid-span is shown as the critical section in Figure 4-13 and thus is the

first to yield and ultimately crushing the concrete in compression, presuming shear failure is diverted.

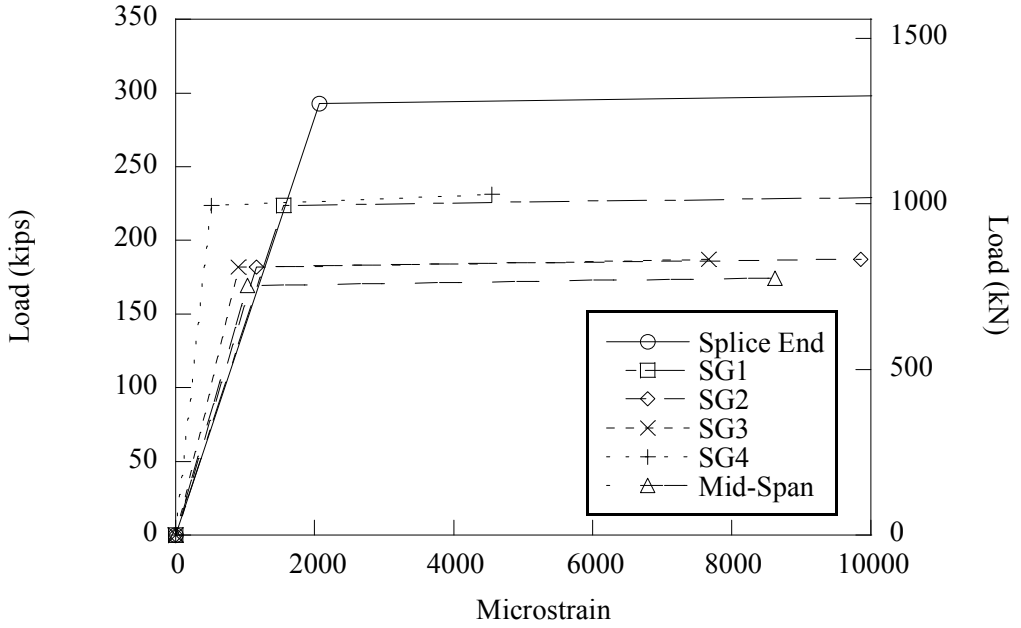

Figure 4-15 Capacity at the SG Sections for the Three-point Test Setup

The LSC specimen is expected to have a balanced failure in shear, flexure, and bond. As the load approaches 180 kips (801 kN), cracks should begin to turn from the transverse direction to 45°, as typical in shear failure. If bond is the dominating mechanism, longitudinal cracking along the reinforcing steel is expected.

The deflection analysis is similar to the four-point loading and is calculated at the load points, which are 5 ft (1.52 m) from the ends of the LSC specimens. The deflections due to flexure at the yielding of the tension steel, Δ_y, and crushing of the concrete, Δ_u, are calculated as follows:

$$\Delta_y = 2P\frac{L/2}{48E_cI_e}\left(3L^2 - 4\left(\frac{L}{2}\right)^2\right) \tag{4.54}$$

$$\Delta_u = \phi_p \frac{d}{2}\frac{L}{2} + \Delta_y \tag{4.55}$$

where L is the distance between the load points, P is the load, E_c is the modulus of the concrete, I_e is the effective moment of inertia as defined in Eq. (4.47), and ϕ_p is the curvature of the section due to plastic deformation. I_e must be recalculated for Δ_u because the neutral axis will have moved up, resulting in different values from the previous I_e at yield. Figure 4-16 shows the deflection versus the load for the three-point test.

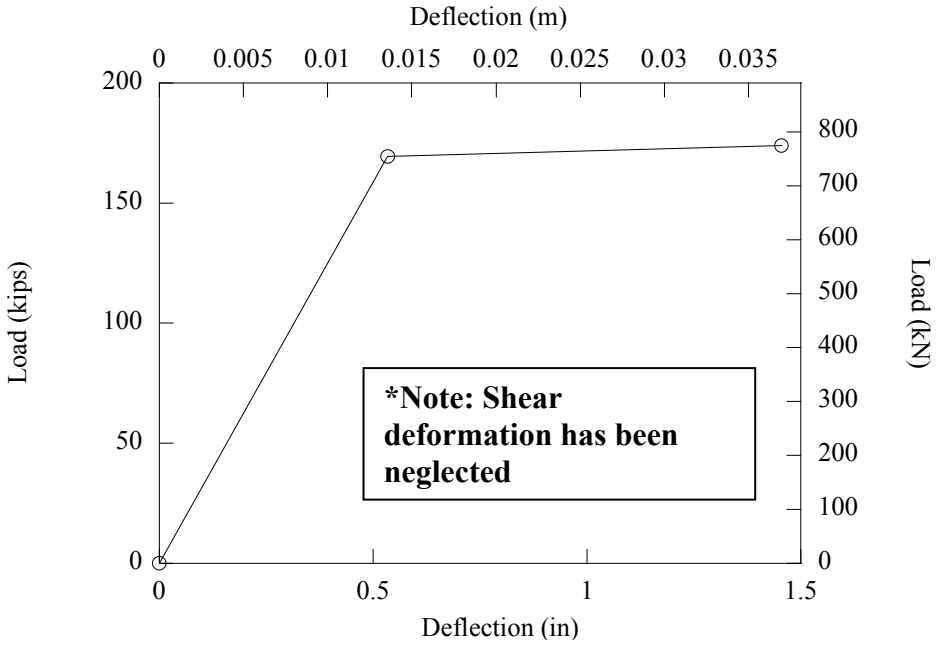

Figure 4-16 Three-point Load Test Deflection at the Load Point

4.3.3. Bond Slip Predictions

The calculations for capacity and predictions for SG measurements during testing are subject to the required development length of the reinforcement of the lap splice. If the bond is not adequate and the splice fails before the bars yield, then the provided splice length is not adequate. Because the design strength is based upon the yielding of the tensile reinforcement steel, bond failure that prevents the yielding of the steel compromises the strength and safety of the column.

During testing, the strains in the longitudinal bars will be monitored via the SG measurements. Instead of the bars deforming plastically to accommodate the high strains, the bars will start to slip with relation to the surrounding concrete. Bond slip is not expected to occur in the four-point test for the undamaged large-scale control specimens, but it may occur in the three-point test due to the significantly reduced splice length provided and the pre-cracked condition of the LSC specimens. However, as the deteriorated LSC specimens are tested, bond slip may occur in either test setup. If it occurs in the four-point test setup, the splice will be proven to have been degraded. Bond slip failure in the three-point test setup does not necessarily signify an inadequate lap splice.

4.4. Summary

Using flexure theory to calculate the strength-deformation response of the LSC specimens, analytical models can be formed to characterize the behavior of the specimens in both a four-point load test setup and a three-point load test setup. Based on the assumption that the bars develop linearly from the end of the bar to $l_{d,eff}$, the stress and strain in the bar can be calculated in the undeveloped regions of the bars. This allows for predictions to be made for strains during testing. Additionally, deflections are calculated from the strength analysis to predict the outcome of testing. These

predictions are based on non-deteriorated LSC specimens, but have a factor built into the analytical model to compensate for deteriorated specimens, which will be tested at a later date. The factor will be derived from testing to link the amount of deterioration to the structural capacity of the LSC specimens. Therefore, the aforementioned control specimens will provide a baseline for comparison of flexural and shear failure resistance.

5. EXPERIMENTAL TESTING AND RESULTS – LSC CONTROL SPECIMENS

5.1. Introduction

This section discusses the test experimental setup, instrumentation, and results for the four-point and three-point load testing of the LSC control specimens. Some results from the material properties testing will be shown, but the focus of this section is the structural performance. The LSC15 and LSC16 specimens were used as the control specimens because they were cast last of all the specimens and were kept in the Structures and Materials Testing Laboratory under dry conditions so that no ASR and/or DEF would form prior to testing. The objectives of the four- and three-point tests are to evaluate the splice region for bond strength and identify failure mechanisms in the splice region.

5.2. Four-point Flexural Load Tests

The design of the LSC specimens was based on the four-point test which applies a constant moment demand across the entire splice region. The objective of this test is to identify the structural behavior and ultimate capacity of the splice region due to flexure and the mode of failure therein. If the bars in the splice are sufficiently anchored, then the failure mechanism should develop at the splice ends and provided length of the splice meets the designed capacity. However, if the bars undergo bond slip, and the longitudinal steel does not yield, the splice length is not adequate.

5.2.1. Experimental Design and Specimen Layout

Figure 4-8 shows the LSC specimens positioned on two "pinned" supports 6 in (152.4 mm) from either end of the specimen. The "pinned" supports were bonded to the strong floor of the Structures and Materials Testing Laboratory and a thin layer of neoprene was placed between the bottom of the LSC specimens and the upper plate of the support (see Figure 5-1). The neoprene helps prevent local stresses in the concrete due to imperfections on the surface. However it does produce a slight vertical deflection during loading which is taken into account during instrumentation placement. Similar supports were positioned under the load actuators at 8 ft (2.4 m) from each end of the LSC specimens (at the splice end). The head of the actuator is also a pinned connection. To ascertain a stable system, the top plates of the supports were supported on each side by 3 bars of 2 in (51 mm) round stock to make the support a "fixed" support (see Figure 5-2). Neoprene pads were also placed between the concrete and the support to create a better interface for the transfer of forces.

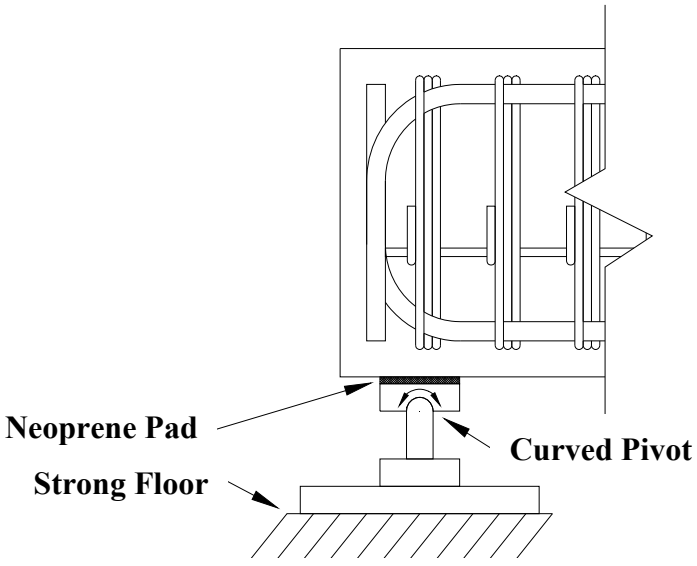

Figure 5-1 "Pinned" Support Setup

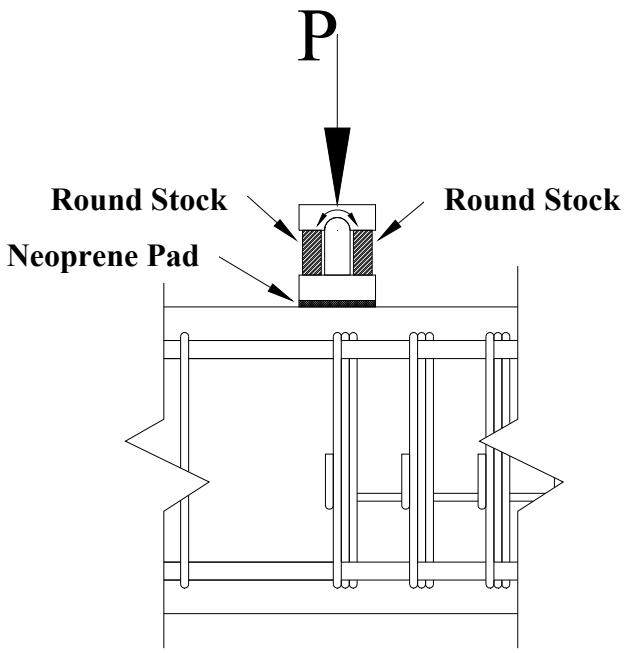

Figure 5-2 "Fixed" Support Setup

Two 220 kips (979 kN) actuators were hung from a steel frame over the LSC specimens. Calculations in Section 4.3.1 show the critical section at the splice end will yield at a moment of approximately 10,000 kip-in (1.1 kN-m) if the longitudinal steel is properly bonded. Figure 5-3 shows the actuators in position over LSC16. Note that the steel frames were anchored to the strong floor and straddle over the LSC specimens at the splice ends.

Figure 5-3 Specimen in the Four-point Test Setup

5.2.2. Instrumentation

In addition to the internal instrumentation installed during fabrication (Section 2.2), 5 string potentiometers (STR), 10 linear variable differential transformers (LVDT) and 10 externally mounted, concrete embedment gages (type KM), and strain gages were installed on the specimens. All LVDTs had a gage length of 12 in (305 mm) except for LVDT5 and LVDT7 which had a gage length of 4 in (102 mm). The LVDTs were attached to the concrete using the same brass inserts as the DEMEC points. This is shown in Figure 5-4.

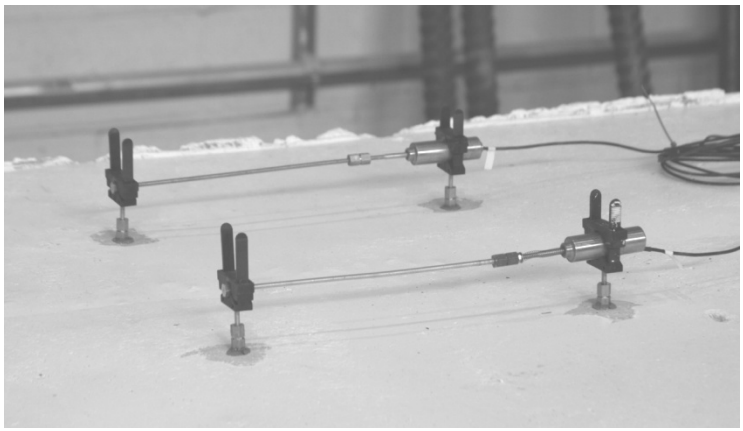

Figure 5-4 LVDT Installation Prior to Testing

The STRs were attached to the LSC specimens using the same method as the LVDTs. The KM gages were attached to the LSC specimens in a similar manner. The concrete was ground flat across the entire footprint of the KM base plates. With the concrete surface ready, the base plates were attached to a spacing bar to keep the base plates aligned and the correct distance apart for the KM gages during testing. The spacing bars were removed before testing and the KM gages were attached to the base plates (see Figure 5-5).

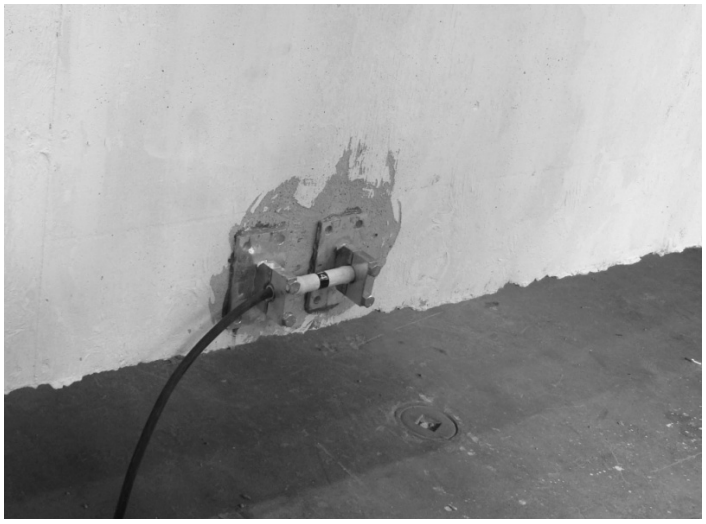

Figure 5-5 KM Gage Installation Prior to Testing

The STRs with a stroke of 4 in (101.6 mm) were used to measure vertical deflections in the specimen. To measure deflections during the tests, the STRs were placed at key locations; one at each floor support and one at each of the sections under the actuators, and one in the middle of the LSC specimens for the four-point test setup (see Figure 5-6).

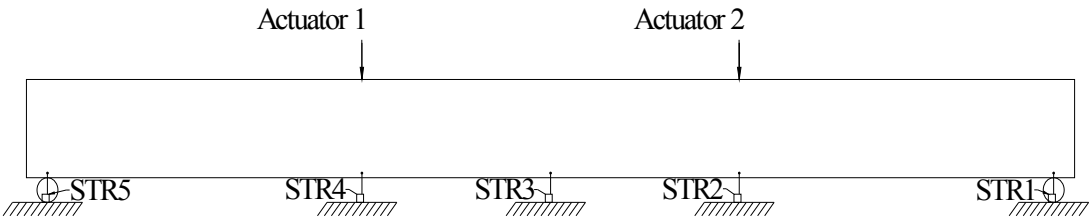

Figure 5-6 STR Locations for the Four-point Test

STR1 and STR5 were used to measure the specimen end deformation due to the neoprene padding at the supports. By subtracting the deflection of STR5 from STR4 and STR1 from STR2, the true deflection of the LSC specimens is measured.

In the first four-point test on LSC16, the placement of the KM gages and LVDTs were mirrored across the longitudinal axis of the specimen. This was done to compare the accuracy of the KM gages and the LVDTs for both compression and tension strain measurements. Figure 5-7 shows the locations of the external sensors on each face of the LSC specimens. The letters “A” and “B” are used to label each end of the specimen.

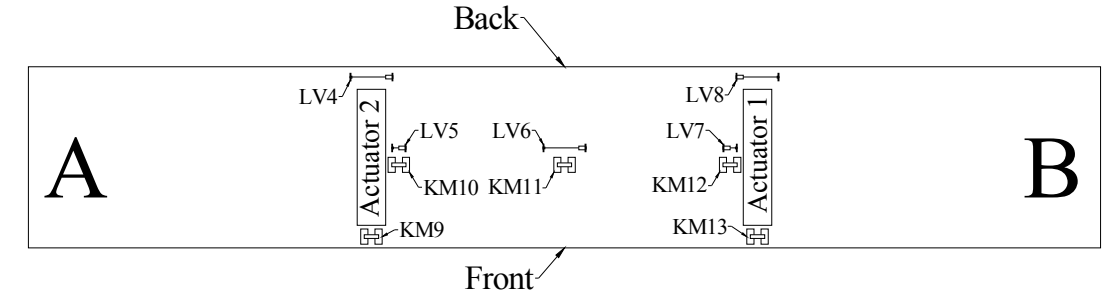

(a) Top View

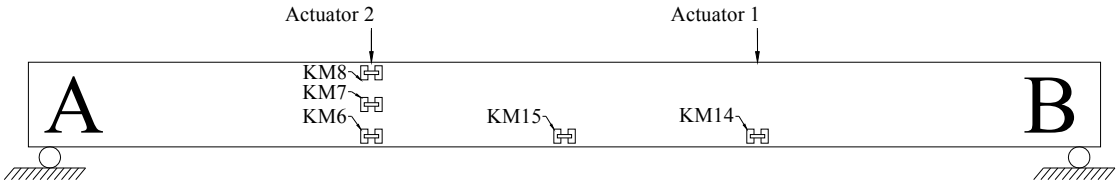

(b) Front View

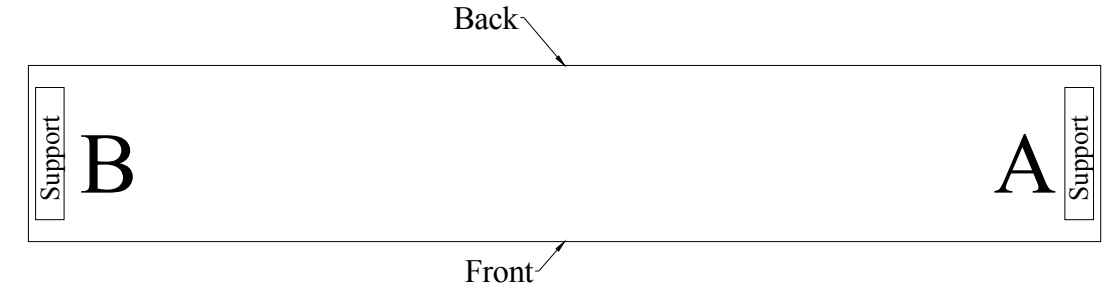

(c) Bottom View

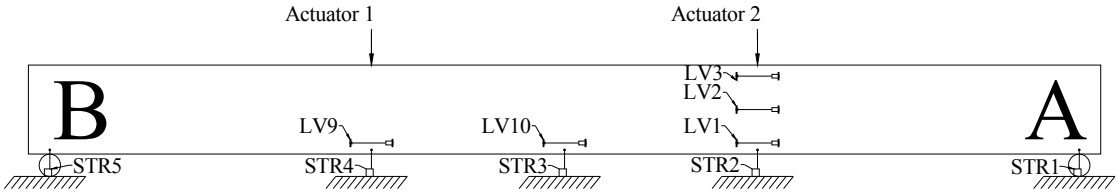

(d) Back View

Figure 5-7 External Sensor Layout for the Four-point Test of LSC16

LVDT1, LVDT2, and LVDT3 were placed 3 in (76.2 mm) from the bottom, at the centroid, and 3 in (76.2 mm) from the top, respectively, to measure the strains across the critical section (splice end). On the opposite side, KM6, KM7, and KM8 were placed in the same positions as LVDT1, LVDT2, and LVDT3, respectively. These gages will be used to verify the strain diagrams used in the analytical model and measure the strains near the splice end, which is the predicted critical region in this test.

Figure 5-7a shows the mirrored layout of LVDT4 through LVDT8 and KM9 through KM13 respectively. LVDT4, LVDT8, KM9, and KM13 were positioned next to the actuators to measure the compression strain in the outermost fibers of the critical region. Likewise, LVDT6 and KM11 were used to measure the compression strains in the outermost fibers in the mid-section of LSC16. LVDT5 and LVDT7 (KM10 and KM12) were used to check for different compression strains in the middle of the critical region compared to the gages on the side. To center the LVDT and KM gages at this location, a gage length of 4 in (102 mm) was used for LVDT5 and LVDT7 instead of the 12 in (305 mm) gage length used elsewhere. The remaining gages were placed in the tension region at the other critical section and the mid-section of the LSC specimens to measure strains at each structurally significant location. LVDT9 (KM14) was placed at the same location as LVDT1 (KM6) except on the opposite splice end, and LVDT10 (KM15) was placed 3 in (76 mm) from the bottom at the mid-section.

However, this instrumentation layout was not only used for LSC16. The instrumentation layout for LSC16 and LSC15 were different because of the knowledge gained during testing of the first specimen. From the first test, it was found that cracks in the tension region progressed through the mounting plate of the KM Gages and altered the data (see Figure 5-8). However, the KM gages provided representative data when applied to the compression regions of the LSC, so the KM gages were used for the compression regions in the following tests and the LVDTs, which measured the tension strains much better, were solely used for tension strain monitoring.

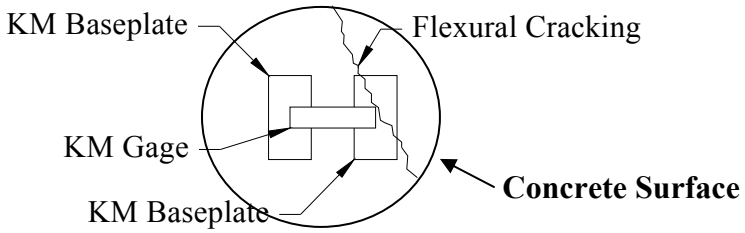

Figure 5-8 KM Gage Detail

In the four-point test on LSC15, only 9 out the 10 external KM gages were used on the compression face, KM15 was used on the side to measure the compression strain in the strain diagram. KM6, KM7, KM13, and KM14 were positioned at the splice end to measure the strains in the critical section. According to the analytical model, crushing of the concrete will occur at this location, which indicates ultimate failure of the LSC specimens. KM8, KM9, KM11, and KM12 were positioned in the center of the LSC specimens on the compression side (the top) and located above the internal strain gages in the specimen (Section 2.2.2), and KM10 was placed in the center of the mid-section of the LSC specimens to monitor compression strains in the middle of the splice. KM8 through KM12 were used to validate the strains from the internal SGs as well as provide a longitudinal strain profile across the length of the splice in the compression region.

Likewise, LVDT1 through LVDT7 were spaced along the tension region every 18 in (457 mm) to monitor the longitudinal strains along the length of the splice. Again, the purpose of this is twofold; to validate the strain measurements from the internal SGs and to create a strain profile for the splice from one end to the other. Additionally, LVDT8 and KM15 were used in conjunction with LVDT1 to produce a strain distribution across the critical region of the splice end as in the first test. Finally, LVDT9 and LVDT10 were placed on the bottom in the critical region to measure the strain in the outermost fiber of the tension region. The locations of the STRs were the same for the four-point and three-point load tests.

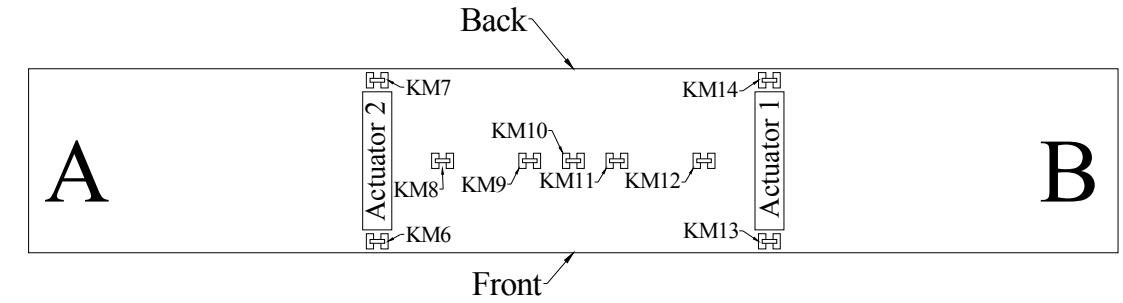

(a) Top View

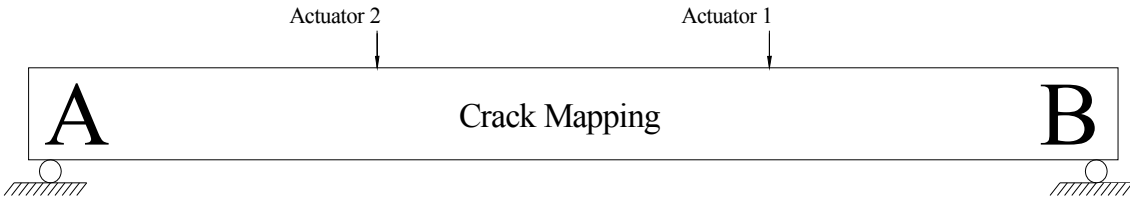

(b) Front View

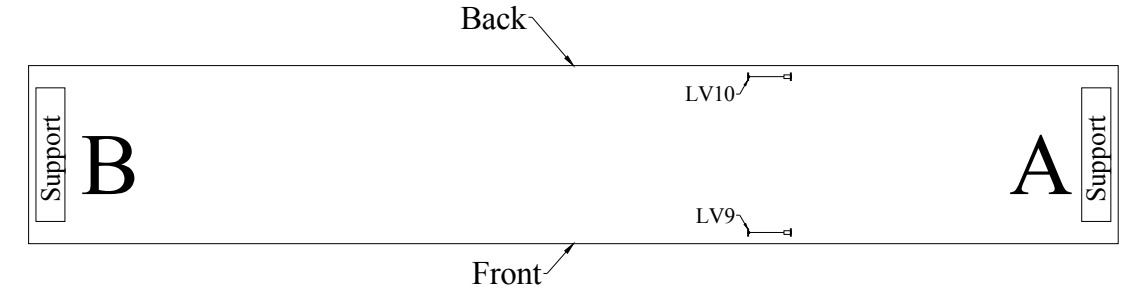

(c) Bottom View

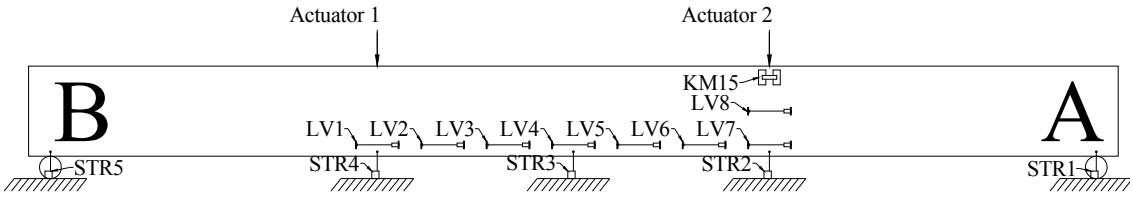

(d) Back View

Figure 5-9 External Sensor Layout for the Four-point Test on LSC15

5.2.3. Test Procedures

The internal and external gages discussed in Sections 2.2.2 and 5.2.2 were connected to a DAQ in the Structures and Materials Testing Laboratory and set to take data readings once every second. However, the internal KM gages were not installed in the LSC control specimens as discussed in Section 2.2.2 (control specimens did not expand), so no data was taken for those channels of the DAQ.

The actuators were set onto the supports prior to beginning the test. Using displacement control allowed for small differences in the load exerted on the LSC specimens by each actuator, but provided increased control over the specimen should the specimen fail unexpectedly. The actuators were placed in displacement control at 0.001 in/sec (25 μm/sec) until cracks initiated in the concrete and then the rate was increased to 0.002 in/sec (50 μm/sec) until specimen failure. In addition, the actuators were stopped periodically to map cracks and take pictures of the LSC specimens. During the loading, the instrumentation was carefully monitored to identify possible failure conditions such as crushing of the concrete and bond slip. The load testing in the four-point test lasted about 30 to 45 minutes.

5.3. Three-point Load Tests

After the four-point test was complete for a given LSC specimens, a three-point test was performed on the same specimen. Figure 4-12 shows the loading demand of the test setup. The objective of this test was to evaluate the bond performance by introducing a large flexural demand in the middle of the splice (such that the available embedment length is half the value as in the four-point test) . Due to the nature of three-point loading, high shear forces were also present in the splice region. Given the loading and specimen strength, the analytical model predicted nearly simultaneous failure criterion for bond, shear, and flexure.

5.3.1. Experimental Design and Specimen Layout

To be able to generate sufficient actuator force and to keep the instrumented side of the specimen in the tension region, the specimen was rolled 180 degrees about its longitudinal axis. In the four-point test, the tension region was on the bottom of the LSC; rolling the LSC specimen put the tension region on the top. After the LSC specimen was rolled, the supports were moved and a "pinned" support (see Figure 5-1) was placed at the mid-section of the specimen. The specimen was then balanced on the support and safety supports were placed under the ends until the actuators were in position. With the actuators spaced at 9 ft (2.74 m) as in the previous test, the analytical model calculated the LSC specimens to fail in shear during the three-point test since the moment arm was small. Therefore, the actuators were placed 15 ft (4.57 m) apart to create a higher moment demand on the mid section of the LSC specimen. This decreased the shear demand, and the analytical model calculated failure criterion for both flexure and shear at about the same load. "Fixed" supports (see Figure 5-2) were again placed on the specimen below the actuators and neoprene padding was installed between the support and the concrete, as was shown on the four-point test.

5.3.2. Instrumentation

All gages were attached to the LSC specimens in the same manner as the four-point tests and the instrumentation layout for the three-point tests was very similar to the instrumentation layout for the second four-point test. The KM gages were used for compression measurements and the LVDTs were used for tension strain measurements.

Figure 5-10 shows the layout of the KM gages, LVDTs, and the STRs. Like the second four-point test, the LVDTs were placed along the side of the LSC specimens in the tension region to measure the longitudinal strain profile of the splice region at an interval of 18 in (457 mm). Additionally, LVDT9 and LVDT10 were installed on the top side of the LSC specimens at the quarter point and center of the mid-section respectively to

measure the tension strain of the critical section at the outermost fibers. LVDT5 was placed at the centroid of the mid-section of the LSC specimens to be used with LVDT4 and KM8 (placed at the bottom for compression strain measurements) in the measurement of the strain distribution of the critical section in this test setup. Lastly, KM6 and KM7 were placed next to the support on the bottom side of the LSC specimens to measure the compression strains in the concrete in the critical section.

Three string potentiometers were used in the three-point test setup; one at the support in the middle of the LSC specimens and 2 underneath the actuators. STR1 was placed at the support to be used in calculating the deformation of the neoprene padding. STR2 and STR3 were place under actuator 2 and actuator 1 respectively and were used to measure the deflection of the LSC specimens. Again, the deflection was calculated by subtracting the deformation at the supports (STR1) from the measurements of STR2 and STR3.

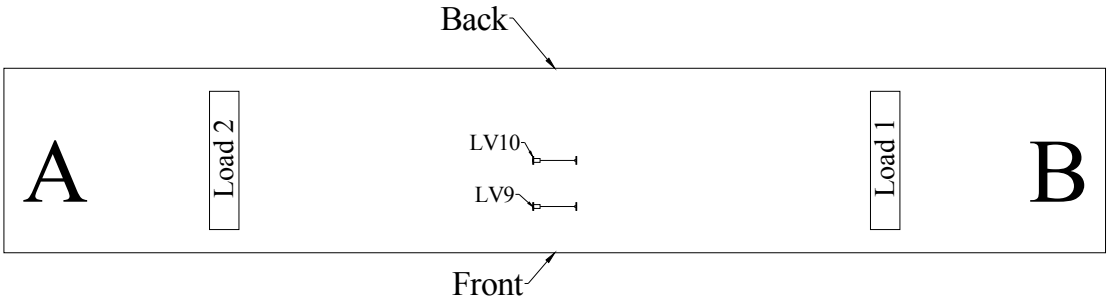

(a) Top View

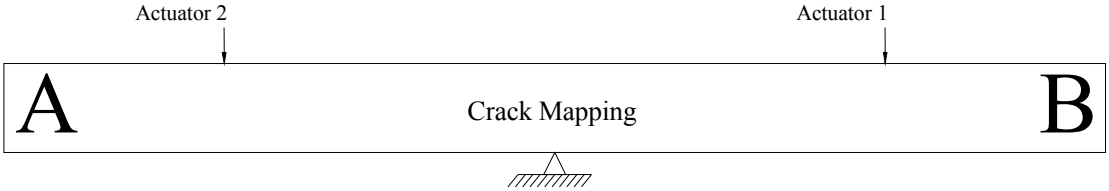

(b) Front View

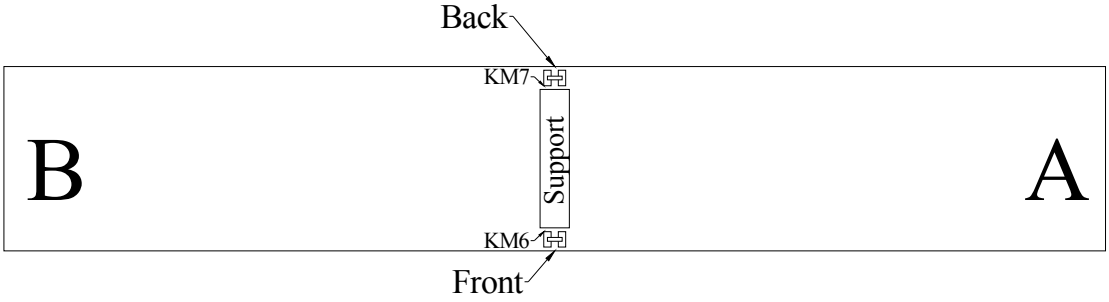

(c) Bottom View

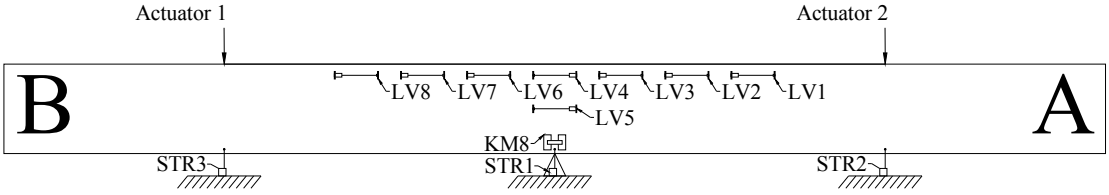

(d) Back View

Figure 5-10 External Sensor Layout for the Three-point Tests on LSC16 and LSC15

5.3.3. Test Procedures

The test procedures for the three-point test were similar to the four-point test previously described in Section 5.2.3. The only difference from the four-point tests was that a load rate of 0.002 in/sec (50.8 μm/sec) was used since the specimens were already cracked from the previous four-point tests. Additionally, when the actuators were lowered into place, the safety supports were removed from the ends of the LSC specimens prior to loading, which was not necessary for the four-point tests.

5.4. Experimental Response

During both tests, the DAQ logged data for both the internal and external sensors installed in the LSC specimens. As a point of clarification, a hydraulic valve was malfunctioning during both of the four-point tests and the first three-point test, which caused the actuators to slightly oscillate. The effects of the oscillations were minor but noticeable and will be noted in the following measured response plots. This oscillation did not affect the outcome of the load testing.

5.4.1. Material Strength Test Results

During the concrete placement operation discussed in Section 2.4.6, several 4 in x 8 in (101 mm x 203 mm) cylinders were cast. Half of the cylinders were stored in a curing room at 73.4 °F (23 °C) and 100% relative humidity (RH) as specified by AASHTO T126. The other half of the cylinders were kept with the LSC, either at the Structures and Materials Testing Laboratory or exposed to accelerated atmospheric conditions at the Texas A&M Riverside Campus. Table 5-1 shows the 28 day compression and strength results from an average of 3 specimens as specified by ASTM C39 (2001) and C78 (2007) for the compression testing and flexural testing respectively.

Table 5-1 Average 28-Day Compression and Flexural Strength Results

	Compression		Flexure
	Cured	Field	Cured
LSC	*psi*	*psi*	*psi*
15 (LSC15)	3891	3874	654
16 (LSC16)	3964	3744	752

To determine the concrete material strength at the time of LSC specimen testing, six cylinders were tested the same week as the respective tests for LSC16 and LSC15. Of the six cylinders, three cylinders were stored in the curing room (73 °F (23 °C) and > 98% RH) and three cylinders were stored with the specimen in the Structures and Materials Testing Laboratory. The test was a standard compression test, except the cylinders were instrumented with two LVDTs on the side of the cylinder to measure the strain of the cylinder relative to the axial force. The displacements from the two LVDTs were averaged and converted to strain by dividing by the gage length as follows:

$$\delta = \frac{Average(\Delta_{LVDT1}, \Delta_{LVDT2})}{L_{gage}} \tag{5.1}$$

where δ is the average strain, Δ_{LVDT} is the displacement measurement of the respective LVDT, and L_{gage} is the gage length of the LVDT. The stress in the concrete was calculated by dividing the force by the cross sectional area of the cylinder. Figure 5-11 shows the results from testing the cylinders for both LSC specimens. Also included on the graph is an analytical calculation of the stress-strain curve as developed by Tedeschini et al. (1964). The analytical model is based off the specified concrete strength of 5000 psi (34.5 MPa) and calculated as follows:

$$f_c = \frac{2f''_c\left(\varepsilon/\varepsilon_0\right)}{1+\left(\varepsilon/\varepsilon_0\right)} \tag{5.2}$$

where f_c is the stress in the concrete, ε is the strain in the concrete, and f''_c and ε_0 are the stress and strain respectively at the maxima and are calculated as follows:

$$\varepsilon_0 = 1.7\frac{f'_c}{E_c} \tag{5.3}$$

$$f''_c = 0.9f'_c \tag{5.4}$$

where f'_c is the specified concrete compressive strength and E_c is the modulus of the concrete, Eq. (4.10).

Note that in Figure 5-11 the field samples were less stiff than the cured samples in both LSC specimens and the analytical model accurately models the early behavior of the cylinders. Near the maxima, the analytical model slightly over predicts the strength of the concrete and the cured cylinders are about the same strength as the field cylinders. Also, the LVDTs malfunctioned during the testing of the second cylinders from the curing room and the field on LSC16, which is why they were omitted from Figure 5-11a.

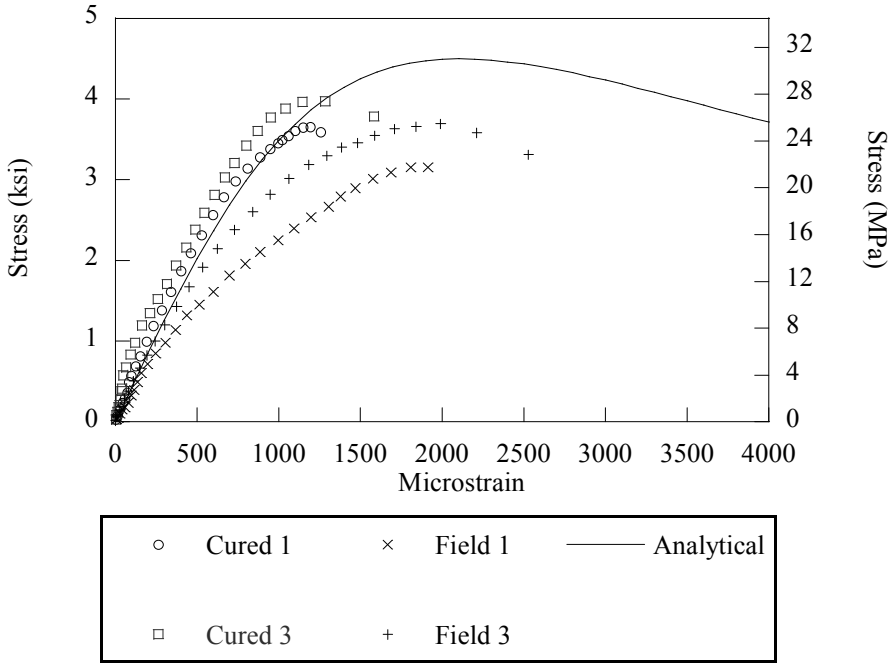

(a) LSC16

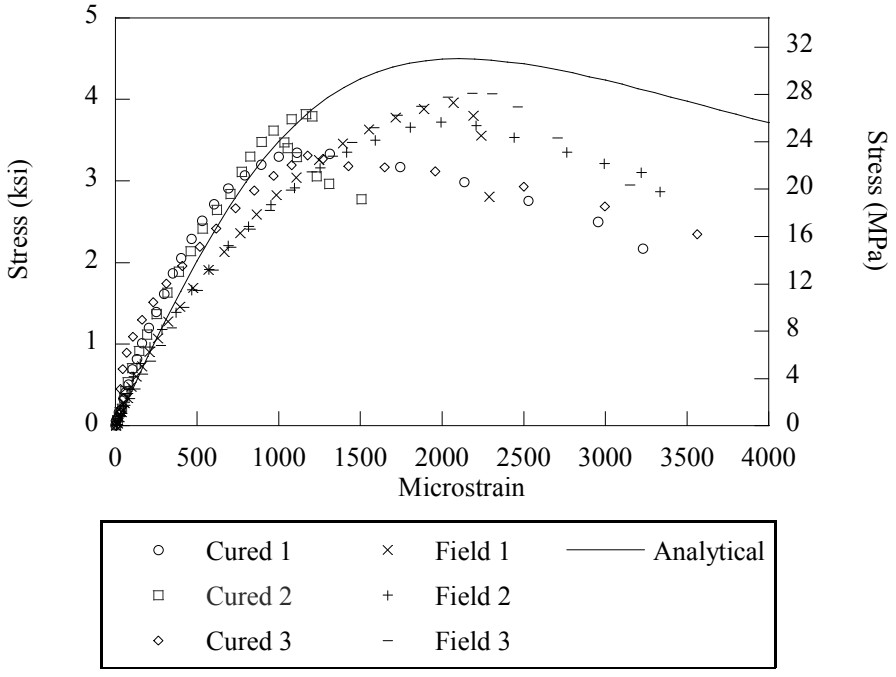

(b) LSC15

Figure 5-11 Stress-strain Plots from Cylinder Compression Tests

5.4.2. Four-point Flexural Test Results

The results from the four-point tests were completed on the LSC16 and LSC15 and are presented in this section. LSC16 was tested first and Figure 5-12 shows load versus deflection response at each actuator or load point, which also coincides with the splice ends. Note that the experimental and analytical loads and deflections correlated very well. The minor noise in the data is due to the oscillations from the hydraulic valve. The analytical model used the concrete compression strength of 4.1 ksi (28.3 MPa) and 70 ksi yield strength for the reinforcing steel instead of the specified strengths. The differences can be accounted for assumptions made in the model. For instance, the assumption of perfectly plastic steel behavior after yielding is conservative and under predicts the load capacity compared to the test results from the LSC specimen. However, this is not imperative to this model because yielding is the desired failure criteria and the tests do not need to be carried on beyond this point. Note the results from the four-point test identify cracking of the concrete and yielding of the steel, but the ultimate capacity of the specimen was not tested in order to preserve the specimen for the three-point test.

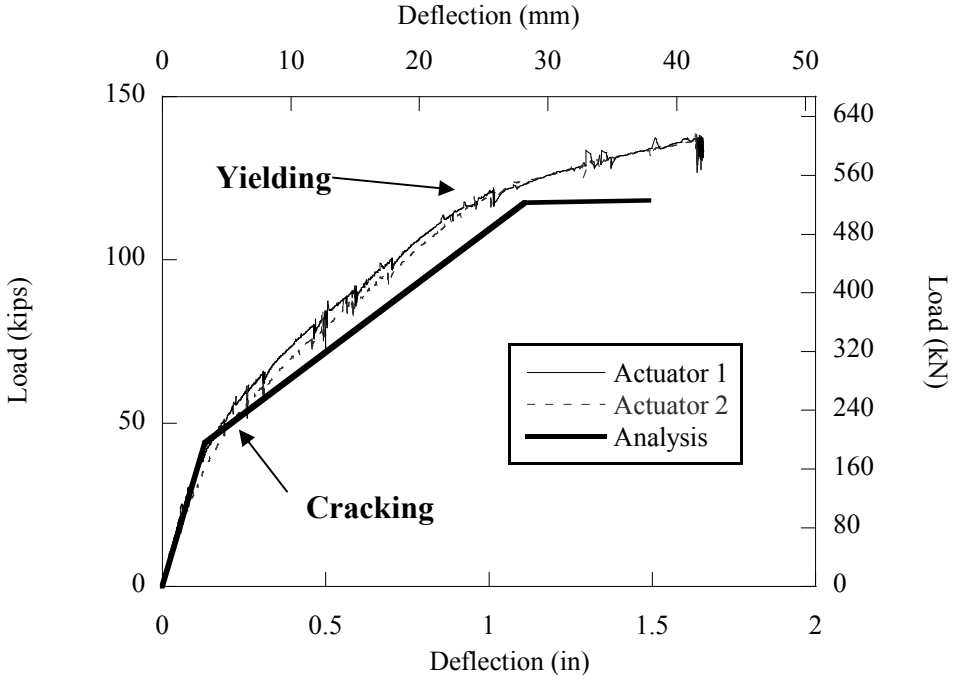

(a) LSC16

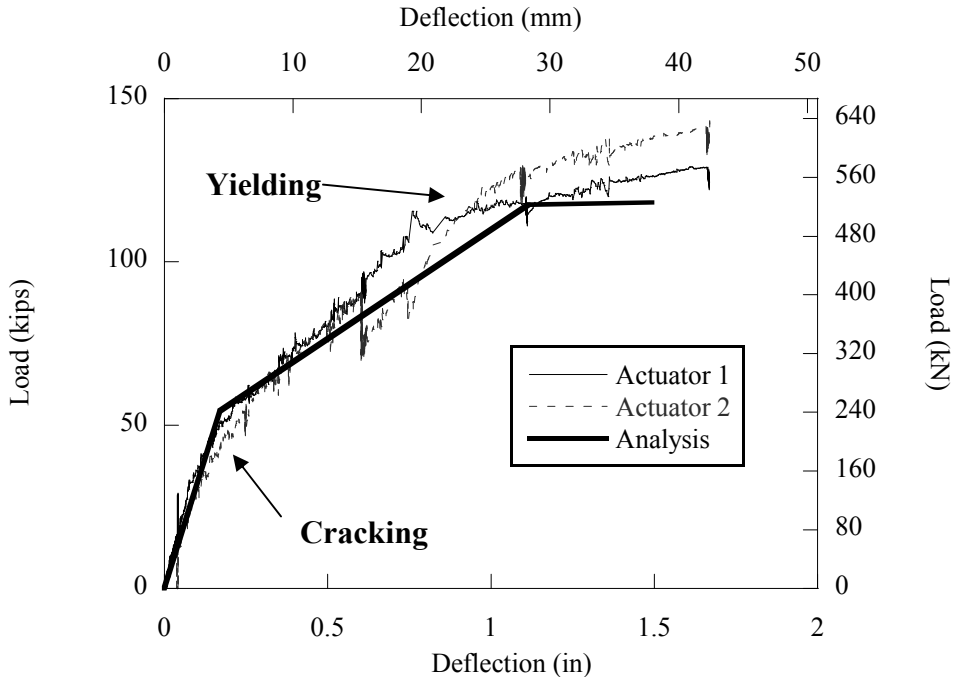

(b) LSC15

Figure 5-12 Load-deflection Curve for the Four-point Test at the Actuator Load Point (Splice End)

The remaining plots compare the strains from the internal and external gages installed on the LSC specimen and the predicted values from the analytical model. Figure 5-13 and Figure 5-14 show the load versus measured strain in each gage along the tension region of the LSC specimens along with the predictions from the analytical model. Note that the analytical model is accurate for the prediction of SG1/SG5, which are located on the bars that should be fully developed. The predictions for SG2/SG6, SG3/SG7 and SG4/SG8 are near areas of the bar that are not fully developed, which may be the reason for the under prediction of the strains by the analytical model. Also note that as the splice end begins to yield at about 115 kips (511 kN), the strain measurement in the SG closest to the end of the splice bars (SG4/SG8) cease to increase as the load increases, which implies that a failure mechanism is developing at the critical sections near the splice ends.

Figure 5-15 shows the load versus measured strains of SG9 and SG10 (strain gages on the compression steel) and the analytical predictions. The analytical model accurately predicts the response up to cracking of the concrete in tension at about 55 kips (245 kN), then the model slightly under predicts the amount of strain for a given load. This is most likely due to some nonlinear behavior of the concrete after cracking has occurred as well as the change in moment of inertia of the LSC specimens at that point.

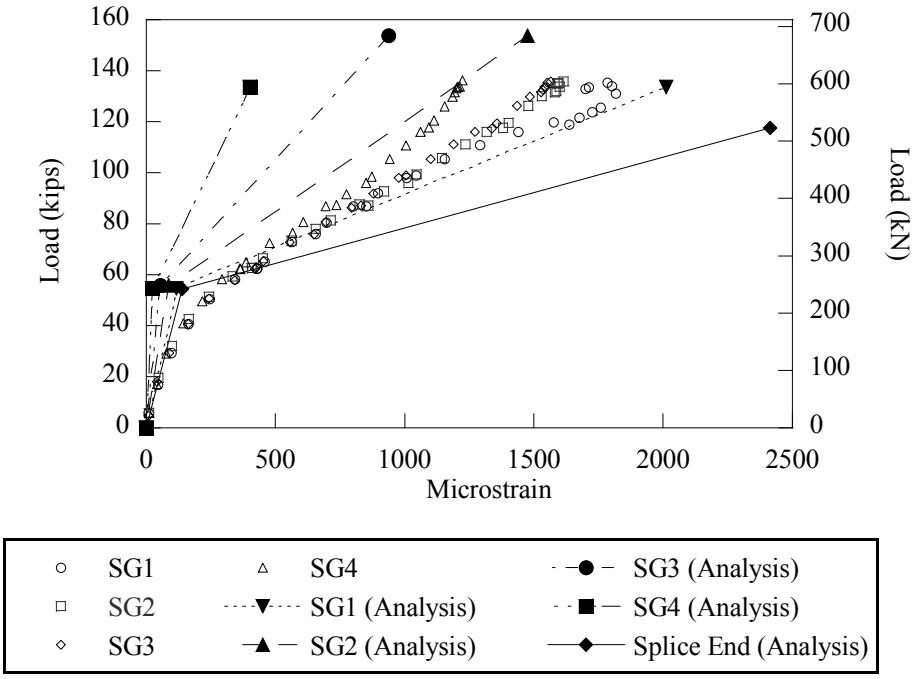

(a) LSC16

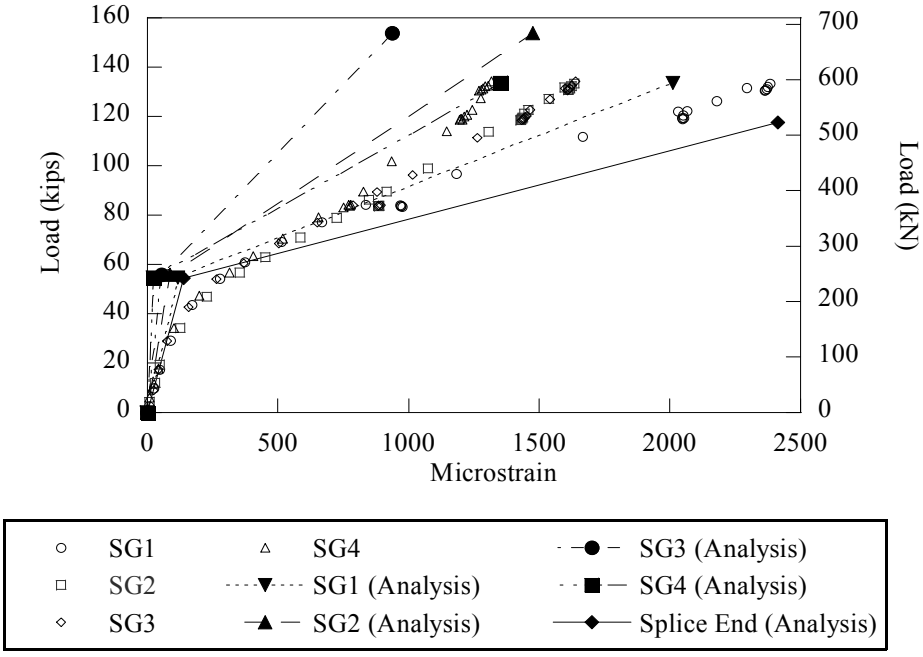

(b) LSC15

Figure 5-13 Load Versus Measured Strain in the Internal Strain Gages (SG1 through SG4) and the Analytical Predictions for Each Gage

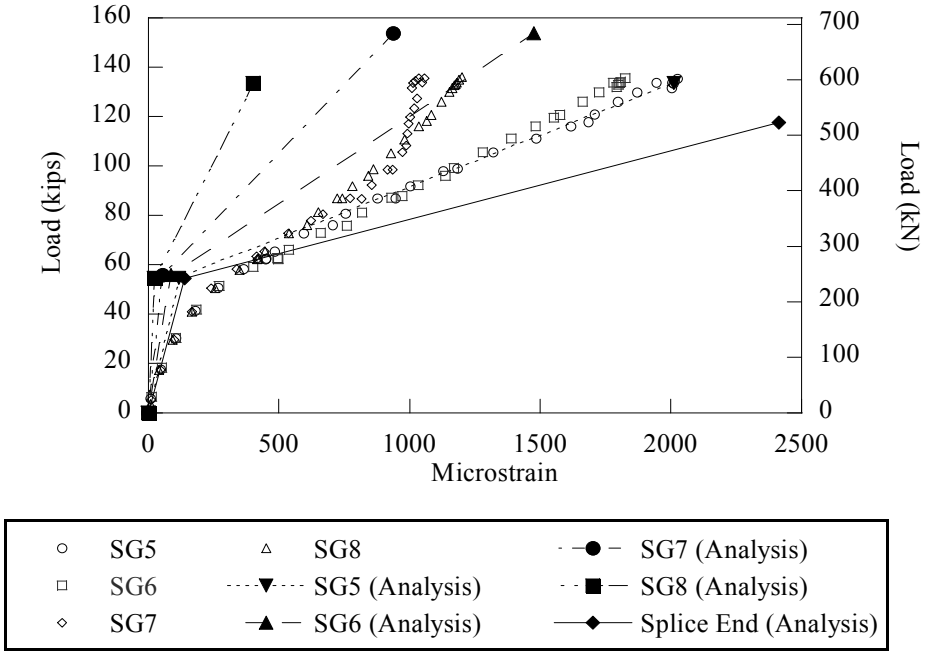

(a) LSC16

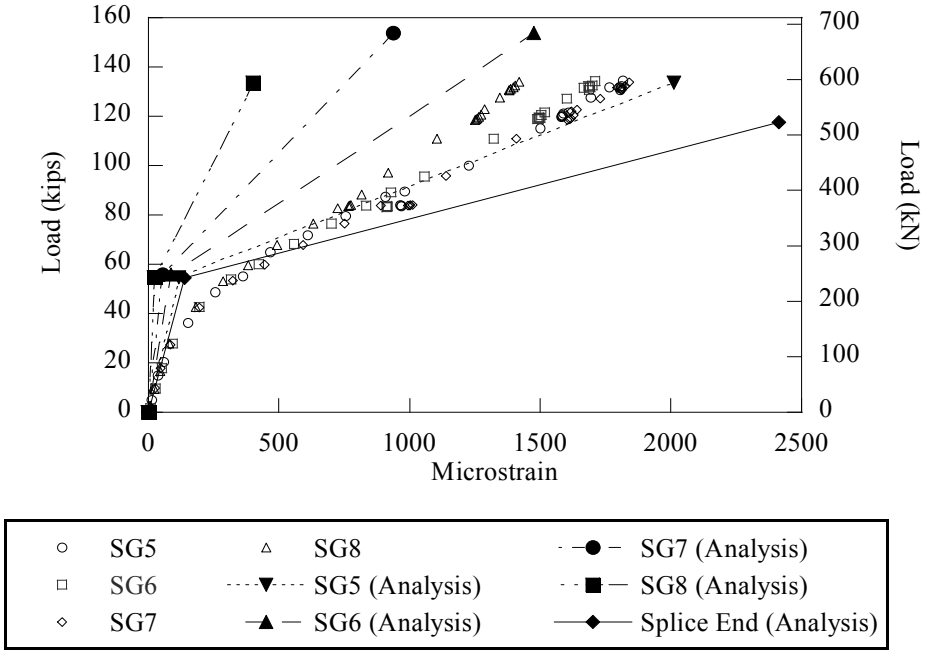

(b) LSC15

Figure 5-14 Load Versus Measured Strain in the Internal Strain Gages (SG5 through SG8) and the Analytical Predictions for Each Gage

The strain measurements of SG11 and SG12, the strain gages on the hoops in the splice region, were negligible due to the lack of shear in this test setup. These gages will be further discussed in the results from the three-point test setup where shear is more prevalent in the splice region.

Figure 5-16 shows the load versus measured concrete surface strain readings in the critical section under the actuator. The figure shows that strain diagram changes with respect to the applied load. The strain at the centroid does not increase much until the concrete begins to crack. Then as the neutral axis begins to move up, the strains gradually increase in the centroid. At yielding of the reinforcement, both the strain gage measurements and the analytical model show a sharp turn in the data in the tension region. Also notice the high strains (above 12000μst) measured at the tension steel level. In further comparison of the analytical model and the measured strains, the strain in the analytical model does not increase as fast as the measured strains in the tests. This signifies that the steel in the LSC specimens is more ductile than the analysis or that the neutral axis has moved higher than the analysis predicted.

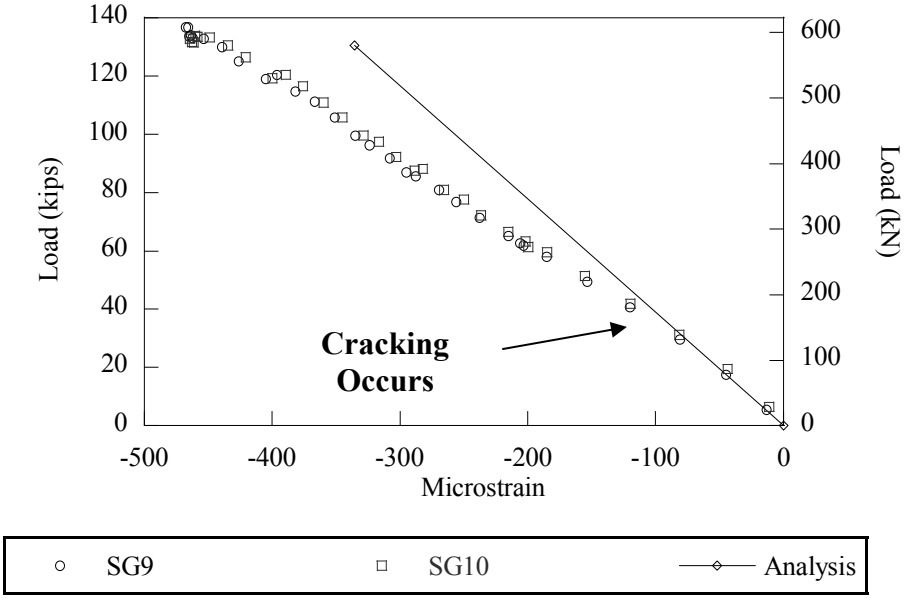

(a) LSC16

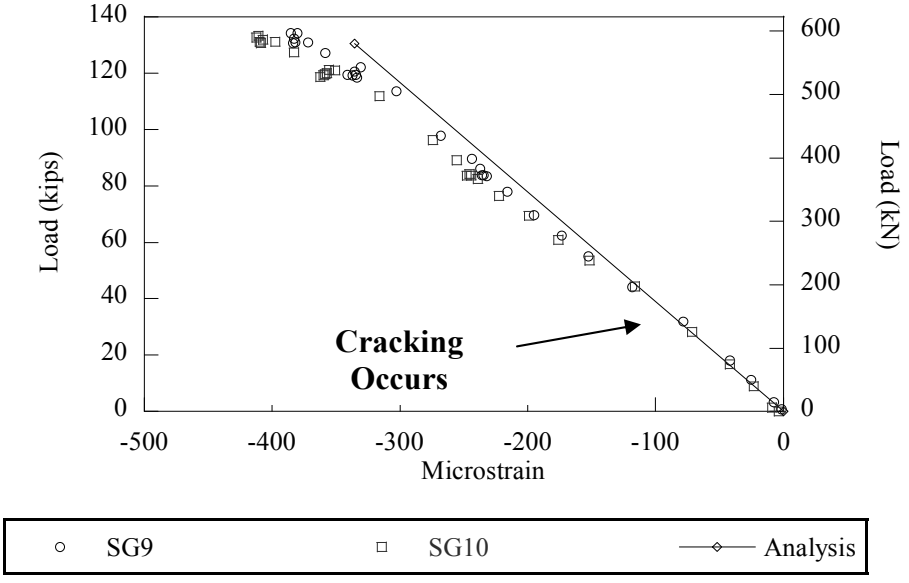

(b) LSC15

Figure 5-15 Load Versus Measured Strain of the Internal Strain Gages in the Compression Region (SG9 and SG10) and the Analytical Predictions

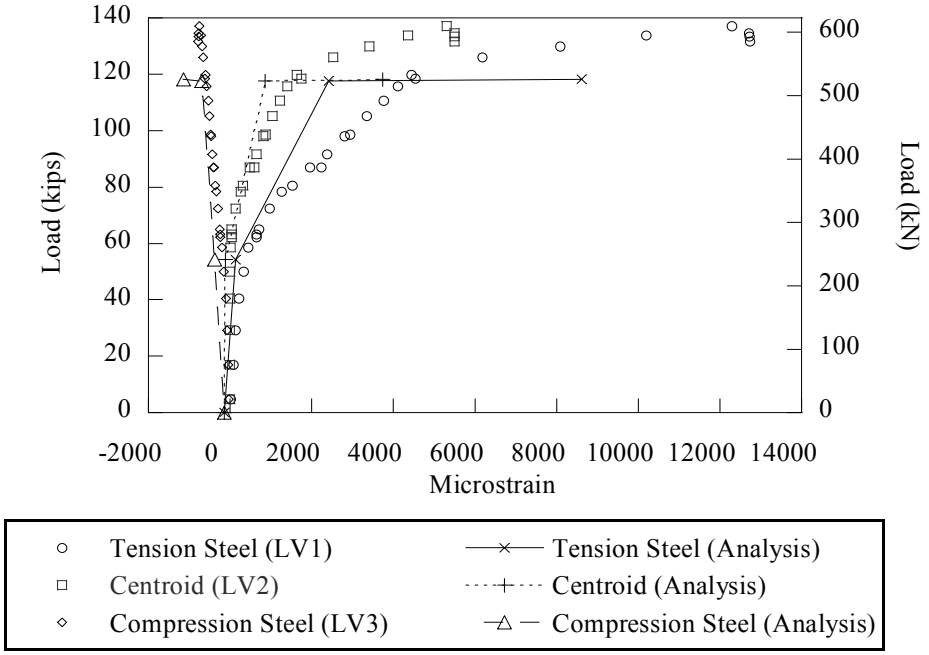

(a) LSC16

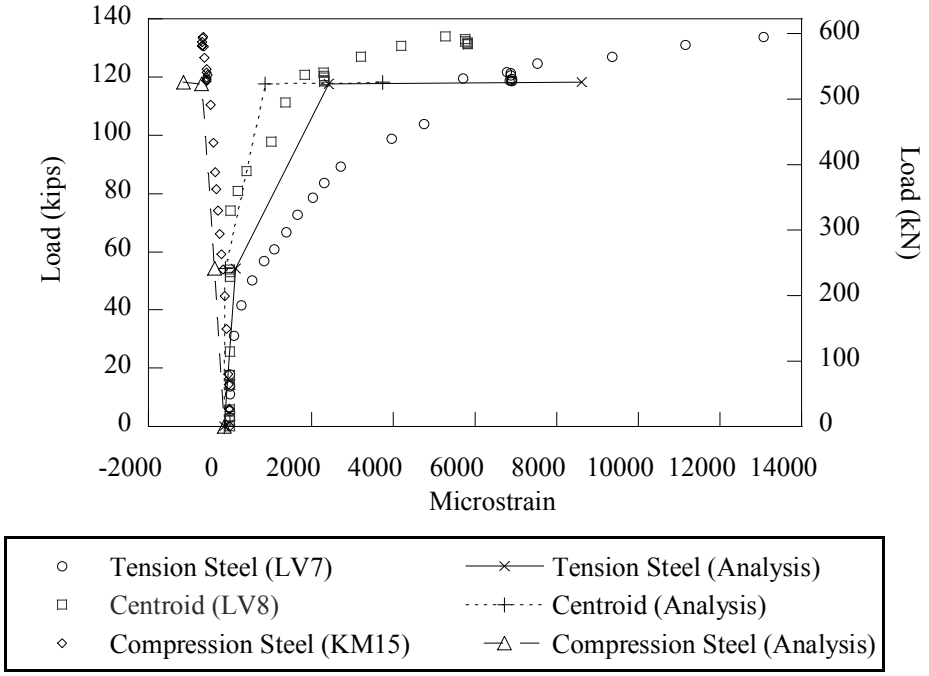

(b) LSC15

Figure 5-16 Load Versus Measured Strain of the External Strain Gages across the Depth of the Critical Section and the Analytical Prediction

The remaining results pertain to LSC15 only because the data from LSC16 was used to evaluate the locations of the LVDTs and KM gages. Figure 5-17 shows the strain profile of the LVDTs along the length of the splice in the tension region, where LVDT1 is at one splice end and LVDT7 is at the other. The strain measurements from LVDT1 and LVDT7 indicate that the reinforcing steel in the critical section yielded at approximately 115 kips (512 kN) and the steel in the other sections have remained in the elastic region. This shows that the failure mechanism is isolated to the splice ends and did not spread across the splice. This indicates again that, the splice is adequately bonded. Also, notice that LVDT4, which is positioned in the middle of the splice, has the smallest strain, which was predicted by the analytical model (see Section 4.2.3).

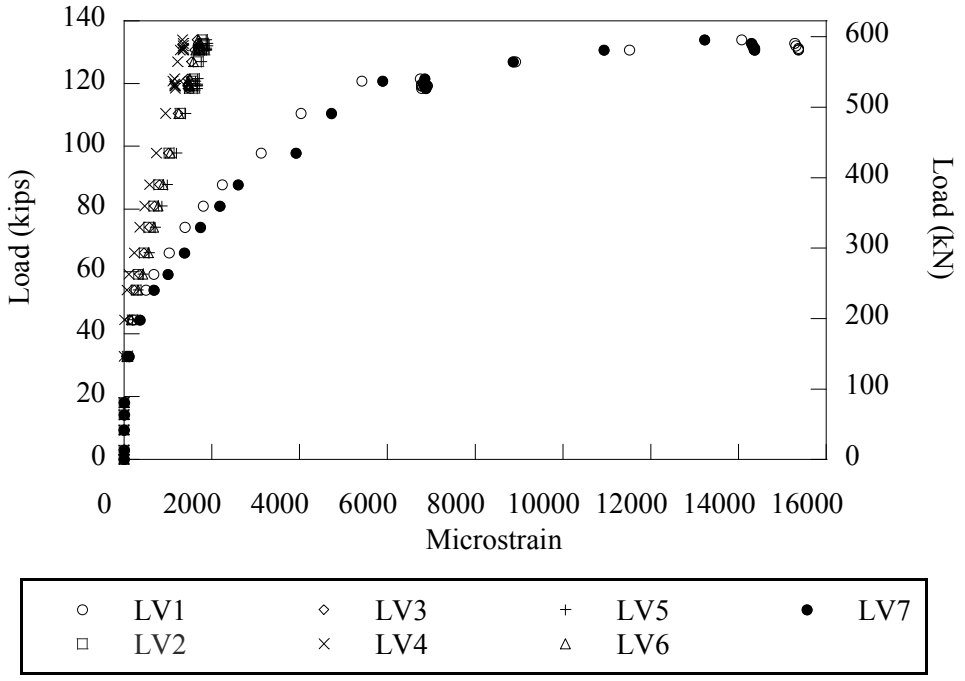

Figure 5-17 Load Versus Measured Strain in the LVDTs across the Splice Length in the Tension Region of LSC15

Figure 5-18 shows the corresponding concrete surface strains across the compression side of the splice region. Note the higher strains in the gages closest to the critical

section, KM8 and KM12. This figure clearly shows that the test was stopped before the concrete crushes because the specimen did not strain beyond the conservative crushing

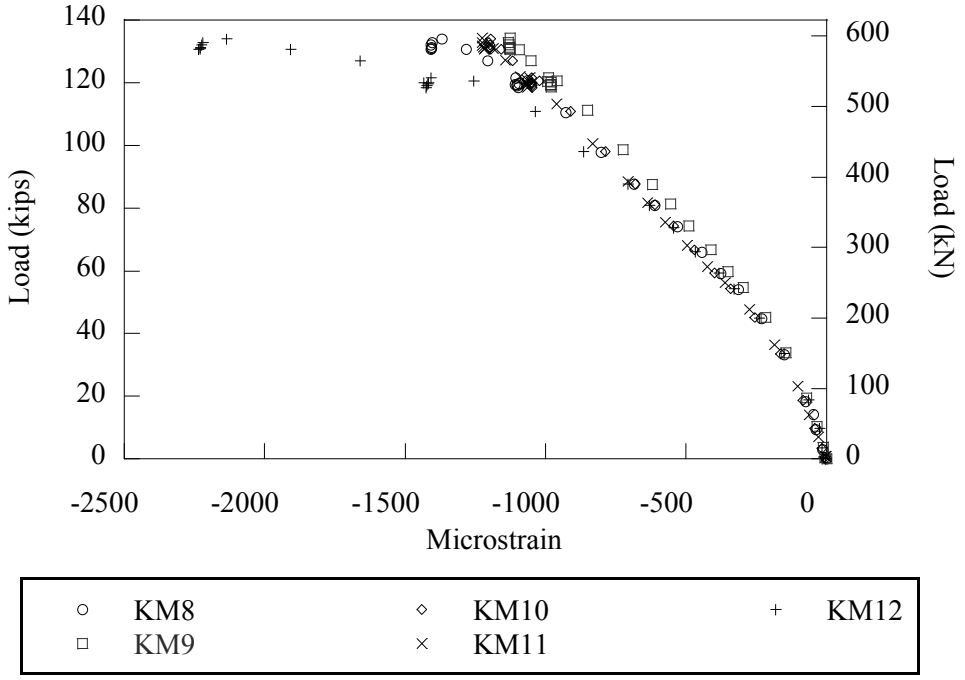

Figure 5-18 Load Versus Measured Strain in the KM Gages along the Splice Length in the Compression Region of LSC15

strain of 300 microstrain KM8 and KM12 are not positioned directly over the splice end because the support for the actuators spanned the middle 3 ft (914 mm) of the top. Therefore, 4 KM gages were positioned next to the support to capture the strains directly above the splice end. Figure 5-19 shows the strains measured by KM6 exceeded the assumed crushing strain of 3000 microstrain. However, the concrete did not crush, which indicates that the crushing strain is conservative.

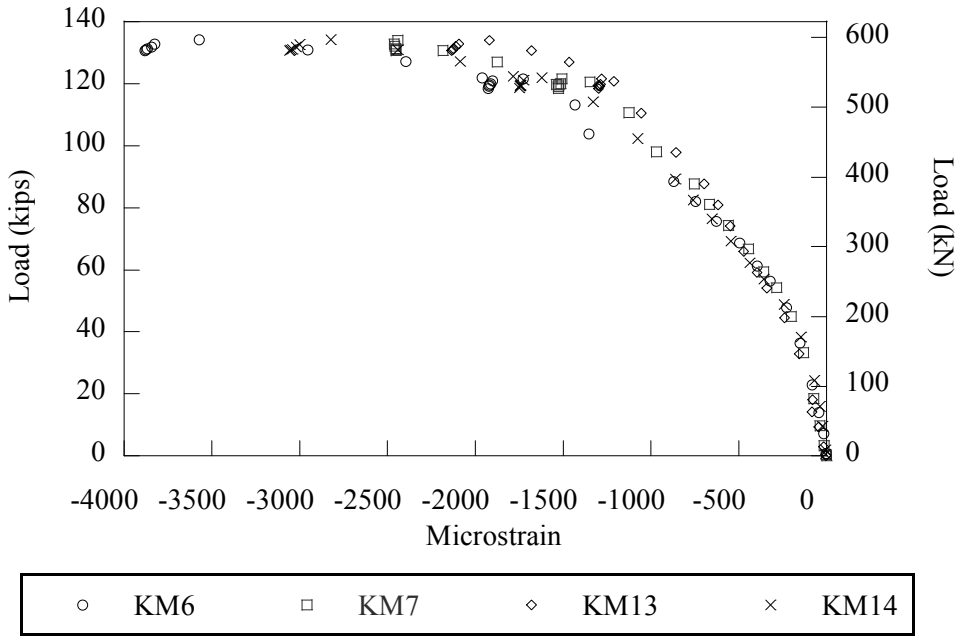

Figure 5-19 Load Versus Measured Strain in the KM Gages at the Splice End in the Compression Region of LSC15

Figure 5-20 shows a comparison of LVDT7 which is mounted on the side of the LSC specimen and LVDT9 and LVDT10, which were mounted on the bottom of the specimen. There was no appreciable difference between the two different mounting conditions, which indicates that the extra effort required to mount the LVDTs was not necessary. Figure 5-21 shows the flexural crack on the bottom of the LSC specimen in the tension region of the splice end.

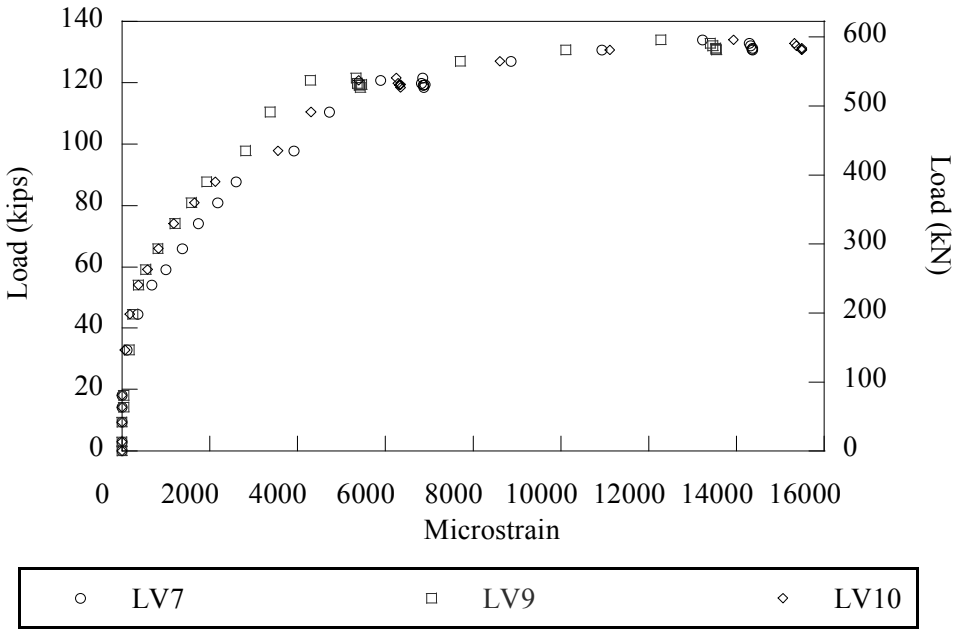

Figure 5-20 Load Versus Measured Strain in the LVDTs at the Splice End in the Tension Region on LSC15

Figure 5-21 Tensile Crack at the Splice End on the Bottom

5.4.3. Three-point Flexural/Shear Test Results

LSC16 and LSC15 were tested in the three-point load test configuration discussed in Section 5.3 after the four-point test. Figure 5-22 shows the deflection of the specimen in the three-point load test setup and the load-deflection curves in Figure 5-23 show the deflections of each side on the LSC specimens relative to the actuator applying the load to that end. Note that the cracking stage of the analytical model is omitted due to the prior cracking that occurred in the four-point test. In addition, the results from the test coincide with the yield capacity of the LSC specimen, but the specimen also experienced some bond slip. However, the failure of both modes was nearly simultaneous as evident from the rounding of the load-deflection curve which signifies the onset of yielding. An offset is also present in the results from the test due to the test configuration and displacement control. Once the test was started, one actuator would remain slightly ahead of the other for the remainder of the test.

Figure 5-22 End View of the Deflection during the Three-point Test

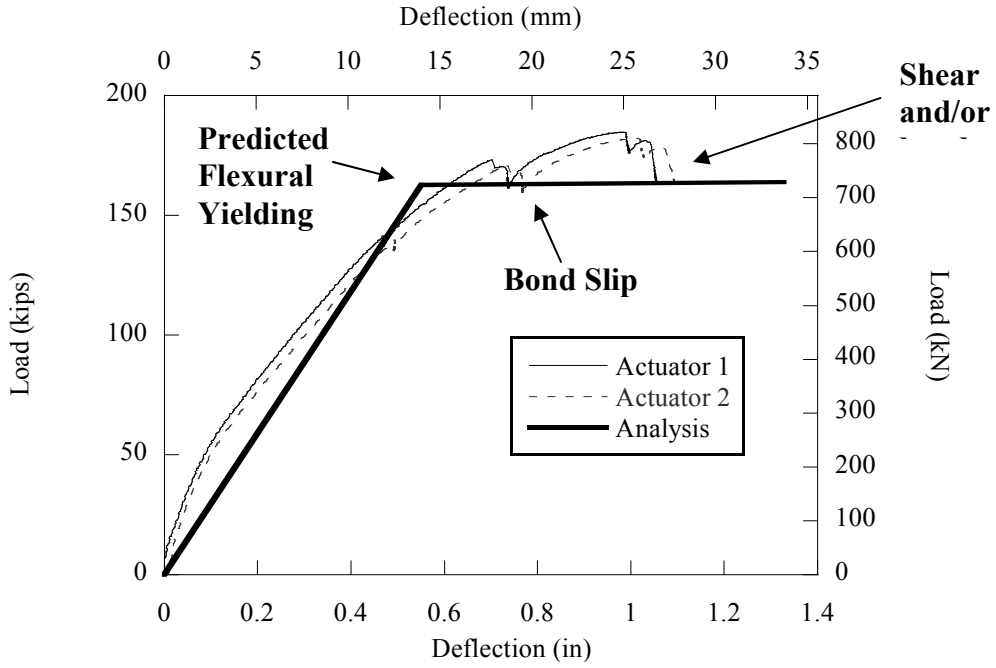

(a) LSC16

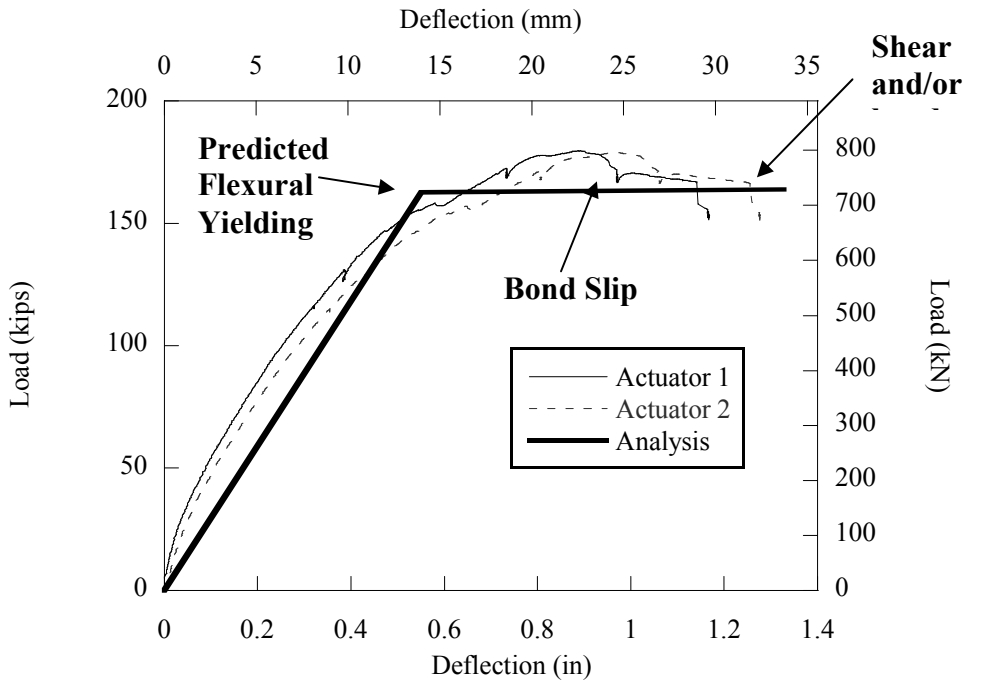

(b) LSC15

Figure 5-23 Load-Deflection Curve for the Three-point Test at the Actuator Load Point

Like the four-point test results, predictions were made for the three-point test using a similar analytical model that takes into account the triangular moment demand on the LSC specimens. Figure 5-24 shows the load versus measured strains in SG1 through SG4 for both LSC16 and LSC15. On LSC16, both SG1 and SG4 experienced bond slip as indicated by the increase in load and the reduction in strain when the load reached 300 kips (1.33 MN). However the slip conditions did not reach far enough into the splice to cause the bar at SG2 or SG3 to lose bond with the concrete. On LSC15, SG3 malfunctioned prior to the tests and did not provide any measurements during the test. Also, compared to LSC16, only SG4 measured strains indicative of bond slip.

Likewise, Figure 5-25 shows the strain measurements for SG5 through SG8. On LSC16, all strain gages exhibited bond slip; first SG4 began to slip, then the other three gages did the same. However, on LSC15 only SG4 exhibited bond failure while the other three gages continued to increase in strain as the load increased.

The analytical model showed good results for SG3 and SG4 but over predicted the strains in the reinforcing steel at SG1 and SG2, most likely due to the assumption for the reinforcing steel being perfectly plastic.

Figure 5-26 through Figure 5-28 show the results for the remaining strain gages. The data shows that the bars began to lose bond at SG9 and SG10. For both LSC specimens, SG9 was the first to lose bond, which indicates that bond slip can occur on either bar in a section.

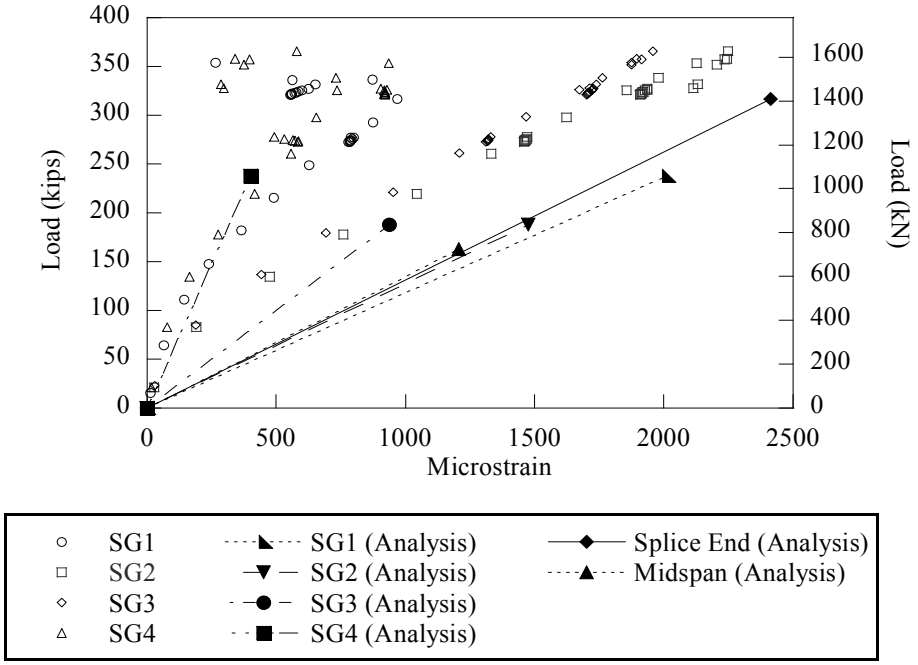

(a) LSC16

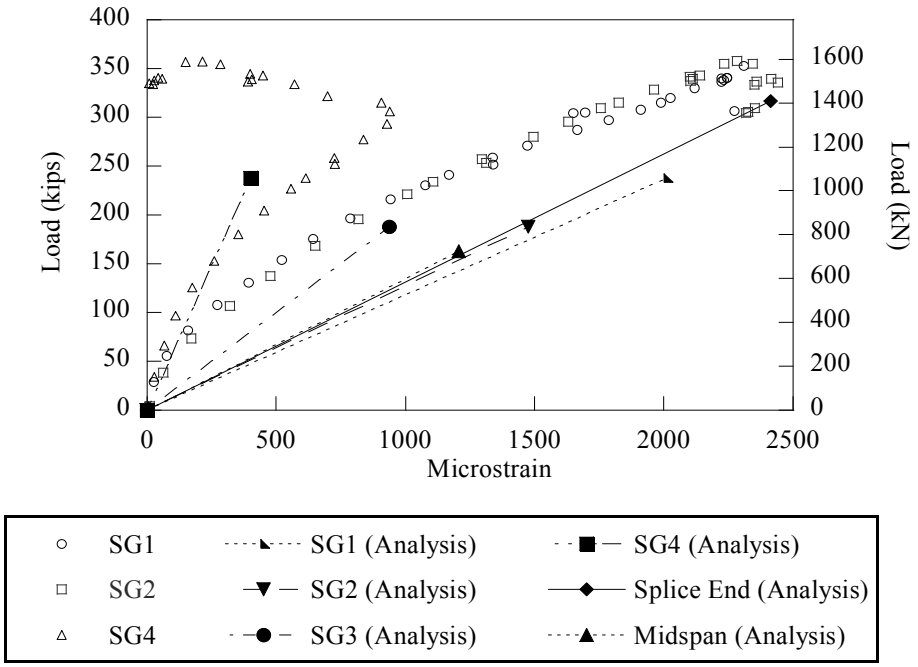

(b) LSC15

Figure 5-24 Load Versus Measured Strain in the Internal Strain Gages (SG1 through SG4) and the Analytical Predictions for Each Gage

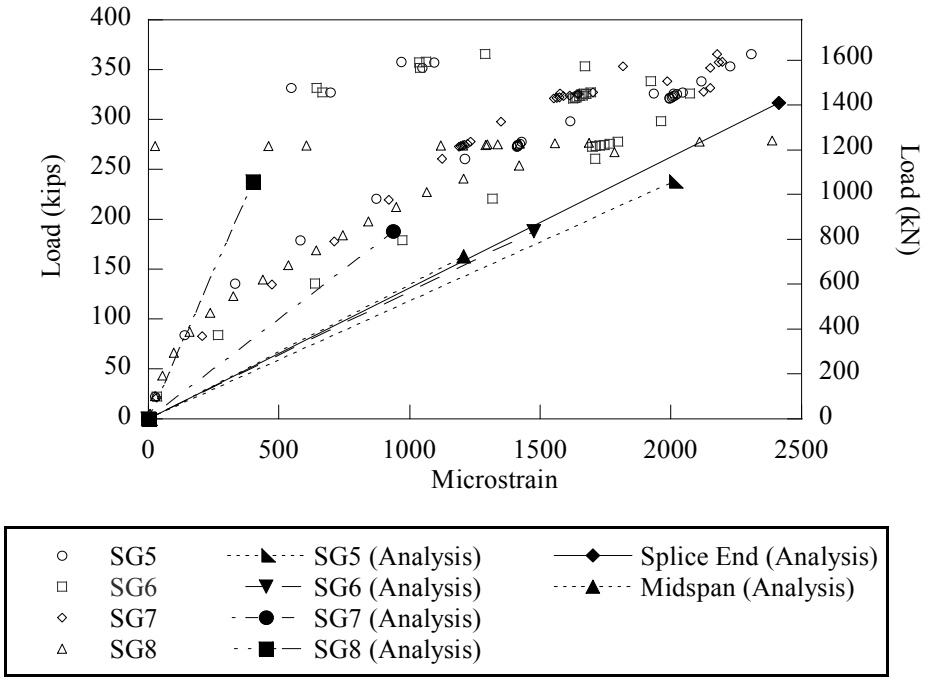

(a) LSC16

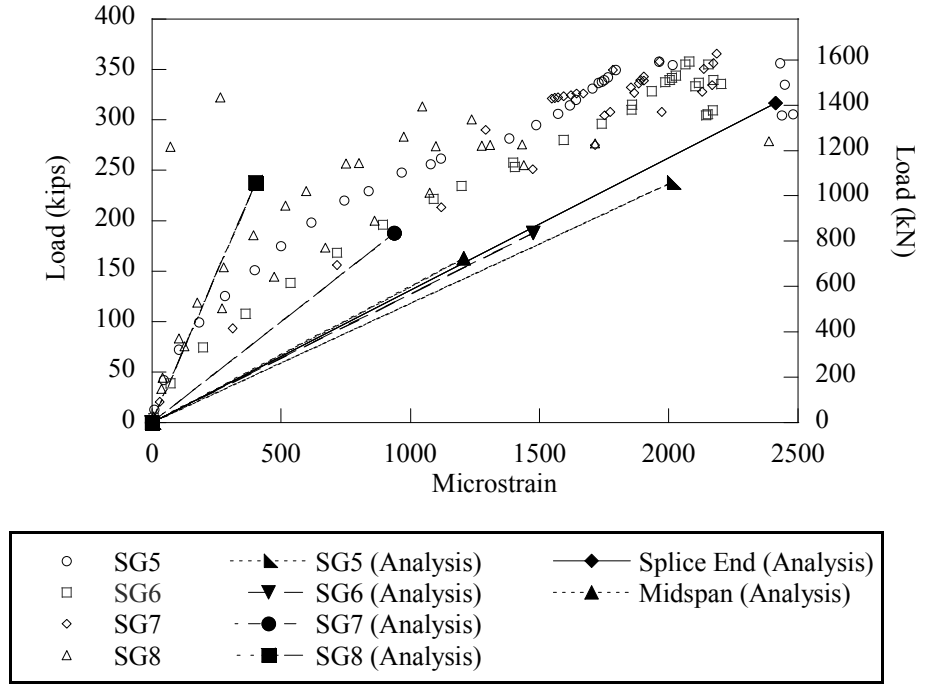

(b) LSC15

Figure 5-25 Load Versus Measured Strain in the Internal Strain Gages (SG5 through SG8) and the Analytical Predictions for Each Gage

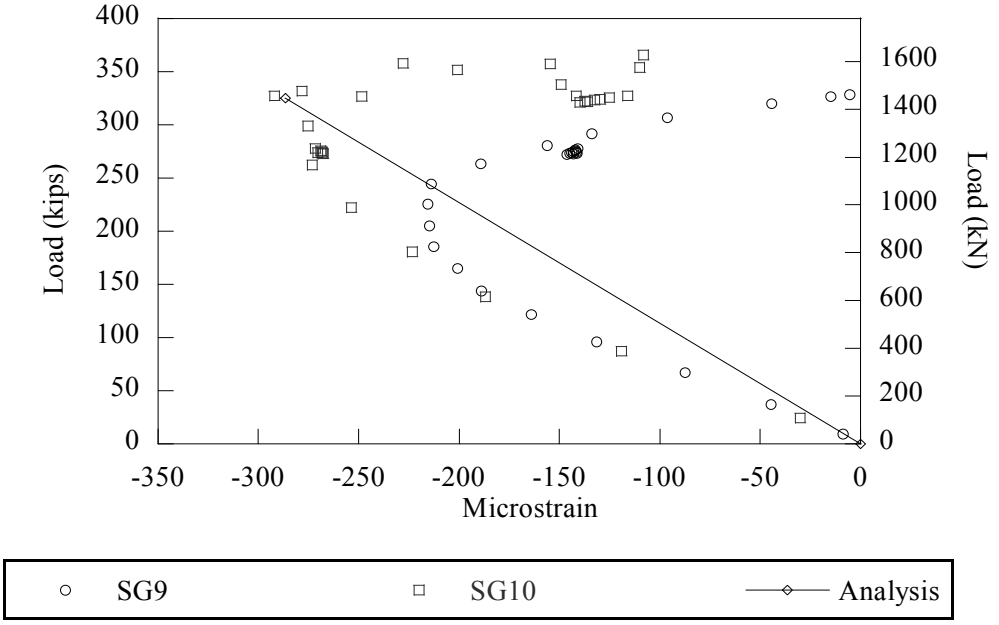

(a) LSC16

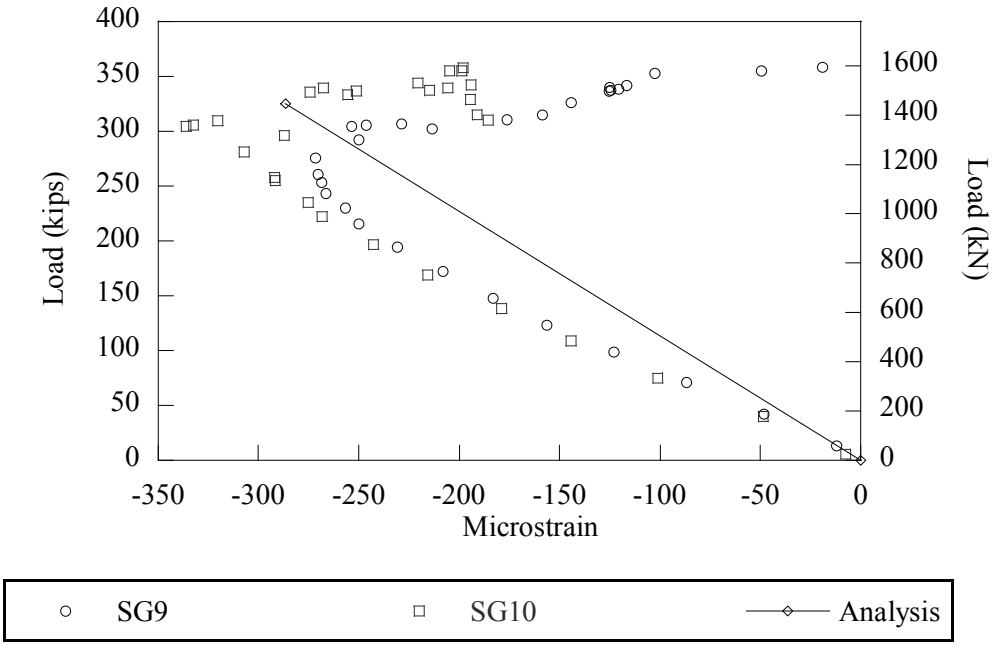

(b) LSC15

Figure 5-26 Load Versus Measured Strain in the Internal Strain Gages (SG9 and SG10) and the Analytical Predictions for Each Gage

One of the differences in the three-point test and the four-point test is the addition of shear demand in the splice region (see Figure 5-27). Shear demand is resisted by the concrete and by transverse reinforcement (hoops). Figure 5-28 shows the strain in the hoop at the mid-section of the LSC specimens. Notice that the strains do not increase appreciably until bond slip has occurred in the longitudinal steel. This is possibly due to the location of the instrumented hoop. Shear cracks formed near the splice end, which stressed the hoops near that location more than the center where the moment demand is higher. Figure 5-27 shows shear cracks near the splice end extending down towards the support. The cracks near the instrumented hoop were mostly tension cracks from the moment demand.

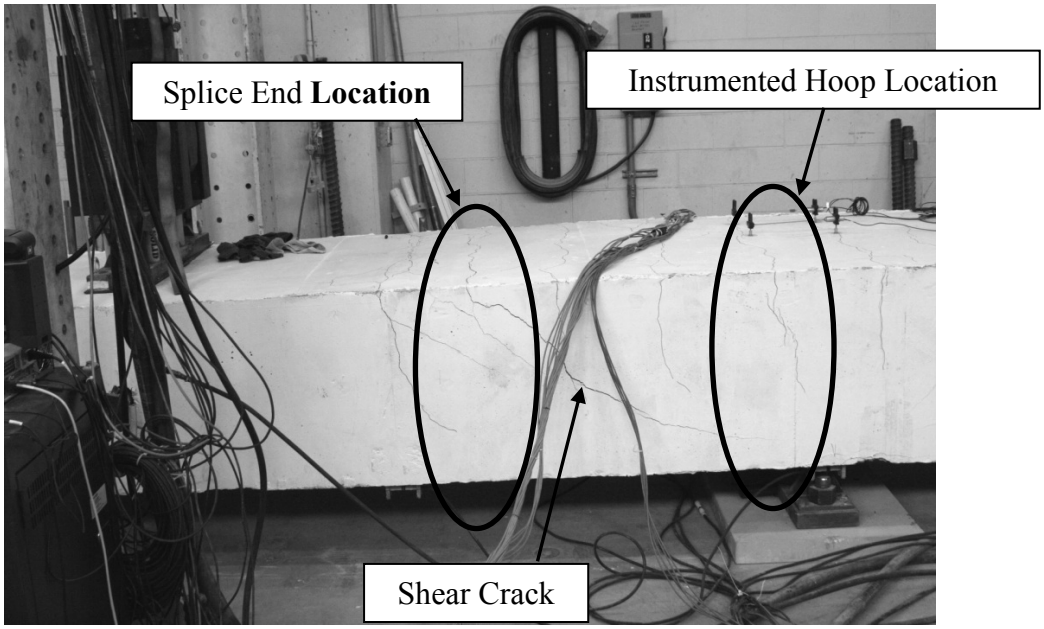

Figure 5-27 Shear and Tensile Cracks on the LSC Specimens in the Three-point Test

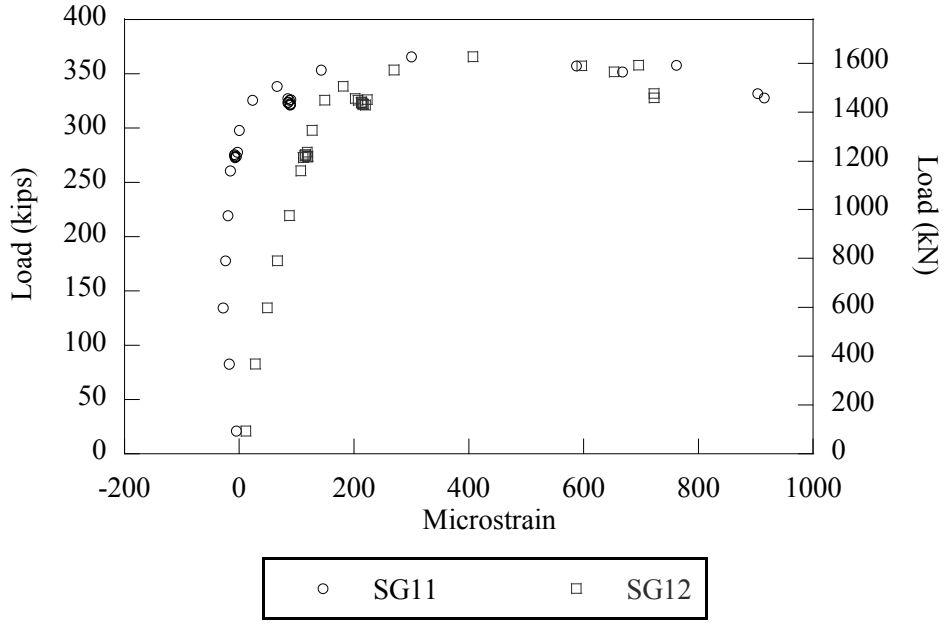

(a) LSC16

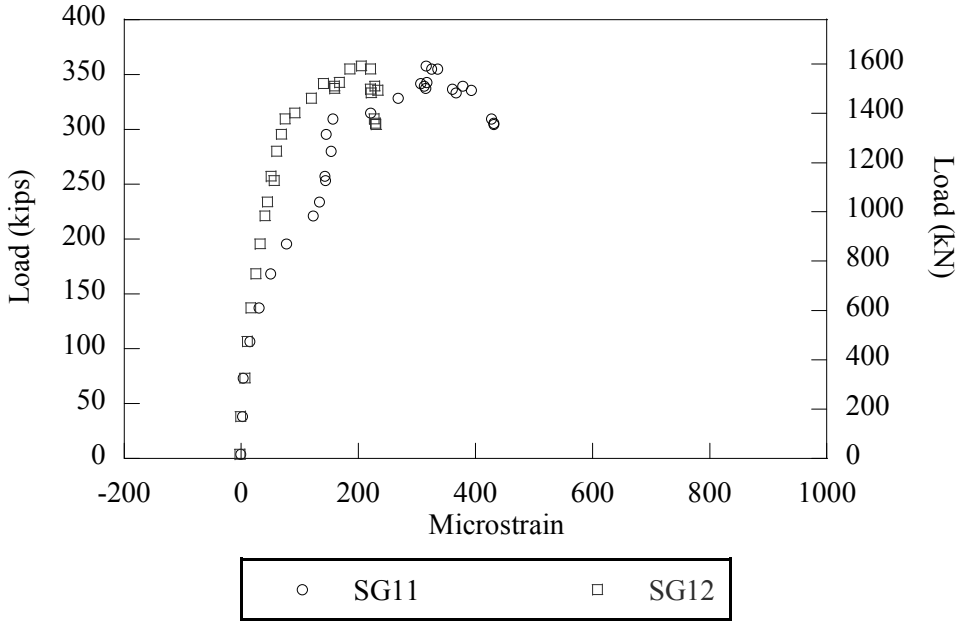

(b) LSC15

Figure 5-28 Load Versus Measured Strain in the Internal Strain Gages, SG11 and SG12 (Transverse Gages)

The external gages on the LSC specimens further reveal evidence of bond slip, compression failure of the concrete, and shear failure. Figure 5-29 shows the LVDTs on the tension side of the LSC specimens along the length of the splice. LVDT1 and LVDT8 are positioned at the splice end where most of the cracks were present and likewise measured the highest strains. This is consistent with the previous four-point test results. However, as the specimen began to fail, the measurements from the LVDTs differed greatly from the four-point test. Figure 5-30 shows that the strain measurements from LVDTs began to increase/decrease irregularly once the load exceeded 300 kips (1.33 MN), which can be explained by the bond slip.

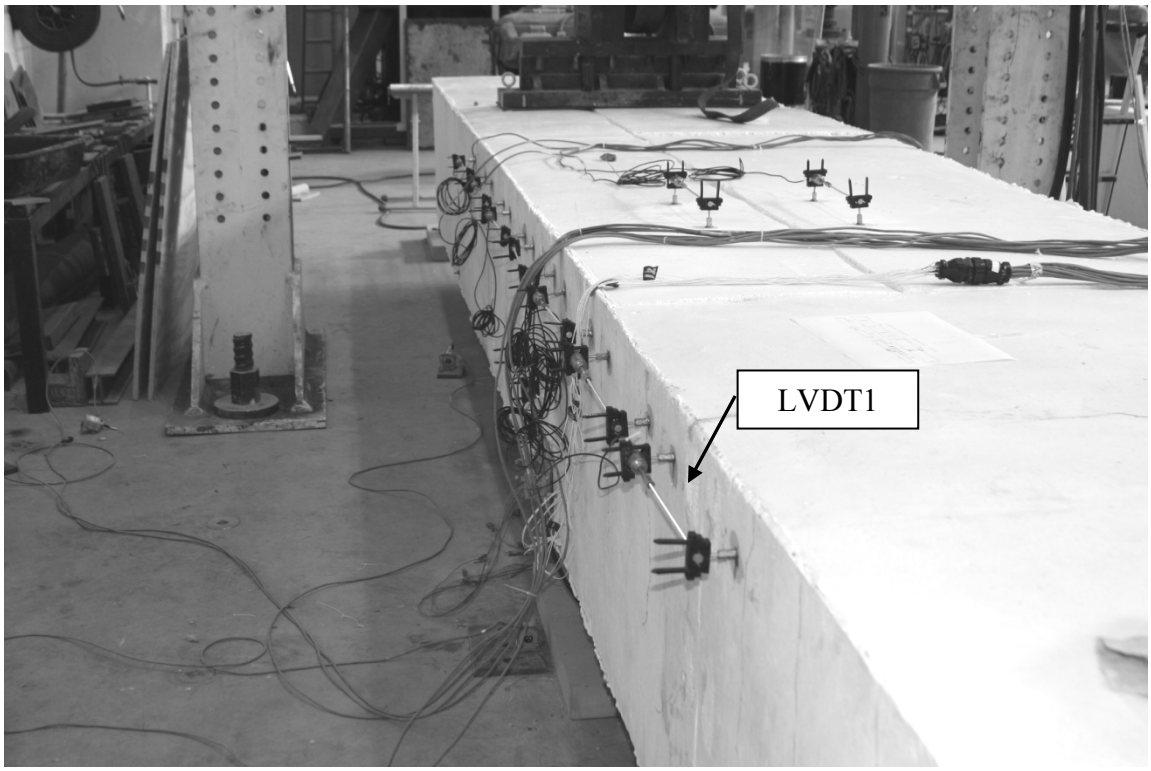

Figure 5-29 LVDTs Along the Splice Length in the Tension Region during the Three-point Test

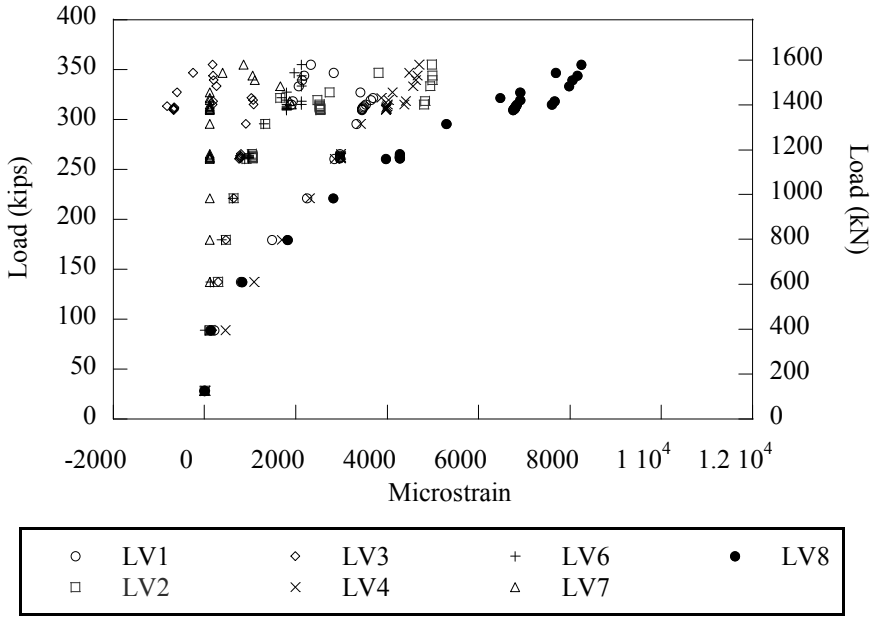

(a) LSC16

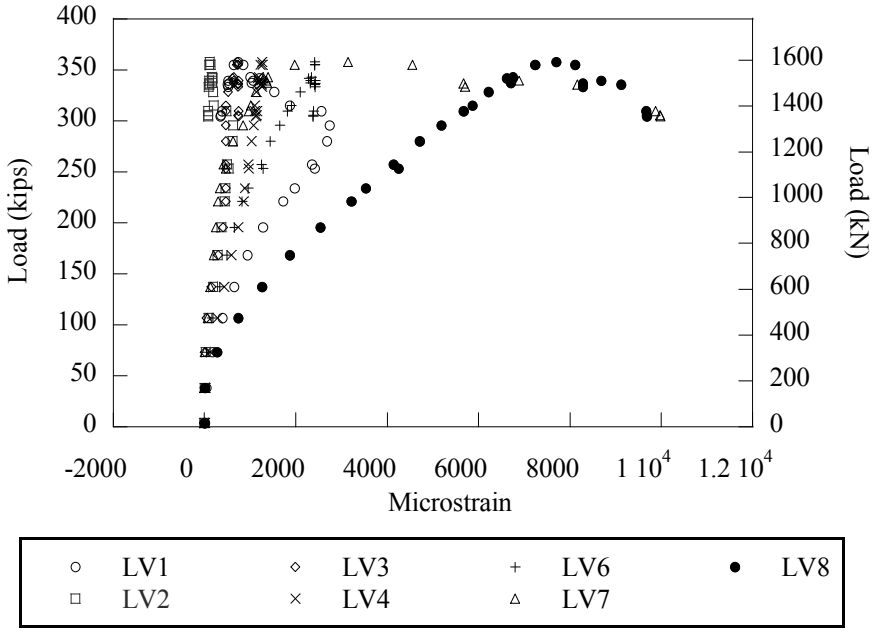

(b) LSC15

Figure 5-30 Load versus Measured Strain in the LVDTs across the Splice Length in the Tension Region

The concrete began to crush beneath the support towards the end of the test (see Figure 5-31), which is evident by the large strains as shown in Figure 5-32. Figure 5-32 shows the strain distribution at the critical section for flexural failure versus the applied load. The analytical predictions presented on the figure also show that the results from the test are more deformable than the prediction model. Also, note the high compressive strain on LSC16. As the specimen began to fail, the neutral axis moves up and the compression region becomes very small, which creates very high stresses in the concrete. Figure 5-33 shows the measurements from the KM gages attached to the LSC specimens. All gages on LSC16 surpassed ε_{cu}, while only KM8 on LSC15 measured such strains.

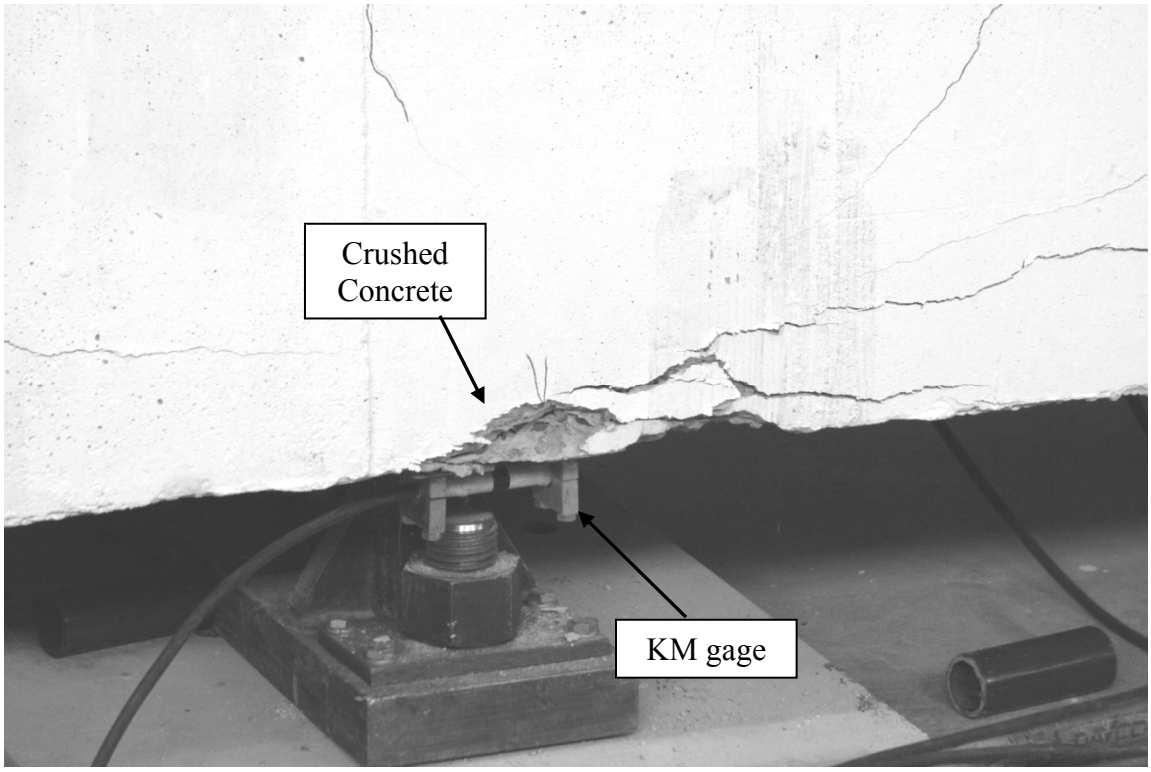

Figure 5-31 Crushing of the Concrete in the Three-point Test

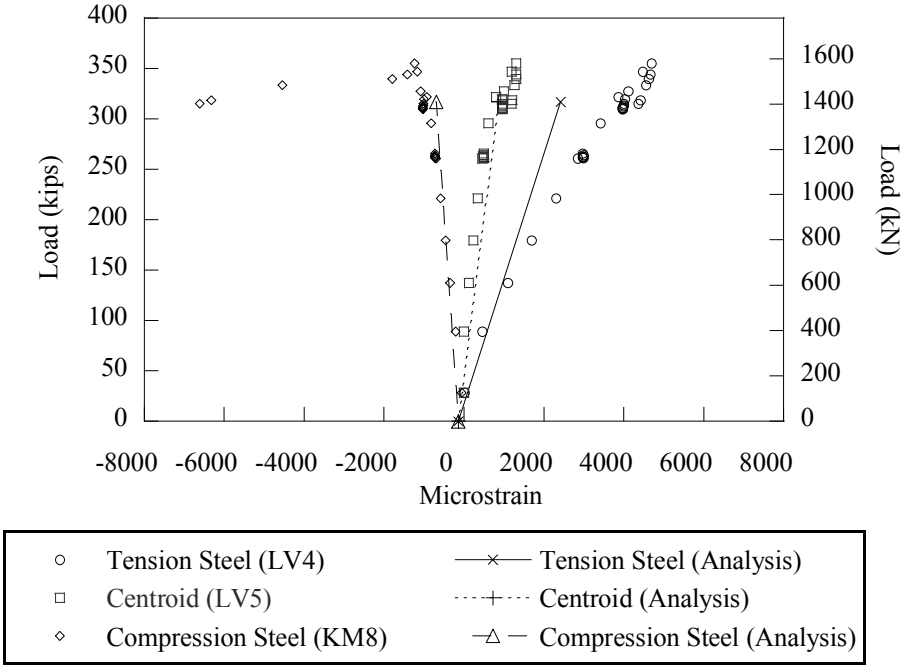

(a) LSC16

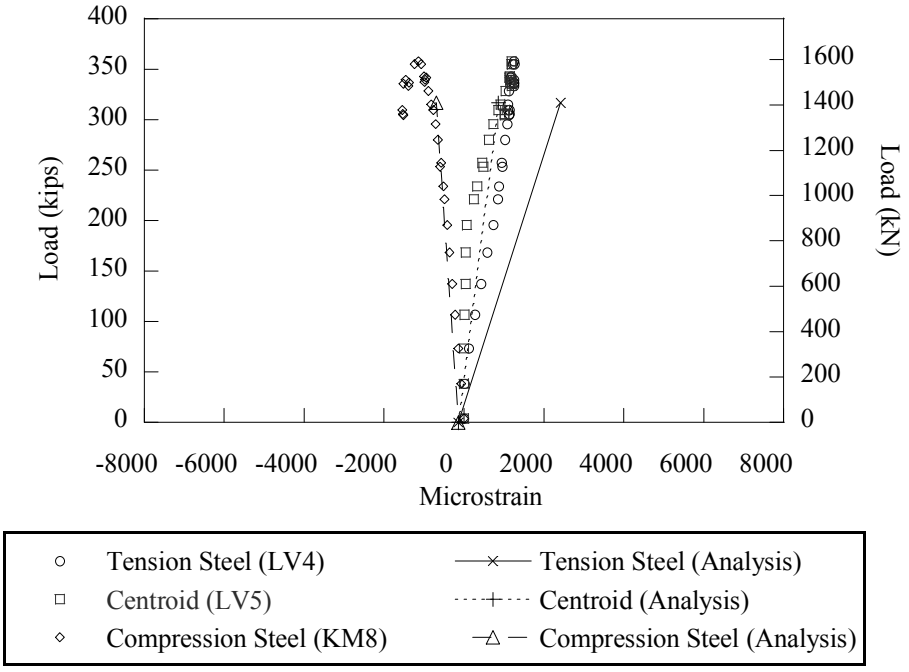

(b) LSC15

Figure 5-32 Load Versus Measured Strain of the External Strain Gages across the Depth of the Critical Section and the Analytical Prediction

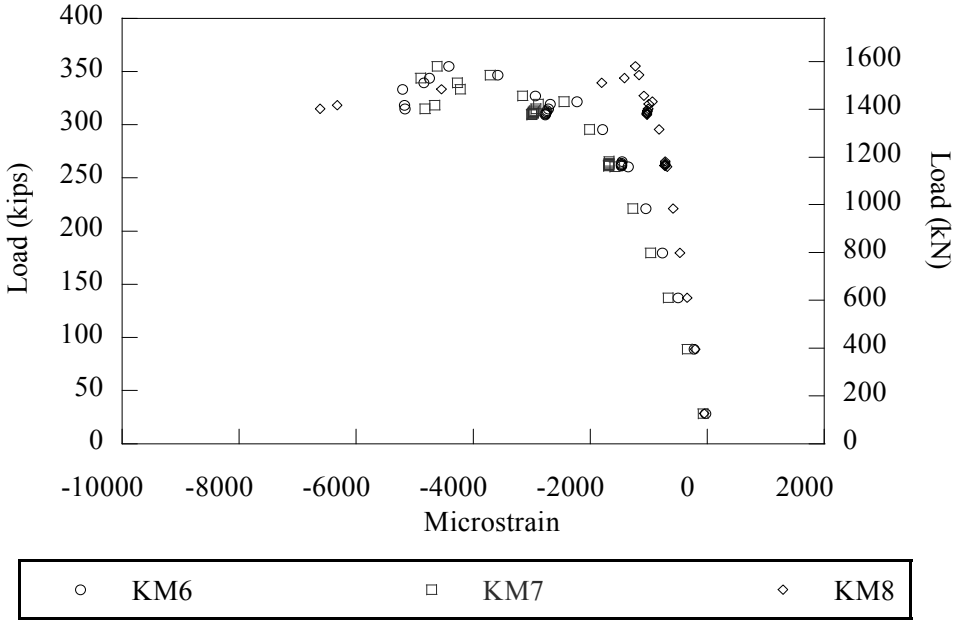

(a) LSC16

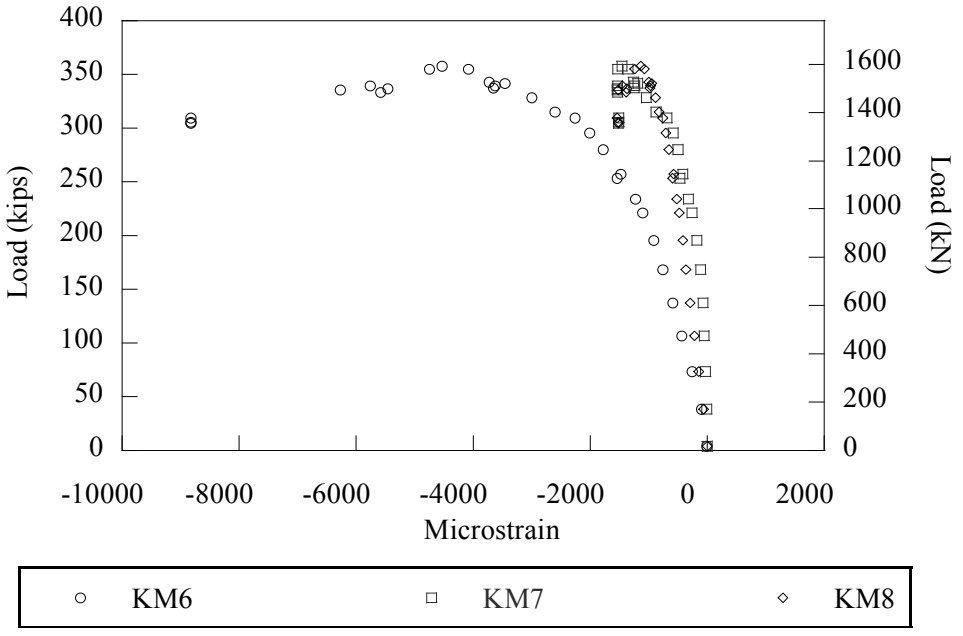

(b) LSC15

Figure 5-33 Load Versus Measured Strain in the LVDTs at the Splice End in the Compression Region

As in the four-point test, the strains measured on the side of the LSC specimen were compared with the strains measured on the extreme fibers of the tension region. Again, there was not an appreciable difference from the measurements on the side versus the top of the LSC specimens. However, the strains on LSC15 are significantly different. The strain measurements of LVDT9 were high while LVDT10 measured little to no strain. This could be due to the crack layout on LSC15. Figure 5-34 shows the tensile cracks run outside the gage length of LVDT10 and inside the gage length of LVDT9 (see Figure 5-35). This could be the cause of the different strain measurements from the two gages.

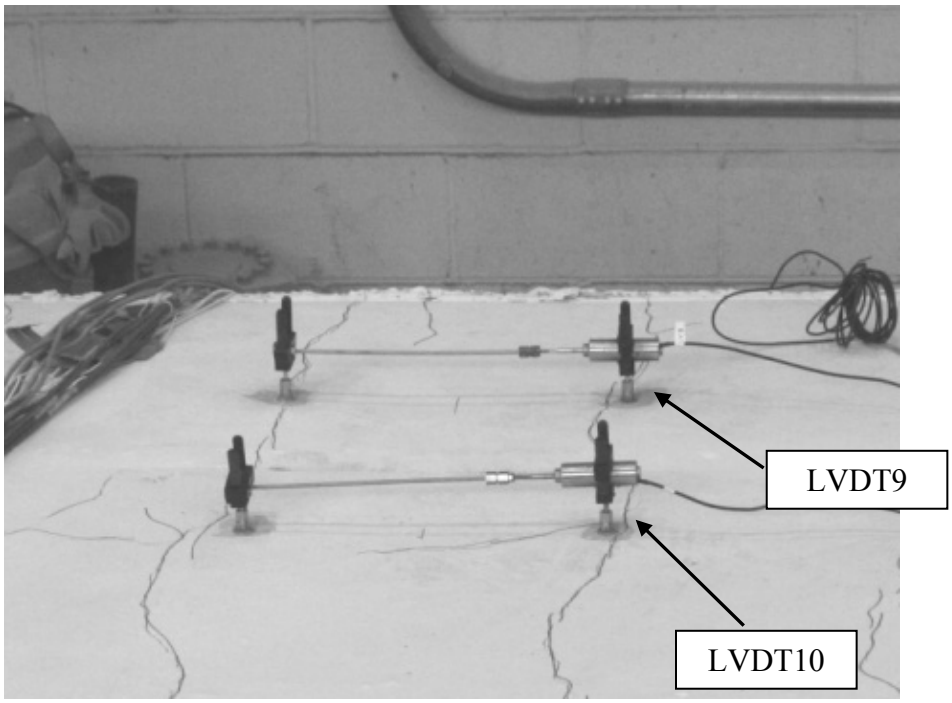

Figure 5-34 Tensile Cracks around LVDT9 and LVDT10

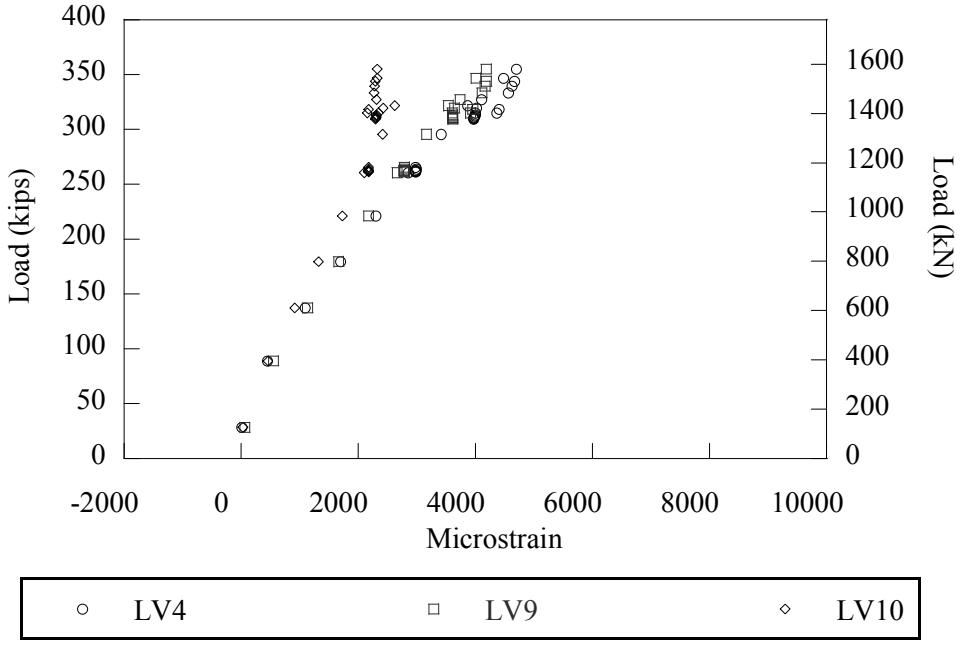

(a) LSC16

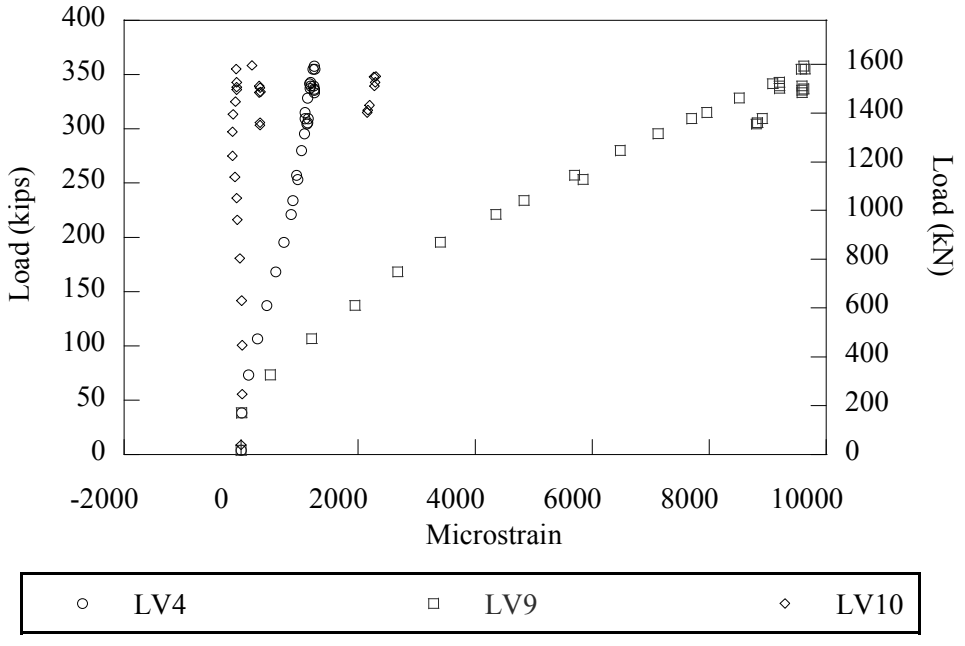

(b) LSC15

Figure 5-35 Load Versus Measured Strain in the LVDTs at the Splice End in the Tension Region

5.5. Summary

This section provided a description of the experimental design, load instrumentation, test procedures, and results for the three-and four-point load tests. In addition to the internal gages installed during fabrication of the LSC; LVDTs, KM gages, and STR gages were used to measure the strains in tension, in compression, and deflections of the LSC specimens respectively.

As predicted by the analytical model, the four-point load test resulted in yielding of the reinforcing steel at the splice ends. The strain measurements across the length of the splice indicated that the yielding of the steel at the splice end was localized and the splice region did not yield. Because sufficient bond was present between the steel and concrete the splice length can be assumed to be adequate to carry the design load.

The three-point load test had near simultaneous failure of the LSC specimen by three different mechanisms; flexure, bond slip, and shear. The specimen first developed cracks in the tension region due to flexural demand. Then at a total load of 300 kips (1.33 MN), the bars began to slip in the tension, which resulted in a decrease in strain on the bars while the load increased on the system. Finally, the specimen failed in shear at the splice ends. The analytical model reasonably predicts the load-deformation response for each given stage of the loading. Future testing of LSC specimens with premature concrete deterioration may weaken the bond and possibly alter the eventual failure mechanism.

6. SUMMARY AND FUTURE TESTING

6.1. Summary

This thesis presents an overview of the construction, testing, and evaluation of large-scale RC bridge column reinforced concrete specimens with a lap splice in the critical region with respect to load test demands. Sixteen specimens were fabricated and fourteen were placed in an accelerated atmospheric exposure environment to promote ASR and/or DEF. Two specimens were kept in an environment that inhibits the progression of ASR and DEF (room temperature with no moisture) and these were the focus of this thesis.

The expansion of the fourteen deteriorating large scale specimens was measured with internal and external gages. At this time the data indicates that the concrete surface strains are higher than the strains inside the hoop and in the cover. The measured strains in the hoop reinforcement indicate that the hoops are yielding in some specimens and the remaining specimens should begin to yield as the strains continue to increase. However, these strains are only on the top side of the large-scale specimens, which are exposed to the sun and higher temperatures. The strains in the regions of the LSC specimens closer to the ground are significantly lower, indicating that higher concrete surface temperatures could impact the amount of damage from ASR/DEF.

To protect the structural behavior of the large-scale specimens in the four-point and three-point load tests, an analytical model was developed. The model also can predict the strain in the reinforcements and concrete throughout the splice region. The model will be to predict performance during future testing of the deteriorated LSC specimens to correlate the amount of deterioration with the structural capacity of the specimen and based on this comparison, an effective development length factor will be used to assess

the safety of bridge columns that are influenced by varying levels of ASR/DEF deterioration.

The analytical model was validated using the large-scale control specimens which were not affected by ASR and/or DEF through four-point and three-point load tests designed to isolate the splice. The model reasonably predicted the load required to first crack the concrete, yield the tension reinforcement, and ultimate failure by bending moment demands.

The assumptions used to develop the analytical model are reasonable but can introduce challenges. For instance, the analytical model uses the assumption of a linear stress-strain curve for the concrete up to f'_c. This is a conservative estimate of the strength. The strength increase from a less conservative model would result in a higher neutral axis, which would induce higher strains in the tension steel as was found in the three- and four-point tests.

Another assumption that limits the accuracy of the model is the assumption of perfectly plastic behavior in the steel after yielding. It is well known that steel will exhibit more strength during the strain hardening portion of the stress-strain diagram. This will allow the model to capture the increase in strength after yielding to the steel has occurred.

Aside from assumptions on the stress-strain curves, the assumption of a linear contribution of the area of the bars according to the development length is conservative. Using a more accurate curve for this may improve the predictions from the analytical model on the expected strain gage results. This is pertinent to calibrating the model for use with solving the effective development length factors for the deteriorated LSC specimens later in the research.

6.2. Future Work

The analytical model and tests were designed with the future testing of the deteriorated specimens in mind. As discussed in Section 4.2.3, the capacity of the splice is dependent on the amount of steel in the section and the corresponding development length, and a factor to account for concrete deterioration, which will be derived from future tests in this research. These tests will be conducted on the remaining LSC specimens currently exposed to the accelerated atmospheric exposure environment discussed in Section 3.2.

The deteriorated LSC specimens will be tested with the same procedures used to evaluate the LSC control specimens in Section 5. From the testing, the calibrated analytical model will be adjusted using the development length factor until the model matches the test results. This will correlate an amount of deterioration with an effective development length.

It is expected that the effective development lengths will increase, but the amount is unknown. According to the AASHTO LRFD (2004), the splice is overdesigned by 22% as discussed in Section 2.1, so the effective development length can increase from the undeteriorated length of 52 in (1.32 m) to 63.5 in (1.61 m) without violating the code specifications. This means that a development length factor greater than 1.22 will violate the code specifications. An effective development length factor less than 1.22 will result in yielding of the bars in the splice, which indicates that the splice still carries the design flexural capacity. Beyond a factor of 1.22 the splice is not designed per code requirements but can theoretically hold the load up to an effective development length factor of 2.08. This is derived by taking the splice length and dividing by the calculated development length according to AASHTO LRFD (2004).

REFERENCES

AASHTO T126. (2001), *Standard Method of Test for Making and Curing Concrete Test Specimens in the Laboratory*. American Association of State Highway and Transportation Officials.

AASHTO. (2004), "LRFD Bridge Design Specifications," American Association of State Highway and Transportation Officials.

ACI Committee 318, (1963), "Building Code Requirements for Structural Concrete (ACI 318-63) and Commentary," American Concrete Institute.

ACI Committee 318, (1971), "Building Code Requirements for Structural Concrete (ACI 318-71) and Commentary," American Concrete Institute.

ACI Committee 318, (1989), "Building Code Requirements for Structural Concrete (ACI 318-89) and Commentary," American Concrete Institute.

ACI Committee 318, (1995), "Building Code Requirements for Structural Concrete (ACI 318-95) and Commentary," American Concrete Institute.

ACI Committee 408, (2005), "Bond and Development of Straight Reinforcing Bars in Tension," ACI 408R-03, ACI Manual of Concrete Practice.

ACI Committee 318, (2008), "Building Code Requirements for Structural Concrete (ACI 318-08) and Commentary," American Concrete Institute.

Ahmed, T., Burley, E., and Rigden, S., (1999a)"Effect of Alkali-Silica Reaction on Tensile Bond Strength of Reinforcement in Concrete Tested under Static and Fatigue Loading," *ACI Structural Journal*, 96(4) 419-428.

Ahmed, T., Burley, E., and Rigden, S., (1999b) "Effect of Alkali-Silica Reaction on Bearing Capacity of Plain and Reinforced Concrete," *ACI Structural Journal*, 96(4) 557-570.

Ahmed, T., Burley, E., and Rigden, S., (1998) "The Static and Fatigue Strength of Reinforced Concrete Beams Affected by Alkali-Silica Reaction," *ACI Structural Journal*, 95(4)376-388..

American Society for Testing and Materials. (2008) *ASTM C 1293: Standard Test Method for Determination of Length Change of Concrete Due to Alkali-Silica Reaction, Annual Book of ASTM Standard*s: Volume 04.02, Concrete and Aggregates. West Conshohocken, PA.

American Society for Testing and Materials. (2000) *ASTM C143-00 Standard Practice for Slump of Hydraulic-Cement Paste Concrete*: Volume 04.02, Concrete and Aggregates. West Conshohocken, PA.

American Society for Testing and Materials. (2001) *ASTM C39-01 Standard Test Method for Compressive Strength of Cylindrical Concrete Specimens, Annual Book of ASTM Standards:* Volume 04.02, Concrete and Aggregates. West Conshohocken, PA.

American Society for Testing and Materials. (2007) *ASTM C78-07 Standard Test Method for Flexural Strength of Concrete (Using Simple Beam with Third-Point Loading):* Volume 04.02, Concrete and Aggregates. West Conshohocken, PA.

Bauer, S., Cornell, B., Figurski, D., Ley, T., Miralles, J., and Folliard, K. (2006) *Alkali-Silica Reaction and Delayed Ettringine Formation in Concrete: A Literature Review*. Tech. no. FHWA/TX-06/0-4085-1. The University of Texas at Austin: Center for Transportation Research.

CEB-FIP Model Code 1990 Design Code. London: T. Telford, 1993.

Chana, P.S. (1989). *Bond Strength of Reinforcement in Concrete Affected by Alkali-Silica Reaction: Phase 1*. Contractor Report CR141. Transport and Road Research Laboratory, Crowthorne, UK.

Darwin D., Zuo, J., Tholen, M.L., and Idun, E.K., (1996) "Development Length Criteria for Conventional and High Relative Rib Area Reinforcing Bars," *ACI Structural Journal*, 93(3) 347-359.

Darwin, D., McCabe, S.L., Idun, E.K., and Schoenekase, S.P., (1992), "Development Length Criteria: Bars Not Confined by Transverse Reinforcement," *ACI Structural Journal*, 89(6) 709-720.

Fan, S. and Hanson, J. M., (1998), "Effect of Alkali Silica Reaction Expansion and Cracking on Structural Behavior of Reinforced Concrete Beams," *ACI Structural Journal*, 95(5), 498-505.

Fu, Y., (1996), "Delayed Ettringite Formation in Portland Cement Paste Products." Ph.D. Thesis, University of Ottawa, Canada.

Giacco, G., R. Zerbino, J. M. Ponce, and O. R. Batic, (2008), "Mechanical Behavior of Concretes Damaged by Alkali-Silica Reaction." *Cement and Concrete Research,* 38, 993-1004.

Jensen, V., (2003) "Elgeseter Bridge in Trondheim Damaged by Alkali Silica Reaction: Microscopy, Expansion and Relative Humidity Measurements, Treatment with Mono-silanes and Repair," *9th Euroseminar on Microscopy Applied to Building Materials,* September 9-12, Trondheim, Norway.

Monette, L.J., Gardner, N.J. and Grattan-Bellew, P.E. (2002). "Residual Strength of Reinforced Concrete Beams Damaged by Alkali-Silica Reaction- Examination of Damage Rating Index Method," *ACI Materials Journal,* 99(1), 42-50

Multon, S., Seignol, J.F., and Toutlemonde, F. (2005), "Structural Behavior of Concrete Beams Affected by Alkali-Silica Reaction," *ACI Materials Journal,* 102(2) 62-76.

Odler, I., and Chen, Y., (1996), "On the Delayed Expansion of Heat Cured Portland Cement Pastes and Concrete," *Cement and Concrete Composites*, 18, 181-185.

Orangun, C.O., Jirsa, J.O., and Breen, J.E., (1977), "Reevaluation of Test Data on Development Length and Splices," *ACI Journal, Proceedings* 74(3) 114-122.

Orangun, C.O., Jirsa, J.O., and Breen, J.E., (1975), "The Strength of Anchored Bars: A Reevaluation of Test Data on Development Length and Splices," *Research Report No. 154-3F,* Center for Highway Research, The University of Texas at Austin,

Petrov, N., Thibault, M., and Tagnit-Hamou, A. (2006) "Expansion Due to DEF in Normally-Cured Concrete Heated by Cement Hydration*." Special Publication*, 234, 239-250.

Poole, A. B., (1992), "Introduction to Alkali-aggregate Reaction in Concrete," In: *The Alkali-Silica Reaction in Concrete*, Taylor & Francis, Van Nostrand Reinhold, New York, pp. 1-29.

Scrivener, K. and Lewis, M., (1997), "A Microstructural and Microanalytical Study of Heat Cured Mortars and Delayed Ettringite Formation," *Proceedings of the 10th International Congress on the Chemistry of Cement*, Gothenburg, Sweden.

Standard Specifications for Construction and Maintenance of Highways, Streets, and Bridges, (2004), Special Publication, Texas Department of Transportation.

Swamy, R. N., (1992), "Testing for Alkali-silica Reaction," In: *The Alkali-Silica Reaction in Concrete*, Taylor & Francis, Van Nostrand Reinhold, New York, pp. 54-95.

Swamy, R. N., and Al-Asali, M. M., (1986), "Influence of Alkali-Silica Reaction on the Engineering Properties of Concrete," *Alkalies in Concrete, ASTM STP 930*, American Society for Testing and Materials, Philidelphia, 69-86.

Swamy, R. N., and Al-Asali, M. M., (1989), "Effect of Alkali-Silica Reaction on the Structural Behavior of Reinforced Concrete Beams," *Proc. ACI Structural Journal*, 86(4) 451-459.

Zhang, Z., Olek, J., and Diamond, S., (2002), "Studies on Delayed Ettringite Formation in Early-Age, Heat-Cured Mortars I. Expansion Measurements, Changes in Dynamic Modulus of Elasticity, and Weight Gains, *Cement and Concrete Research*, 32, 172–173.

Zuo, J. and Darwin, D., (2000), "Splice Strength of Conventional and High Relative Rib Area Bars in Normal and High Strength Concrete," *ACI Structural Journal*, 97(4) 630-641.

Zuo, J., and Darwin, D., (1998), "Bond Strength of High Relative Rib Area Reinforcing Bars," *SM Report No. 46*, University of Kansas Center for Research, Lawrence, 350-359.

VITA

Name:	Ryan Alberson
Address:	Protection Engineering Consultants, 14144 Trautwein, Austin, TX 78737
Email Address:	ralberson@protection-consultants.com
Education:	B.S., Civil Engineering, Texas A&M University, 2008 M.S., Civil engineering, Texas A&M University, 2009